

UNIVERSITY OF KWAZULU-NATAL

Semi-Empirical Modelling of Subtropical Rain
Attenuation on Earth-Satellite Microwave Links

Babajide Olugbenga Afolayan



January, 2018

Supervisor: Professor Thomas Joachim Afullo

Co-Supervisor: Dr. Akintunde Ayodeji Alonge

**SEMI-EMPIRICAL MODELLING OF SUBTROPICAL RAIN
ATTENUATION ON EARTH-SATELLITE MICROWAVE LINKS**

Babajide Olugbenga Afolayan

In fulfilment of the Degree of Doctor of Philosophy in Electronic Engineering,
College of Agriculture, Engineering and Science, University of KwaZulu-Natal,
Durban



January, 2018

Supervisor:

As the candidate's Supervisor, I agree/~~do not agree~~ to the submission of this thesis

Professor T.J. Afullo



Date: 17th January 2018

Co-Supervisor:

As the candidate's Co-Supervisor, I agree/do not agree to the submission of this thesis

Dr. A. A. Alonge _____

Date: _____

DECLARATION 1- PLAGIARISM

I, Babajide Olugbenga Afolayan, with Student Number 214584033, with the thesis entitled “Semi-Empirical Modelling of Subtropical Rain Attenuation on Earth-Satellite Microwave Links,” declare that

1. The research reported in this thesis, except otherwise indicated, is my original research.
2. This thesis has not been submitted for any degree or examination in any other university.
3. This thesis does not contain any other person’s data, pictures, graphs or other information not specifically acknowledged as being sourced from other persons.
4. This thesis does not contain other persons’ writing, unless specifically acknowledged as being sourced from other researchers. Where other written sources have been quoted, then a: Their words have been re-written but the general information attributed to them has been referenced, b: Where their exact words have been used, then their writing has been placed in italics and inside quotation marks, and referenced.
5. This thesis does not contain text, graphics or tables copied and pasted from the internet, unless specifically acknowledged, and the source being detailed and in the thesis and in the reference sections.

Signed.....

Date: 17th January 2018

DECLARATION 2 – PUBLICATIONS

DETAILS OF CONTRIBUTIONS TO PUBLICATIONS that form part and/or include research presented in this thesis:

JOURNAL PUBLICATIONS

- **B.O. Afolayan**, T.J. Afullo and A.A. Alonge, “Seasonal and Annual Analysis of Slant Path Attenuation over a 12 GHz Earth-Satellite Link in Subtropical Africa,” International Journal on Communications Antenna and Propagation, Vol. 7 (7), 2017. pp. 572 - 580
- **B.O. Afolayan**, T.J. Afullo and A.A. Alonge, “Subtropical Rain Attenuation Statistics on 12.6 GHz Ku-Band Satellite Link using Synthetic Storm Technique,” Accepted for publication in South African Institute of Electronic Engineers (SAIEE) African Research Journal. May, 2018

CONFERENCE PROCEEDINGS

- **B.O. Afolayan**, T.J. Afullo and A.A. Alonge, “Time matching of attenuation-precipitation events on a slant path link,” Progress in Electromagnetic Research Symposium (PIERS), Shanghai, China, 8-11 Aug. 2016. <http://ieeexplore.ieee.org/document/7735810/>
- **B.O. Afolayan**, T.J. Afullo and A.A. Alonge, “Dynamics of Reception Outage due to Subtropical Rainfall on a Satellite TVRO Link”, in Proceedings of Southern African Telecommunication Networks and Applications Conference, George, South Africa, 4-7 September, 2016, pp. 4967 – 4970.
<http://ieeexplore.ieee.org/document/7735810/>
- **B.O. Afolayan**, T.J. Afullo and A.A. Alonge, “A Generalized Analysis of Attenuation-Precipitation Time Lapse Events on Earth-Satellite Microwave Links”, in Proceedings of 2017 IEEE AFRICON, Cape Town, South Africa. 18-20 September 2017 pp. 332 – 337
<http://ieeexplore.ieee.org/document/8095504/>

Signed:.....

ACKNOWLEDGEMENTS

To God the Father and to Christ “*in whom are hid all treasures of wisdom and knowledge.*”

- *Colossians 2:3 (King James Version)*

I acknowledge with special appreciation my supervisor Professor Thomas Afullo whose role in this work and in my life has been extremely positive. You have been a real mentor, a support and a trainer in the art of being the best one can be in anything.

I appreciate the immense support of my co-supervisor, Dr. Akintunde Alonge in guidance, in invaluable advice here and there and in blazing the trail to many possibilities.

My regards to everyone in the Radio Propagation research group of the School of Electrical, Electronic and Computer Engineering of the University of KwaZulu-Natal, Howard Campus, Durban for the co-operation, the camaraderie, and the shared passion for useful research which has been a buoy for me throughout this program.

To the three women in my life: my wife Adedolapo Dorothy (*the wise*), my bigger baby Sophia Tumininu (*the smart*) and my smaller baby Oreoluwa Joy (*the compassionate*). You have all sacrificed so much for me to be able to do this. No words can convey my gratefulness. May God grant us many years for me to show it in kind.

To my big sister Olutoyin Omolara Olaitan. You told me to do this long ago. Glad I finally listened before it got too late. Your support and encouragement has been immensely helpful.

DEDICATION

*For **Jumoke**.*

*And for **Iya Barra**.*

“Good people pass away; the godly often die before their time. But no one seems to care or wonder why. No one seems to understand that God is protecting them from the evil to come.”

Isaiah 57:1 (New Living Translation)

ABSTRACT

The exponential rise in demand for high fidelity content on multiple platforms has in recent years made increased use of the higher echelons of radio communication frequency inevitable. At these high frequencies, wavelength becomes small enough to compare with the size of rain drops and in some cases smaller than drop size. This implies that the impairment due to rain, which already usually forms the most severe form of impairment at higher radio frequency bands, will become even more acute and require rigorous parameterization.

This thesis investigates both by rigorous measurements and by theoretical approaches, the attenuation effect of rainfall in a subtropical climate (Durban, South Africa) on a microwave earth-satellite link operating at 12.6 GHz. The link was set up and the received signal level monitored via spectrum analyser sweeps conducted every minute. A Joss-Waldvogel impact disdrometer was installed such that its diaphragm is located a few meters away from the link's receive antenna. From such a location, all precipitation recorded by the disdrometer are assumed to have some effect on the link. The monthly variation in the received signal during clear air was investigated by taking into consideration the average monthly values of temperature, relative humidity and atmospheric pressure. By employing multiple regression, a linear expression was obtained that can be used to predict the change in received signal level in clear air over the link given the values of these three atmospheric parameters. The attenuation due to the rain events was extracted from the data by carrying out an even-by-event matching of rain rate spikes with the corresponding drop observed in the received signal level at and around the time of the precipitation. The average monthly received signal level during clear air was extracted from the spectrum analyser data and used as the base channel power to which the received signal during rain in the particular month is compared. The difference between the two is stored as the attenuation due to rain in that instant of measurement time. The attenuation data thus accumulated were entered into a computer algorithm and a regression fitting procedure carried out to deduce an empirical set of logarithmic and power law models that relate the total path attenuation to rain rate. The models were then validated by a largely favourable comparison with four existing models, one of which is the in-force ITU-recommended model for slant path attenuation estimations.

Random number properties of rain attenuation statistics obtained from the measurement model were exploited to develop a Markov chain approach by which seasonal and annual slant path rain attenuation time series can be generated. By investigating the nature of the probability distributions of the seasonal and annual measured path attenuation statistics, which was found to be lognormal, the state probability matrix necessary for implementing a Markov chain prediction model for future patterns of rain attenuation on a similar link was obtained as the lognormal probability density function. The state transition probability vector for each time period was developed by extracting the fade slope statistics of the measured attenuation. The discrete-time Gaussian distributed fade slope PDF forms the basis for

the state transition probability matrix. With these, Markov-generated time series of seasonal and annual slant path attenuation for up to five iterations were obtained. The results make useful data that can be used for long-term planning for rain fade mitigation in a subtropical climate easier to generate without the expense of measurements.

The theoretical approach called the Synthetic Storm Technique was also applied to investigate the nature of slant path rain attenuation in Durban. Based on the rainfall pattern captured by the disdrometer, SST approximations for the four seasons of the subtropical year and for years of rain data collection were carried out. The results were compared with the values generated from the measurement model. It reveals that the two models exhibit significant agreement because in a majority of the cases, the $A_{0.01}$ values obtained are very close. Comparison of the performance of SST as a theoretical model with that of the ITU-recommended method also reveals that the ITU performs slightly better as an alternative to measurement than the SST model.

It was observed that during certain precipitation events, the satellite link registers significant attenuation levels several minutes before the disdrometer records any precipitation on the ground. This anomaly was investigated in this work and a few conclusions drawn. By proceeding on the assumption that the observed delay was due to the migrating rain cell interacting with the satellite beam several minutes before reaching the receive antenna, it was demonstrated that the time of delay between precipitation and attenuation is related to the rain height during that particular rain event. A simple mathematical analysis is presented that enables the rain height to be estimated from the delay time. The results obtained range between 1.4 km to 6.7 km which is similarity to rain height values obtained by the ITU model which range from 1.36 km to 6.36 km.

TABLE OF CONTENTS

DECLARATION 1- PLAGIARISM.....	ii
DECLARATION 2 – PUBLICATIONS.....	iii
ACKNOWLEDGEMENTS	iv
DEDICATION	v
ABSTRACT	vi
TABLE OF CONTENTS	viii
LIST OF FIGURES.....	xi
LIST OF TABLES	xiv
CHAPTER ONE: INTRODUCTION	1
1.1 Introduction.....	1
1.2 Problem Formulation	2
1.3 Scope of the Work	3
1.4 Thesis Overview	3
1.5 Contributions to Knowledge	4
1.6 Publications.....	5
CHAPTER TWO: LITERATURE REVIEW.....	6
2.1 Electromagnetic Phenomena.....	6
2.2 The Radio Frequency Spectrum.....	7
2.3 Overview of Losses in Radio Propagation.....	8
2.3.1 Free Space Path Loss	9
2.3.2 Refractive Loss	9
2.3.3 Loss to Vegetation	10
2.3.4 Atmospheric Gas Loss	11
2.4 Fundamentals of rain structure and rain impairment of radio links	11
2.4.1 Scattering and absorption in rain	11
2.4.2 Radio waves in a water medium.....	12
2.4.3 Microphysical Structure of Rain	13
2.4.4 Rainfall Rate	14
2.4.5 Rain Rate Exceedance.....	15
2.4.6 Classification of Rain.....	16
2.4.7 Some Characteristics of Subtropical Climate	16
2.5 Theory and models of Slant Path Rain Attenuation Prediction	17
2.5.1 Olsen Power Law Model.....	18

2.5.2	The Lin Model	18
2.5.3	The Crane (Global) Model.....	19
2.5.4	The Garcia-Lopez Model.....	19
2.5.5	The ITU-R Model	20
2.6	Overview of Earth-Satellite Communication.....	22
2.6.1	Geostationary Orbits	23
2.6.2	Link budgeting for Downlink Reception	25
2.6.3	Sun Outage on Satellite Links.....	26
2.7	Chapter Summary	26
CHAPTER THREE: MODELLING OF MEASURED ATTENUATION AT Ku BAND IN		
SUBTROPICAL RAIN		
		27
3.1	Introduction.....	27
3.2	Measurement System Description	27
3.2.1	Rain Rate Measurement.....	29
3.2.2	Satellite Beacon Receiver System.....	30
3.3	Link Budget Analysis	33
3.4	Statistical Analysis of measured rain rate data	34
3.4.1	Rainfall Rate Exceedance over Durban	35
3.5	Modelling of Clear Air Attenuation from Measured RSL.....	38
3.5.1	Results and modelling of measured RSL in Clear-Air.....	39
3.6	Modelling of Measured Rain Attenuation	42
3.6.1	Correlation of Rainfall Spikes with RSL Values	42
3.6.2	Measured Earth-Space Attenuation Statistics	45
3.6.3	Rain Attenuation Bounds over the Earth-Satellite Link	50
3.6.4	Slant Path Rain Attenuation Exceedance Statistics	52
3.6.5	Validation of the Proposed Measurement Model.....	54
3.7	Reception Outage at Slant Paths due to Rain Attenuation.....	58
3.8	Chapter Summary	61
CHAPTER FOUR: GENERATION OF RAIN ATTENUATION TIME SERIES FROM		
MEASUREMENT-DERIVED PDFS BY MARKOV CHAIN PRINCIPLE.....		
		62
4.1	Introduction	62
4.2	Basic Markov Chain Principles.....	62
4.3	Probability density functions of measured attenuation	66
4.4	State Transition Probability Matrix and Fade Slope Statistics.....	72
4.5	Markov-Generated Path Attenuation Time Series	79
4.6	Exceedance statistics of Markov-Generated slant path attenuation.....	82

4.7 Chapter Summary	86
CHAPTER FIVE: SYNTHETIC STORM TECHNIQUE ANALYSIS OF SLANT PATH	
ATTENUATION IN SUBTROPICAL RAIN	88
5.1 Introduction.....	88
5.2 Theoretical Framework for the Synthetic Storm Technique.....	88
5.3 Input Parameters and Link Statistics.....	91
5.4 Attenuation Prediction by SST for some Rain Events	91
5.5 Annual SST Attenuation Results	95
5.6 Performance of SST Compared with the ITU-R Prediction	97
5.7 Chapter Summary	99
CHAPTER SIX: ESTIMATION OF RAIN HEIGHT FROM ATTENUATION-PRECIPITATION TIME	
DELAY DATA.....	100
6.1 Introduction.....	100
6.2 Dynamics of the interaction between the Rain System and the Slant Path.....	100
6.3 Extraction of the Time Delay Statistics	102
6.4 Relationship of Time Delay with Rain Height.....	104
6.5 Results of Rain Height Estimated from Time Delay Statistics.	107
6.6 Chapter Summary	109
CHAPTER SEVEN: CONCLUSIONS AND RECOMMENDATIONS.....	
7.1.1 Introduction.....	110
7.1.2 Chapter Three - Measurement of Attenuation at Ku Band in Subtropical Rain	110
7.1.3 Generation of Rain Attenuation Time Series from Measurement-Derived PDFs by Markov Chain Principle.....	110
7.1.4 Synthetic Storm Technique Analysis of Slant Path Attenuation in Subtropical Rain.....	111
7.1.5 Estimation of Rain Height from Attenuation-Precipitation Time Delay Data.....	111
7.2 Recommendations for Future Work.....	111
REFERENCES	113

LIST OF FIGURES

Figure 2-1: Poynting Vector	7
Figure 2-2: Absorption by water vapour and oxygen showing characteristic peaks at some frequencies [32]	11
Figure 2-3: Dynamics of absorption and scattering in rain.....	12
Figure 2-4: Dependence of terminal velocity of raindrops on diameter [45].....	14
Figure 2-5: Subtropical Regions of the world (indicated in yellow) using the Koppen climate classification [1].	16
Figure 2-6: Slant Path Profile [8].....	20
Figure 2-7: Satellite Link profile	23
Figure 2-8: Geostationary satellite orbit relative to Earth’s geometry.....	24
Figure 2-9: Dynamics of sun outage [79]	26
Figure 3-1: Schematic of the co-located dual measurement system	28
Figure 3-2: Outdoor and indoor components of the measuring equipment set-up. Disdrometer diaphragm is 3.8 m from the receive antenna.....	28
Figure 3-3: Schematic diagram of the Joss-Waldvogel impact disdrometer.	29
Figure 3-4: Time series of rain rate captured in the entire month of May, 2013	29
Figure 3-5: Time series of rain rate captured in a 3-hour period on 16th October 2014	30
Figure 3-6: Basic physical profile of the satellite link.	30
Figure 3-7: Footprint of the IS-20 communications satellite over southern Africa [82]	31
Figure 3-8: Time series of received signal level captured over a rainy period on 14th of November, 2013	32
Figure 3-9: Seasonal Rain Rate Exceedance in Durban for 2013	37
Figure 3-10: Seasonal and Rain Rate Exceedance in Durban for 2014	37
Figure 3-11: Annual and Rain Rate Exceedance in Durban for 2013 and 2014.....	38
Figure 3-12: Variation of Monthly Averages of Clear Air Signal over Durban ($\theta = 36.5^\circ, f = 12 \text{ GHz}$)	39
Figure 3-13: Variation of monthly averages of temperature and relative humidity with average monthly RSL in clear air	41
Figure 3-14: Variation of monthly averages of atmospheric pressure with average monthly RSL in clear air.....	42
Figure 3-15: Assignment of rain peaks to RSL troughs for a drizzle event on 04/04/2014.....	43
Figure 3-16: Assignment of rain peaks to RSL troughs for a shower event on 20/11/2013	43
Figure 3-17: Assignment of rain peaks to RSL troughs for a widespread event on 15/12/2014	44
Figure 3-18: Assignment of rain peaks to RSL troughs for a drizzle event on 12/06/2013.....	44
Figure 3-19: Variation of measured attenuation with rain rate in Nov 2013 ($\theta=36.5^\circ, f=12 \text{ GHz}$)	46
Figure 3-20: Variation of measured attenuation with rain rate in December 2013 ($\theta=36.5^\circ, f=12 \text{ GHz}$)	46
Figure 3-21: Variation of measured attenuation with rain rate in February 2014 ($\theta=36.5^\circ, f=12 \text{ GHz}$)	47
Figure 3-22: Variation of measured attenuation with rain rate in April 2014 ($\theta=36.5^\circ, f=12 \text{ GHz}$)....	47
Figure 3-23: Variation of measured attenuation with rain rate in June 2014 ($\theta=36.5^\circ, f=12 \text{ GHz}$)....	48
Figure 3-24: Variation of measured attenuation with rain rate in August 2014 ($\theta=36.5^\circ, f=12 \text{ GHz}$).48	48
Figure 3-25: Variation of measured attenuation with rain rate in October 2014 ($\theta=36.5^\circ, f=12 \text{ GHz}$).	49
Figure 3-26: Variation of measured attenuation with rain rate in November 2014 ($\theta=36.5^\circ, f=12 \text{ GHz}$)	49

Figure 3-27: Scatter plot of all coincident attenuation points measured at each rain rate.	50
Figure 3-28: Logarithmic Models of Rain Attenuation Bounds model ($\theta = 36.5^\circ, f = 12 \text{ GHz}$)	51
Figure 3-29: Comparison of measured Rain Attenuation with ITU-R model ($\theta = 36.5^\circ, f = 12 \text{ GHz}$). ..	52
Figure 3-30: Seasonal and Annual Slant Path Attenuation Exceedance Probability in Rainfall over Durban, ($\theta = 36.5^\circ, f = 12 \text{ GHz}$).	53
Figure 3-31: Performance of the bounded measurement-based models compared with existing models in the 11 dB path attenuation margin.....	56
Figure 3-32: Synchronized attenuation-precipitation time series during a 2013 thunderstorm event that resulted in loss of reception.	58
Figure 3-33: Synchronized attenuation-precipitation time series during a 2014 thunderstorm event that	59
Figure 3-34: Synchronized attenuation-precipitation time series during a 2014 shower event that resulted in loss of reception.....	59
Figure 3-35: Synchronized attenuation-precipitation time series during a 2014 shower event that resulted in loss of reception.....	60
Figure 4-1: State Space and State Probability Matrix.....	64
Figure 4-2: State transition probabilities of a 5-state Markov Chain.....	64
Figure 4-3: Rain attenuation time series in the 500th to 800th time instant of rain during winter season in Durban in 2013 ($f=12.6 \text{ GHz}, \theta = 36.5^\circ, t_n = 30 \text{ seconds}$).....	67
Figure 4-4: Rain attenuation time series in the 9,000th to 16,000th time instant of rain in Durban in 2016 ($f=12.6 \text{ GHz}, \theta = 36.5^\circ, t_n = 30 \text{ seconds}$).....	67
Figure 4-5: PDF of slant path rain attenuation statistics in a winter season in Durban. ($f = 12.6 \text{ GHz}, \theta$ $= 36.5^\circ$)	69
Figure 4-6: PDF of slant path rain attenuation statistics in a spring season in Durban. ($f = 12.6 \text{ GHz}, \theta$ $= 36.5^\circ$)	69
Figure 4-7: PDF of slant path rain attenuation statistics in an autumn season in Durban. ($f = 12.6 \text{ GHz},$ $\theta = 36.5^\circ$)	70
Figure 4-8: PDF of slant path rain attenuation statistics in a summer season in Durban. ($f = 12.6 \text{ GHz},$ $\theta = 36.5^\circ$)	70
Figure 4-9: PDF of slant path rain attenuation statistics in 2013 in Durban. ($f = 12.6 \text{ GHz}, \theta = 36.5^\circ$) ..	71
Figure 4-10: PDF of slant path rain attenuation statistics in 2014 in Durban. ($f = 12.6 \text{ GHz}, \theta = 36.5^\circ$)	71
Figure 4-11: PDF of slant path rain attenuation statistics in a 2015 in Durban. ($f = 12.6 \text{ GHz}, \theta = 36.5^\circ$)	72
Figure 4-12: PDF of slant path rain attenuation statistics in 2016 in Durban. ($f=12.6 \text{ GHz}, \theta = 36.5^\circ$) ..	72
Figure 4-13: Illustration of fade slope using a 50tn rain fade time series during Summer in Durban. ($f=12.6 \text{ GHz}, \theta = 36.5^\circ$)	73
Figure 4-14: Approximation of each element of the state transition probability matrix from fade slope PDF.....	74
Figure 4-15: PDF of the fade slope of measured attenuation in a subtropical winter season	75
Figure 4-16: PDF of the fade slope of measured attenuation in a subtropical summer season.....	76
Figure 4-17: PDF of the fade slope of measured attenuation in a subtropical spring season	76
Figure 4-18: PDF of the fade slope of measured attenuation in a subtropical autumn season	77
Figure 4-19: PDF of the fade slope of measured attenuation in 2013 in Durban	77
Figure 4-20: PDF of the fade slope of measured attenuation in 2014 in Durban	78
Figure 4-21: PDF of the fade slope of measured attenuation in 2015 in Durban	78
Figure 4-22: PDF of the fade slope of measured attenuation in 2016 in Durban	79

Figure 4-23: Comparison of measured and simulated slant path rain attenuation time series for the 100th to 200th time instant during a subtropical winter season.	80
Figure 4-24: Comparison of measured and simulated slant path rain attenuation time series for the 6000th to 6150th time instant in 2013.	81
Figure 4-25: Comparison of measured and simulated slant path rain attenuation time series for the 250th to 330th time instant in 2014.	82
Figure 4-26: Comparison of measured and simulated slant path rain attenuation time series for the 1st to 90th time instant in 2015.	82
Figure 4-27: Comparison of measured and simulated slant path rain attenuation time series for the 20000th to 20070th time instant in 2016.	83
Figure 4-28: Rain attenuation exceedance for measured and Markov-generated statistics in winter.	84
Figure 4-29: Rain attenuation exceedance for measured and Markov-generated statistics in spring.	84
Figure 4-30: Rain attenuation exceedance for measured and Markov-generated statistics in autumn.	85
Figure 4-31: Rain attenuation exceedance for measured and Markov-generated statistics in summer.	85
Figure 4-32: Rain attenuation exceedance for measured and Markov-generated statistics for 2013.	86
Figure 4-33: Rain attenuation exceedance for measured and Markov-generated statistics in 2014.	87
Figure 4-34: Rain attenuation exceedance for measured and Markov-generated statistics in 2015.	87
Figure 4-35: Rain attenuation exceedance for measured and Markov-generated statistics in 2016.	87
Figure 5-1: Two-layer vertical profile of rain for the Synthetic Storm Technique	89
Figure 5-2: SST and measured attenuation for rain event on 6th of May, 2016	93
Figure 5-3: SST and measured attenuation for rain event on 6th of February 2015	93
Figure 5-4: SST and measured attenuation for rain event on 4th of November 2014	93
Figure 5-5: SST and measured attenuation for rain event on 3rd of December 2013.	94
Figure 5-6: SST and measured attenuation for rain event on 1st of March 2015	94
Figure 5-7: Comparison of SST attenuation exceedance probability with measurement 2013	95
Figure 5-8: Comparison of SST attenuation exceedance probability with measurement 2014	96
Figure 5-9: Comparison of SST attenuation exceedance probability with measurement 2015	96
Figure 5-10: Comparison of SST attenuation exceedance probability with measurement 2016	97
Figure 5-11: Comparison of the three models at 1 to 40 mm/h.	99
Figure 6-1: Rain formation in Durban and its interaction with the slant path of satellite beacon	102
Figure 6-2: Illustration of a time delay event.	104
Figure 6-3: Illustration of a time delay event.	104
Figure 6-4: Exceedance probability of rain height estimated from time delay events in Durban.	109

LIST OF TABLES

Table 1-1: Some background studies of rain and rainfall effects in Durban, South Africa.....	2
Table 2-1: ITU Nomenclature for radio communication frequency Bands.....	8
Table 2-2: Microwave Satellite Communication bands.....	8
Table 2-3: Months of the seasons in Durban.....	17
Table 3-1: Basic link parameter.....	32
Table 3-2: Link Budget for Reception Footprint of Intelsat-20 Satellite over Durban	33
Table 3-3: Seasonal summary of rain rate data for 2013 and 2014.....	35
Table 3-4: Peak Rain Rate Data for 2013 and 2014 by Rain Type.....	36
Table 3-5: Average Seasonal and Annual Rain Rate Exceedance Statistics in Durban	39
Table 3 6: Monthly Average Variation of RSL and Atmospheric Parameters in Clear Air Propagation over Durban.....	41
Table 3 7: Seasonal Attenuation Statistics over Durban.....	46
Table 3-8: Logarithmic and Power Law Models of Slant Path Attenuation.....	53
Table 3 9: Seasonal Values of Path Attenuation Exceedance	54
Table 3 10: RMS Error values of measured attenuation bounds against some existing models	58
Table 3 11: Chi-Square test results of measured attenuation against expected values from some existing models	58
Table 4-1: Lognormal parameters of the seasonal and annual rain attenuation PDFs.....	69
Table 4-2: Error Analysis of the lognormal-distributed attenuation statistics	69
Table 4-3: Error analysis of the normally-distributed attenuation statistics	75
Table 4-4: Gaussian mean and standard deviation for periodic datasets of fade slope.....	76
Table 4-5: Measured and Markov-Generated $A_{0,01}$ values.....	83
Table 5-1: Input parameters used for the 2-layer vertical rain profile	93
Table 5-2: Path attenuation at various exceedance probabilities for both models	98
Table 5-3: Error analysis of SST and ITU-R model using measurement figures as the expected value.....	100
Table 6-1: Time lapse events	104
Table 6-2: Rain Height estimates from time delay events	108

CHAPTER 1: INTRODUCTION

1.1 Introduction

Communication links are deployed primarily in the populated regions of the world. Thus, the performance of these systems in locations such as the frigid regions to the north and south poles for example is not of particular interest to system designers. Populated regions of the planet are divided into three major climatic zones or regions [1]. The most researched region in terms of tropospheric effects of radio propagation is the temperate region. This is followed by the tropical region and lastly the subtropics. In the early evolution of widespread deployment of wireless communications, the largest amount of hardware design and production takes place in the temperate regions of the planet namely Europe, America, Japan and China. Nearly all the systems deployed in the early days were calibrated based on research done in temperate regions. In more recent decades however, the rate of increase in the level of deployment in the tropical regions (example, India and Nigeria) and in the subtropical regions of the world (example, South Africa and Australia) occupy an increasingly significant percentage of the global total. Thus, it is imperative to inculcate more region-specific research input into system design and production [2].

There is a tendency to assume that tropospheric conditions in the subtropics can be simply approximated as a kind of average of those of the temperate and tropical locations. However, recent research has revealed that the subtropical troposphere possesses its own uniqueness that requires detailed investigation in order to attain high fidelity for communication systems deployed in the region [3-6].

The phenomenon of rain bears a unique place among other tropospheric effects on earth-satellite radio propagation especially at frequencies of and above the 7 GHz and 10 GHz range, being the highest source of loss that can be anticipated other than free space loss [2]. Rainfall, and by extension rain impairment is a stochastic event. Its variability in time and space implies that the ability to predict it with some level of accuracy rests in turn on the ability to carry out location-specific measurements over a reasonable period of time [7]. The express purpose of this thesis is first and foremost to provide an empirical basis, employing rigorous, high precision measurement, for predicting the attenuation caused on an earth-satellite link by rainfall in a typical subtropical location. From the results of this measurement, other theoretical methods are developed that can be used to predict slant path rain attenuation for similar systems and locations. The validity of a few well-established theoretical approaches is also tested to see how they conform to what has been measured. A brief analysis of the performance of the microwave link in clear-air is also explored.

1.2 Problem Formulation

Rain attenuation on slant paths is most commonly modelled by procedures outlined in the ITU recommendation P.618-12[8]. The model has remarkable versatility in that it takes into consideration a number of site diversity factors such as $R_{0.01}$, site coordinates and a few others. The model also makes use of an effective path length parameter L_E , which is calculated by incorporating a horizontal reduction factor and a vertical correction factor. However, some studies and measurement campaigns in the tropical regions notably Nigeria and Malaysia, have found the model to be inadequate for predictions in the highest and the lowest portions of rain rate in the tropics [9], [10], [11, 12]. Some model modifications and recommendations have been proposed [13], [14].

A substantial body of work exists on the topic of rainfall and rain effects in Durban and South Africa in general which are equally applicable to subtropical sites notably in Australia and in South America. Over the past decade, studies and measurements have been carried out on various aspects with many useful results. The table 1-1 presents some detail of some of the background work that has been done in Durban.

Table 1-1: Some background studies of rain and rainfall effects in Durban, South Africa

Authors	Focus	Details
Fashuyi & Afullo (2007)	Rain attenuation in South Africa	Modelling from measurements on a terrestrial link at 19.5 GHz
Fashuyi & Afullo (2008)	Rain attenuation prediction	Prediction model for line-of-sight links
Odedina & Afullo (2008)	Secondary radioclimatic factors	Model for terrestrial LOS links in South Africa
Odedina & Afullo (2009)	Secondary radioclimatic factors	Further work on terrestrial LOS links in Southern Africa
Odedina & Afullo (2010)	Scattering by spherical raindrops	Semi-empirical modelling focusing on the spherical shape of raindrops
Alonge (2012)	Drop size distribution modelling	DSD model for terrestrial links and for microwave frequency
Malinga et al (2013)	Computations of rain attenuation	Extensive calculations at microwave and millimetre bands
Alonge & Afullo (2014a)	Queuing Characteristics of rainfall events	Queuing theory analysis of rainfall in equatorial and subtropical Africa
Alonge & Afullo (2014b)	Fractal analysis of rainfall duration	Further queuing theory analysis of rainfall in subtropical Africa
Ahuna & Afullo (2016)	Conversion between integration times	Estimation of conversion factors for Durban data

From the information in the table, it can be deduced that not much work, if any, has been done on earth-satellite links for the subtropics. While most of the theoretical modelling of rain can in principle be applied to slant paths, extensive measurement on slant paths in Durban or any other subtropical location is not reported in literature. Several measurement-based models and results for slant path rain attenuation are however reported for tropical locations such as in [15] for several locations in America, in [16] for Malaysia, [17] for Singapore, [18] and in [19] for Nigeria. All these works focus on the microwave bands for satellite communications and involved one method or the other of correlation of rain rate measurements with received signal measurement over an earth-satellite communication service.

The results unanimously reveal the inadequacy of theoretical prediction models that do not have some kind of basis in actual measurements. All the studies were followed by recommendations and propositions for improvement of the predictions. Such recommendations cannot be applied to the subtropics due to the variation of the pattern and intensity of rain both in time and space, hence the necessity of the present study for as a first step towards a more empirical approach to the prediction of rain attenuation on earth-satellite paths in the subtropics.

1.3 Scope of the Work

This work is specifically focused on carrying out the following:

- To develop a reliable empirical model for measured attenuation on a slant path in a typical subtropical location using the results of several months of high-precision measurements of rain rate and received signal level.
- To validate the measurement results by comparing the results yielded by the measurement model with the results of well-tested theoretical models.
- To derive the Markov properties of the measured slant path rain attenuation and use the same to develop a Markov chain method by which long-term predictions of slant path attenuation can be carried out for seasonal and annual cycles of the subtropical climate.
- To extensively implement the synthetic storm technique for slant paths attenuation using the parameters and rain pattern of a subtropical location and compare the results with that of measurement and with other theoretical approaches.
- To investigate and explain the observation of rain attenuation on a slant path several minutes before precipitation occurs and to translate the delay observed into rain height estimations.

1.4 Thesis Overview

The thesis is organized as follows:

Chapter One is an introduction to the study and it presents the motivation and the problem to be solved.

Chapter Two is a brief review of the relevant literature that forms the basis of the work to be done. It covers previous works on radio propagation effects in general and in subtropical climate. It also covers a brief examination of the theory of satellite communications and the uniqueness of subtropical climate.

Chapter Three reports extensively on the measurement campaign that forms the basis of the work done. It presents the resulting model and its performance compared with some key theoretical models in the same range of fade depth and the corresponding rain rate. It ends with a brief discussion of how total squelching is observed to occur on the measurement link.

Chapter Four reports on the probability density distribution of the measured attenuation and how it forms the state probability matrix for a Markov chain-based prediction model. Fade slope statistics of the measured model is also presented as well as how the state transition vector of the proposed Markov model is derived from the PDF of fade slope.

Chapter Five presents the results of implementing the synthetic storm technique for estimating attenuation on a slant path using the parameters of the measurement link. It also presents an extensive comparison of these results with measurement over a few years.

Chapter six presents a proposed explanation of the phenomenon of observing rain attenuation on a slant path before precipitation occurs. A simple mathematical analysis for extracting event-specific values of rain height from the time lapse is shown.

Chapter seven spells out some conclusions and makes proposals for future work.

1.5 Contributions to Knowledge

This work is expected to make the following contributions to the body of knowledge of the subject matter:

- From the measurement results, an empirical model emerges that forms a first reliable foundation for all slant path rain attenuation prediction methods specifically tailored to subtropical precipitation effects. The model places attenuation occurrence at each rain rate in bounds from minimum to average to maximum. The maximum bound is especially of prime importance, the bound in which link impairment is most serious.
- The work formulates a method for generating rain attenuation data using the temporal stochastic properties of measured data. This has long-term advantages.
- The suitability of various theoretical approaches to slant path attenuation statistics was explored and recommendations made based on which model(s) perform best when compared to actual measured attenuation.

- A unique method for estimating rain height during some particular events was proposed in the work. The method presents an obvious advantage of accuracy over the more widely applied approach of adopting an annual average for attenuation estimation

1.6 Publications

Results of the work reported in the thesis that have also been published in Journals and in conference proceedings are as follows:

- **B.O. Afolayan**, T.J. Afullo and A.A. Alonge, “Seasonal and Annual Analysis of Slant Path Attenuation over a 12 GHz Earth-Satellite Link in Subtropical Africa,” *International Journal on Communications Antenna and Propagation*, Vol. 7 (7), 2017. pp. 572 - 580.
- **B.O. Afolayan**, T.J. Afullo and A.A. Alonge, “Subtropical Rain Attenuation Statistics on 12.6 GHz Ku-Band Satellite Link using Synthetic Storm Technique,” Accepted for publication in the *South African Institute of Electrical Engineers African Research Journal*. May, 2018.
- **B.O. Afolayan**, T.J. Afullo and A.A. Alonge, “Time matching of attenuation-precipitation events on a slant path link,” *Progress in Electromagnetic Research Symposium (PIERS)*, Shanghai, China, 8-11 Aug. 2016. pp. 4967 - 4970
<http://ieeexplore.ieee.org/document/7735810/>
- **B.O. Afolayan**, T.J. Afullo and A.A. Alonge, “Dynamics of Reception Outage due to Subtropical Rainfall on a Satellite TVRO Link”, in *Proceedings of Southern African Telecommunication Networks and Applications Conference*, George, South Africa, 4-7 September, 2016, pp.408-410.
- **B.O. Afolayan**, T.J. Afullo and A.A. Alonge, “A Generalized Analysis of Attenuation-Precipitation Time Lapse Events on Earth-Satellite Microwave Links”, in *Proceedings of 2017 IEEE AFRICON*, Cape Town, South Africa. 18-20 September 2017. pp. 332 – 337.
<http://ieeexplore.ieee.org/document/8095504/>

CHAPTER 2: LITERATURE REVIEW

2.1 Electromagnetic Phenomena

Electromagnetic phenomena are rooted in the interactions and inter-convertibility of electric and magnetic force fields in nature and as generated by electronic circuits. The behaviour of these interactions are best summed up by a system of partial differential equations known as Maxwell's Equations [20], [21]. They are expressed in a simple differential form for free space as:

$$\begin{aligned} a) \nabla \cdot \mathbf{E} &= \frac{\rho}{\epsilon_0} && \text{(Gauss' Law)} \\ b) \nabla \cdot \mathbf{B} &= 0 && \text{(Gauss' Law of Magnetism)} \\ c) \nabla \times \mathbf{E} &= -\frac{\partial \mathbf{B}}{\partial t} && \text{(Faraday's Law)} \\ d) \nabla \times \mathbf{B} &= \mu_0 \left(\mathbf{J} + \epsilon_0 \frac{\partial \mathbf{E}}{\partial t} \right) && \text{(Ampere's Law)} \end{aligned} \tag{2.1}$$

The first equation establishes the direct relation between electric field \mathbf{E} and charge. It implies that the amount of field leaving a point, an area or a volume is proportional to the amount of charge inside it. The second expression implies that magnetic field always exists in such a way that the inward flowing flux over an area is always equal to the outward flowing flux. Hence, a magnetic configuration with a single pole is not possible. The third expression describes how a time-variant magnetic field gives rise to an electric field that acts in such a way as to oppose it. The last equation describes how a changing electric field in a closed loop gives rise to a magnetic field that is proportional to the current. Intrinsic properties of any electromagnetic field can be extracted by obtaining real solutions of the above system of partial differentials.

In its most basic form, modern radio communication is dependent on the ability to build electronic circuits that will produce and sustain an outflow of electromagnetic energy in the form of plane-polarized waves. Such a waveform will flow out of any electronic circuit with frequency in the range of a few thousands Hertz [22]. Above a certain frequency, the alternate cycles of build-up and collapse of electromagnetic energy in and around the circuit will no longer be able to occur fast enough without energy escaping into the surrounding medium. Such a circuit is thus able to serve as a transmitter and it can be matched with the proper antenna configuration and an equally matching receiving antenna circuit can be built. The radio wave propagates as plane-polarized waves made up of transverse electric and magnetic fields. Its power density in Watts per metre squared as it travels along the z -axis is related to the Poynting vector as illustrated in Figure 2-1 given by the cross product

$$\mathbf{S} = \mathbf{E} \times \mathbf{H} \tag{2.2}$$

where \mathbf{E} is the electric field vector in Newtons per Coulomb (NC^{-1}) and \mathbf{H} is the magnetic field vector in Amperes per meter (Am^{-1}). The direction of \mathbf{E} determines the polarization of the wave, which in this case is regarded as a radio signal encoded with intelligent information. The level of fidelity of the signal that will arrive at the receiver is directly related to S .

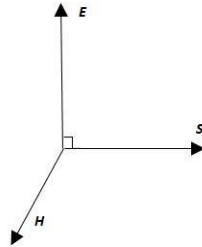


Figure 2-1: Poynting Vector

As the radio wave progresses from the transmitter, we can only reckon its energy in the far field region. It is ideally assumed that they are radiated in concentric spheres away from the transmitter from a point source. As the sphere gets bigger, its surface area increases with the square of the distance away from the source/transmitter. The power of the transmitter remains the same however, hence it is the same power that is continually being spread out over a larger surface. The result of the spreading out is that the power density S reduces in proportion to $1/d^2$ and so does the power density of the received signal.

Using the foregoing geometry, a basic estimate of the value of S at a receiver distance d away will be as given by equation 2.3.

$$S = G \frac{P_T}{4\pi d^2} \quad (2.3)$$

where G is the gain factor of the receiver and P_T is the power density originally transmitted.

2.2 The Radio Frequency Spectrum

Wireless radio communication systems utilize a section of the electromagnetic wave spectrum generally referred to as the radio frequency spectrum [23]. This falls in the range 3 KHz to 3 THz. The administration and designation of this frequency range for various services is done by international bodies such as the Institute of Electrical and Electronic Engineers (IEEE) and the United Nations-affiliated International Telecommunications Union (ITU). They are responsible for harmonizing the licensing of these bands for various services worldwide in order to prevent channel conflicts, interference and disputes [24]. The ITU version of the official nomenclature of the various subdivisions of the radio frequency spectrum is presented in Table 2-1.

Table 2-1: ITU Nomenclature for radio communication frequency Bands

Nomenclature	Abbreviation	Frequency Band	Wavelength
Very Low Frequency	VLF	3 to 30 kHz	10 to 100 km
Low Frequency	LF	30 to 300 kHz	1 to 10 km
Medium Frequency	MF	300 to 3000 kHz	100 to 1000 m
High Frequency	HF	3 to 30 MHz	10 to 100 m
Very High Frequency	VHF	30 to 300 MHz	1 to 10 m
Ultra High Frequency	UHF	300 to 3000 MHz	10 to 100 cm
Super High Frequency	SHF	3 to 30 GHz	1 to 10 cm
Extremely High Frequency	EHF	30 to 300 GHz	1 to 10 mm
Terahertz Frequency	THF	300 to 3000 GHz	0.1 to 1 mm

The frequency band of interest in this study and in most rain attenuation studies is officially designated by the ITU as the Super High Frequency band. In terms of its wavelength range, it is commonly referred to as part of the Microwave band. The band is reserved for such services as microwave devices, applications, wireless local area networks (LAN) and earth-satellite communication services such as television and radio broadcasting. Other sub-designations are made in this band as their frequencies are allocated for specific services. Examples of SHF subdivisions relevant to satellite communications services such as Internet access, TV and radio broadcasting, radar and weather services and so on, are shown in Table 2-2. The band is of special interest for rain attenuation studies because the range of raindrop diameters falls almost exactly within its range of wavelengths as shall be seen in section 2.4.3.

Table 2-2: Microwave Satellite Communication Bands

Band	Downlink Frequency	Uplink Frequency
C	3.625 - 4.2 GHz	5.85 - 6.425 GHz
X	7.25 - 7.75 GHz	7.9 - 8.4 GHz
Ku	10.95 - 12.75 GHz	13.75 - 14.5 GHz
Ka	20.2 to 21.2 GHz	30.0 to 31.0 GHz

2.3 Overview of Losses in Radio Propagation

Preserving the fidelity and power content of a transmitted signal as much as possible as it travels from transmitter to receiver is the single most significant design aim of any wireless communication system. The fidelity of the received signal is highly dependent on this and so is the fidelity of the encoded content be it voice, data or video. Preserving 100% of the transmitted power is made technically impossible by several identifiable sources of loss that the signal is bound to encounter along its path both in nature and

otherwise. The following is a general look at the more significant types of loss that a radio wave will encounter along its path.

2.3.1 Free Space Path Loss

When the intervening distance between the transmitting antenna and the receiving antenna is made up entirely of a vacuum, the loss in signal power is then not due to any of the natural contents of the troposphere. Such a loss is the Free Space Loss (FSL). As described in 2.1.1, the simplest and most ideal configuration of a transmitting antenna is a point source propagating electromagnetic energy through space in concentric spheres away from a point [25]. From equation 2.2, we assume a system of isotropic receiving and transmitting antennas of gains G_R and G_T respectively equal to unity. Then,

$$P_R = \frac{P_T}{4\pi d^2} \quad (2.4)$$

where P_R is the received power, P_T is the transmitted power and d is the intervening distance.

It can be shown that the Free Space Loss is proportional to the square of the distance d and the square of the frequency of the radio signal as given by equation 2.5.

$$FSL = \left(\frac{4\pi df}{c}\right)^2 \quad (2.5)$$

where f is frequency (in Hz) being transmitted and c is the speed of electromagnetic waves in ms^{-1} . It is customary to express 2.5 in the more convenient unit of decibels (dB), in which case it takes the form:

$$\begin{aligned} FSL (dB) &= 10 \log_{10} \left(\left(\frac{4\pi df}{c} \right)^2 \right) \\ &= 20 \log_{10} \left(\frac{4\pi df}{c} \right)^2 \\ &= 20 \log_{10} d + 20 \log_{10} f + 20 \log_{10} \frac{4\pi}{c} \end{aligned} \quad (2.6)$$

The last term of equation 2.6 is obviously a constant for a free space medium. When f is in Hertz and d in meters, it is -147.33. If we adopt the dimensions GHz for f and km for d as often done for microwave links, the constant becomes 92.45.

2.3.2 Refractive Loss

The homogeneity of space as a propagation medium implies that radio waves will experience no refraction. The troposphere offers no such homogeneity. Hence, there is a measurable radio refractive index of the troposphere and it is typically greater than unity. The wavelength, and by implication

frequency of the signal plays a major role in this type of loss. The refractive index of the troposphere is inversely proportional to height above the ground and it has been shown that this refractive index becomes significant above a wavelength of 10 m. This is due to the fact that the wavelength above this becomes similar to the distance over which variations in temperature, pressure and humidity changes in the atmosphere [26], [27]. In a general sense, radio refractivity N is given by equation 2.7.

$$N = \frac{77.6}{T} \left(p + \frac{4810e}{T} \right) \quad (2.7)$$

where p is the atmospheric pressure, e is water vapour pressure and T is the temperature. At a given height above the ground, the refractive index n is given by equation 2.8.

$$n = 1 + (N \times 10^{-6}) \quad (2.8)$$

Refractive loss is very significant at certain wavebands for terrestrial propagation.

2.3.3 Loss to Vegetation

Studies have established that trees and foliage cover have a scattering effect on electromagnetic waves propagating through them [28]. This loss type is highly dependent on the type of vegetation in the propagation path. The moisture content of the leafy parts of the vegetation also plays a part. As vegetation changes with the seasons of the year, a seasonal variation in loss levels to vegetation also exists [29]. Another factor is the path taken by the radio waves through the vegetation. An ITU study group predicted foliage loss by carrying out extensive measurements at the UHF band and at foliage depth below 400 m. Generally, foliage loss is given in [30] by equation 2.9

$$L_{foliage} = 0.2f^{0.3}d^{0.6} \text{ (dB)} \quad (2.9)$$

where f is the frequency in MHz and d is the foliage depth below 400m.

A separate study carried out by the European Union research group [31] resulted in a double specification model that presents separate methods of estimating foliage loss under two conditions: when the trees are “in leaf” and when they “are out of leaf”. The loss under these conditions is given by equation 2.10.

$$L_{foliage} = \begin{cases} 26.6f^{-0.2}d^{0.5} & \text{Out of leaf} \\ 15.6f^{-0.09}d^{0.26} & \text{In leaf} \end{cases} \quad (2.10)$$

where f is the frequency in MHz and d foliage depth above 200 m. the COST235 model is based on measurements at 9.6 to 57.6 GHz hence it is more applicable at the higher frequency than the ITU model.

2.3.4 Atmospheric Gas Loss

Radio waves propagating through a clear atmosphere are subject to attenuation by absorption in atmospheric gas molecules. Measurements show that the attenuation due to each gas peaks around certain frequencies. The two gases of particular interest are water vapour and oxygen. This is due to their relative abundance in the atmosphere. A number of other gases such as O_3 , NH_3 , SO_2 and NO_2 are also responsible for signal attenuation by absorption but to a significantly lesser extent. {Marcus, 2005 #126} showed that the frequency at which attenuation due to the gases attain peaks coincides with the mechanical resonance frequencies of the gas molecules.

Across the radio wave spectrum, the two gases responsible for the most severe absorption and attenuation effects in the atmosphere have their unique absorption lines forming peaks around certain frequencies [32]. It is imperative for system design to avoid transmission at such frequencies as much as is practicable. As shown in figure 2-2, absorption by oxygen peaks at 60 GHz with a specific attenuation of about 20 dB/km and water vapour at 20 GHz with a specific attenuation of 0.5 dB/km. These are the most significant frequencies at which atmospheric gas absorption takes place. Atmospheric gas absorption above the 100 GHz frequency threshold is more complicated. But [33] was able to demonstrate that absorption by water vapour also peaks at 183 GHz and 325 GHz.

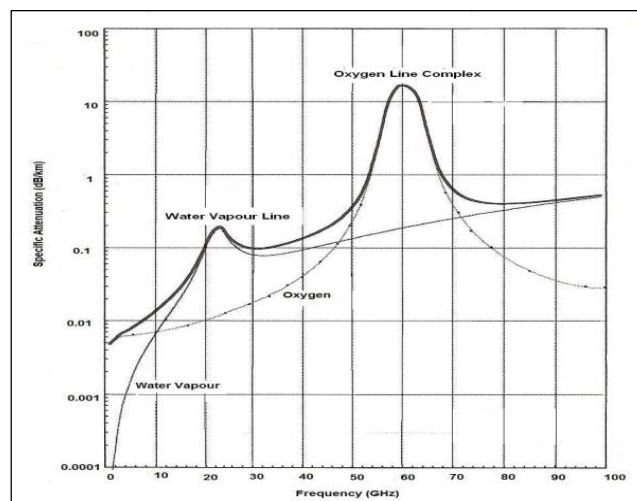


Figure 2-2: Absorption by water vapour and oxygen showing characteristic peaks at some frequencies [32]

2.4 Fundamentals of rain structure and rain impairment of radio links

2.4.1 Scattering and absorption in rain

The interaction of radio waves with a rain medium inevitably causes the parts of its electromagnetic energy getting absorbed by the raindrops. Another portion of the electromagnetic energy gets scattered in multiple directions [34]. While the absorbed part is lost as heat, the scattered part manifests as a form

of noise at the receiver and in severe cases this noise is capable of hampering the reception of the desired signal [35], [36]. Figure 2-3 illustrates the basic process that takes place when a radio wave encounters raindrops. The observed effects are generally described as absorption, forward scattering, side scattering and back scattering. Evidently, the power content of the emergent wave will only be a fraction of that of the incident wave. The sum total of all these effects is what is referred to as rain attenuation.

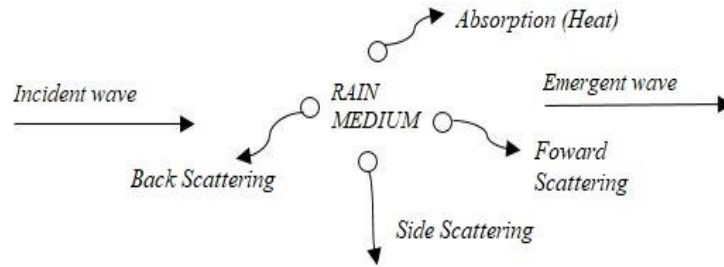


Figure 2-3: Dynamics of absorption and scattering in rain

The dynamic and extent of absorption and scattering by raindrops depends on several factors. An especially significant factor is how the wavelength of the radio compares to the size of the raindrops. The closer the wavelength is to raindrop size the more severe the scattering and absorption process will be [36],[37]. This is why frequency is a dominant factor in attenuation prediction. Other factors that will influence the absorption and scattering process is the shape of the raindrops and the contents of the water [38]. The total path attenuation experienced by the radio signal is an integration of the amount of scattering and absorption that occurs in each raindrop as it passes through in the rain medium since the wave does not recover its energy after passing through each raindrop.

2.4.2 Radio waves in a water medium

Under the right conditions, electromagnetic radiation is known to be capable of propagating through all known physical materials as well as through space [25]. The intrinsic wave propagation parameters of the medium can be used to predict the resultant effect of the medium on the radio wave. In terms of wave propagation, a medium can either be a conducting medium or non-conducting dielectric material. This classification is made by computing such parameters as the conductivity σ of the medium and its loss tangent, which is given by the quotient in equation 2.11.

$$\text{Loss Tangent} = \frac{\sigma}{\omega \epsilon} \quad (2.11)$$

where ω is the angular frequency of the wave and ϵ is the electric permittivity of the medium. The medium will pass the test for a good conductor if $\sigma \gg \omega \epsilon$ or the quotient in equation 2.11 is much greater than unity [39]. For the purpose of this test, it is rational to use the frequency 10 GHz. This is because

it translates into a wavelength of 3 mm which is generally regarded as a threshold size of raindrops above which rain impairment becomes significantly severe [2].

The relative permittivity of rain water ϵ_r is 81. The conductivity of water is 10^{-4} S/m. Permittivity of free space ϵ_o is 8.85×10^{-9} F/m at 10 GHz or 10^7 Hz. ω is given by

$$\begin{aligned}\omega &= 2\pi f \\ &= (2\pi \times 10^9) \text{ rad/s}\end{aligned}$$

Given these values, the loss tangent is 2.2×10^{-5} . Since $2.2 \times 10^{-5} \ll 1$, rain water is to be classified as a poor conductor and a lossy dielectric, which in part forms the root cause of rain attenuation of electromagnetic signals.

2.4.3 Microphysical Structure of Rain

Rain is the liquid product of condensed water particles in the atmosphere as released by clouds during the precipitation process [40]. The microphysical structure of raindrops, which refers to their size, their aerodynamic properties and so on is vital to rain attenuation prediction. The actual length of water medium that a radio wave will actually traverse depends on the aggregate diameter of raindrops in the medium [2].

Based on studies by several authors [41], [36], the diameter of raindrops range from 0.1 mm to 7 mm. Drops smaller than this range are considered to belong more in the class of vapour with regards to their effects on communication links. Above this range of diameter, the body of water tends not to stay together long enough to be considered a single drop. The laws of surface tension, gravity and aerodynamic forces will cause them to break up into two or more drops [42]. At the lower end of the size spectrum, raindrops are approximately a perfect sphere. Departure from a perfect sphere is not observed until drop diameter D is greater than 0.3 mm [41].

In the most widely applied drop and shape model, the Pruppacher-Pitter model [42], a falling raindrop begins to flatten at the base as its diameter increases. The eventual shape is described as the oblate spheroid. It acquires a horizontal axis that is longer than its vertical axis and a concave depression appears at the centre under it. The oblate spheroid shape is important for an accurate integration of the length of water traversed by the radio wave. It also has implications for the polarization of the radio wave. Since the horizontal axis is longer in a drop of this shape, a horizontally polarized wave is likely to experience slightly more impairment than a vertically polarized one [43], [44].

As raindrops fall towards the ground, measurements have shown that they attain a maximum velocity which they then maintain as they fall. This terminal velocity is determined by their size, which follows

from the law of momentum. A bigger size implies a higher mass which also implies a higher momentum. The Figure 2-4 shows the relationship between drop diameter and terminal velocity as fitted from experimental measurements by several authors. The results show a remarkable agreement between the various models in the 0 – 6 mm range of drop diameter. Terminal velocity peaks at about 9 m/s for raindrops of 5 mm in all the models.

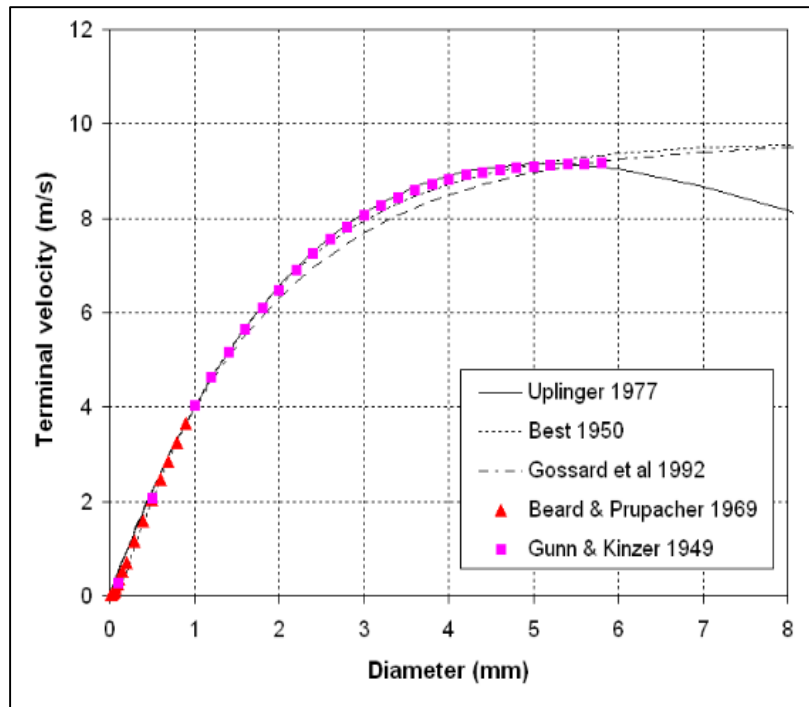


Figure 2-4: Dependence of terminal velocity of raindrops on diameter [45]

2.4.4 Rainfall Rate

The quantitative reckoning of the intensity of rainfall is generally referred to as rain rate. according to [45], a raindrop of mass M_i will make a contribution R to the rain rate during the precipitation event given by equation 2.12.

$$R = M_i(\mu_v - \mu_u) \quad (2.12)$$

where μ_v is the terminal velocity of the drop and μ_u is the updraft rate. In a unit volume of occupied by particles of the same size, the value of rain rate will be given by equation 2.13.

$$R = \frac{4}{3}\pi\rho a^3 N(\mu_v - \mu_u) \quad (2.13)$$

where N is the number of drops in the volume and ρ is the density of water.

In practice, the size of drops will vary widely as discussed earlier, hence a more realistic approximation of rain in a unit volume of air is needed in form of an integral over all drop sizes such that

$$R = \frac{4}{3}\pi\rho \int_{a=0}^{a=\infty} a^3 N(a) v(a) da \quad (2.14)$$

where $v(a)$ is the terminal velocity of a raindrops of radius a . $N(a)da$ is the number of drops in the range between a and $(a + da)$ per unit volume [45]. Given that value of ρ in g/cm^3 is unity for water the dimension of R is mm/h . When a known mathematical distribution is adopted for the drop size it can be shown that the equation above becomes[2],

$$R = 6\pi \times 10^{-4} \int_0^{\infty} D^3 N(D) v(D) d(D) \quad (2.15)$$

D is the drop diameter in mm , $N(D)$ is the is the adopted mathematical model of the drop size distribution in $\text{mm}^{-1}\text{m}^{-3}$ and $v(D)$ is the terminal velocity of drop of diameter d .

2.4.5 Rain Rate Exceedance

The random nature of rain both in space and time makes it imperative to carry out a rigorous statistical analysis of rain intensity values for communication link planning and deployment. This randomness is exhibited in the fact that around the globe rainfall intensity and frequency varies widely from location to location so much so that it is highly unlikely to experience the exact same level and pattern of rain impairment in any two locations. However, the similarity within various regions of similar climactic characteristics is good enough to make reliable system planning and deployment possible.

Based on popular Service Level Agreements (SLAs) between operators and users in a wide variety of industries for service availability, communication links are designed for 99.99% availability in a year[46], [47]. This implies that 0.01% downtime is the acceptable maximum. Thus, when planning for rain impairment on communication links, designers are interested in the rain rate exceeded at that particular location in 0.01% the time ($R_{0.01}$). This value is easily obtained from the yearly Cumulative Distribution Function (CDF) of rain rates measured in the location for the year. Point rainfall data of the location at 1-minute integration time is considered ideal for determining $R_{0.01}$. The longitudinal duration of rainfall is the demonstrated in the ITU recommendation document P.3.837-7[48], which details a method for estimating at $R_{0.01}$ for locations and regions where point rainfall data may not be available [49], [32].

A more recent approach to rain rate statistics is the application of queuing theory. [50] evolved a model that assumes that rainfall regimes occur as queues. By extracting the queuing parameters of rainfall data obtained from rain gauge and disdrometer measurements in Durban, South Africa and Butare, Rwanda, they proposed a method for mathematically simulating cumulative distribution functions of rain rate from which the $R_{0.01}$ can be extracted.

2.4.6 Classification of Rain

Rainfall events are classified according to the highest rain rate spike recorded during the event. The broader classification of rain as Stratiform rain and Convective rain takes into consideration the general type of cloud formation, duration of precipitation and rain intensity [51], [52], [53]. Stratiform rain occurs due to smaller and weaker cloud formations which release lighter rainfall, but the events usually over a relatively wide area. Convective rain results from stronger more compact cloud formations. The exhibit higher intensity but often less duration and coverage.

In [12], three rain classifications were established for tropical rainfall that are more specific. They are drizzle, shower and thunderstorm. They associated specific rain rate ranges to each classification. However, a more applicable classification for subtropical rain is the classification by [54], [4] and [55] which are based on extensive rain gauge and disdrometer measurements campaigns in various locations in the region. Four rain regimes emerged from these works namely drizzle (<5 mm/h), widespread (5 mm/h – 10 mm/h), shower (10 mm/h – 40 mm/h), and thunderstorm (>40 mm/h).

2.4.7 Some Characteristics of Subtropical Climate

Subtropical regions are so classified according to the Koppen climactic classification. As illustrated in the Figure 2-5, they lie mostly within the 25° and 35° latitudes both north and south. This places them next to tropical regions in most cases. Locations in this region experience hot summer months with high humidity. During the cold winter months, average temperature in the subtropics can take on values from 0° to 18° and in the warm summer months, it can be as high as 22°. Subtropical climate features all the four seasons of the calendar year namely spring, summer, winter and autumn.

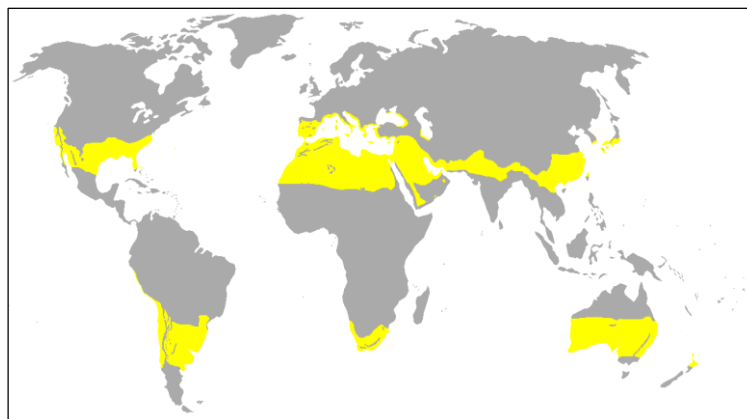


Figure 2-5: Subtropical Regions of the world (indicated in bright yellow) using the Koppen climate classification [1].

The annual rainfall in an average subtropical location such as Durban is expected to exceed 1000 mm. Durban is a coastal city located on 29.86°S and 31.02°E. Its climate and that of much of the southern Africa region is heavily affected by the Mozambique current and the Agulhas current from over the

Indian Ocean on the eastern coast and the Benguela current from the Atlantic Ocean on the western coast.

Table 2-3: Months of the seasons in Durban

Season	Months
Summer	November to February
Autumn	March to May
Winter	May to September
Spring	September to November

Rainfall characteristics of Durban has been studied extensively. A few of these have been cited earlier in this chapter. Rain attenuation contour maps for South African cities were developed by [56] and [57] using hourly and five-minute rain rate data from the South African Weather Service (SAWS). Conversion methods for different rain rate integration times using rain gauge and disdrometer data for Durban and other south African cities was exhaustively modelled by [58] and [59]. In [60] and [61], rain cell size models fitted for Durban based on rain gauge data from several spots in Durban as well as disdrometer data are reported. [54] developed drop size distribution models fitted to Durban data using Kernel estimates [3]. [50] and [62] reports on extracting queuing parameters from rain rate data from Durban and Butare, Rwanda and they were able to simulate rain rate time series in form of queues.

2.5 Theory and models of Slant Path Rain Attenuation Prediction

As earlier mentioned, attenuation of radio waves by rain is an integral sum of the scattering and absorption effects at each of the raindrops in the medium. Long term prediction of this phenomenon is a very important source of loss especially on microwave links and efforts to make precise, reliable predictions for it is as old as radio communication itself. The intrinsic characteristic that makes this task especially tedious is that like rain itself, rain attenuation is non-deterministic. It exhibits complete randomness not only in time but also from place to place. Like other stochastic parameters, multiple approaches are required to be able to come up with appropriate predictions that will be useful for designing systems whose fidelity is directly dependent on it.

The work reported in [63] laid the foundation for theoretical prediction of rain attenuation using perturbation theory calculations to estimate the scattering and absorption of electromagnetic waves on impact with small particles in general. [64] applied this approach to scattering and absorption by raindrops in particular over known path lengths. Building on advances in rain rate modelling and prediction, [65] proposed a good model for specific attenuation (that is, the rain attenuation per unit distance over a link). The model established the power-law relation between the specific attenuation and rain rate calculating the coefficients according to frequency range. [66] also proposed a power-law model with suggested correction factors for better regional fit. The early models were sufficient for

prediction for the temperate regions, being results of adopting rain rate distributions in those regions. However, they mostly underestimate rain attenuation on both terrestrial and slant paths in tropical and subtropical regions. A few of the more relevant prediction models used for comparison purposes in this thesis are as follows.

2.5.1 Olsen Power Law Model

The power law relation known as the Olsen Model [65] that relates the attenuation per unit distance in a medium (Specific Attenuation) to the rain rate given as

$$\gamma = kR^\alpha \quad (2.16)$$

The accuracy of this expression depends on the validity of the frequency-dependent coefficients k and α . The coefficients were initially calculated for various frequency ranges from regression procedures carried out using experimental data. Theoretical estimates of k and α presented in this work for 1 to 1000 GHz. The values were obtained from Mie scattering estimations of scattering and absorption. The frequency dependence of k and α under the Olsen Model for the frequency range 0 to 180 GHz in four expressions for each coefficient are [65]

$$\left. \begin{aligned} k &= 6.39 \times 10^{-5} f^{2.03} && \text{for } f < 2.9 \text{ GHz} \\ k &= 4.21 \times 10^{-5} f^{2.42} && \text{for } 2.9 \text{ GHz} \leq f \leq 54 \text{ GHz} \\ k &= 4.09 \times 10^{-2} f^{0.699} && \text{for } 54 \text{ GHz} \leq f \leq 180 \text{ GHz} \\ k &= 3.38 f^{-0.151} && \text{for } f > 180 \text{ GHz} \end{aligned} \right\} \quad (2.17)$$

$$\left. \begin{aligned} \alpha &= 0.851 f^{0.158} && \text{for } f < 8.5 \text{ GHz} \\ \alpha &= 1.41 f^{-0.0779} && \text{for } 8.5 \text{ GHz} \leq f \leq 25 \text{ GHz} \\ \alpha &= 2.63 f^{-0.272} && \text{for } 25 \text{ GHz} \leq f \leq 164 \text{ GHz} \\ \alpha &= 0.616 f^{0.126} && \text{for } f > 164 \text{ GHz} \end{aligned} \right\} \quad (2.18)$$

The Olsen model formed the initial ITU-R model for specific attenuation.

2.5.2 The Lin Model

The Lin model estimates total path attenuation. It is an early application of the power-law model of specific attenuation given by [64]

$$A_T = kR^\alpha L K_r \quad (2.19)$$

L is the propagation path length in km and K_r path reduction factor derived by [65] as a result of measurements on 11 GHz microwave link to account for the observation that attenuation is not necessarily in direct proportion to path length.

K_r is given by

$$K_r = \frac{1}{1+L\left(\frac{R-6.2}{2636}\right)} \quad (2.20)$$

However, this estimate of K_r is only applied for rain intensity R greater than 10 mm/h. For lower rain intensity, it is taken to be unity.

2.5.3 The Crane (Global) Model

The Crane model [31] is a statistical rain attenuation model developed for terrestrial and slant paths based on the Olsen power law model for specific attenuation. Later improvements on the initial model was developed culminating in the Crane Global Model [66]. According to this model, total path attenuation over a link of path length D is given by the equations 2.21 and 2.22

$$A_T = kR^\alpha \left(\frac{e^{y\delta(R)} - 1}{y} + \frac{e^{zD} - e^{y\delta(R)}}{z} \right) \text{ for } \delta(R) < D < 22.5 \text{ km} \quad (2.21)$$

$$\text{and } A_T = kR^\alpha \left(\frac{e^{y\delta(R)} - 1}{y} \right) \text{ for } 0 < D < \delta(R) \quad (2.22)$$

where R is the rain rate in mm/h.

The model employed a path integral that involved piecewise exponentials over the path length. The rain rate-dependent constants were empirically derived and their values are given by the system of equations (2.23) summarised as follows:

$$\left. \begin{aligned} \delta(R) &= 3.8 - 0.6 \ln(R) \\ c &= 0.026 - 0.03 \ln(R) \\ B &= 0.83 - 0.17 \ln(R) \\ \mu &= \frac{B}{\delta(R)} + c \\ y &= \alpha u \\ \text{and } z &= \alpha c \end{aligned} \right\} \quad (2.23)$$

Equations 2.21 and 2.22 are given for propagation path length up to 22.5 km. For greater distances, it is recommended to estimate for 22.5 km and multiply by a factor $D/22.5$.

2.5.4 The Garcia-Lopez Model

Garcia-Lopez and Peiro in [67] built further on the idea of implementing a path reduction factor when estimating total path attenuation by proposing a model, also founded on the power law relationship of specific attenuation, and introducing a special path reduction model that takes into consideration the spatial variation of rainfall in different locations around the globe.

According to this model, for point rain rate at integration time t for $p\%$ of the time, rain attenuation on the path is [67]

$$A(p\%) = kR_t^\alpha LK_G \quad (2.24)$$

where L is the path length and K_G is the proposed reduction factor. K_G is a function of the integration time of R and the spatial structure of rain at the location. It is given by

$$K_G = \frac{1}{a+[L(bR_t+cL+d)]/e} \quad (2.25)$$

The parameters a , b , c , d and e fitted for various regions were presented by [68]. One of the regions listed is Australia, which presents a fairly good approximation for conditions in subtropical Africa.

2.5.5 The ITU-R Model

The in-force ITU-recommended procedure for estimating the rain attenuation on a slant path is outlined in the recommendation document ITU-R P.618-12 [8]. The procedure employs a few parameters of the link and the location as input and adopts a simple slant path profile shown in figure 2-6 below. A brief outline of the recommendations is as follows.

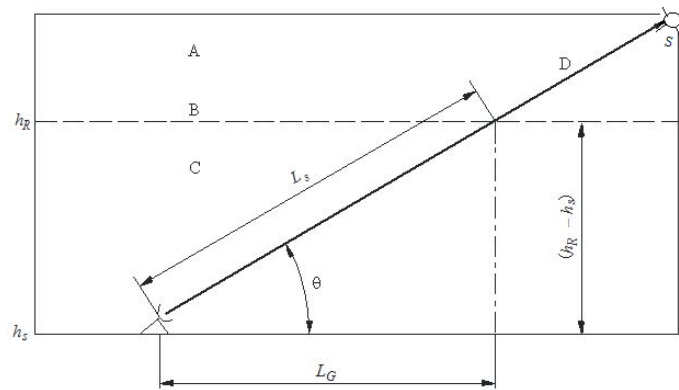


Figure 2-6: Slant Path Profile[8]

From the figure, region A is the region of frozen precipitation (melting layer), B is the rain height while C is the region of liquid precipitation. For elevation angle θ above 5° , the nominal slant path length L_s in km is given by

$$L_s = \frac{(h_R - h_s)}{\sin \theta} \quad (2.26)$$

For smaller elevation angles (less than 5°),

$$L_s = \frac{2(h_R - h_s)}{\left(\sin^2 \theta + \frac{2(h_R - h_s)}{R_e} \right)^{1/2} + \sin \theta} \quad (2.27)$$

where h_s is the height of the earth station above sea level in km, θ is the elevation angle of the receive antenna, R_e is the effective radius of the earth - which is a constant at 8500 km and h_R is the rain height in km given by

$$h_R = h_0 + 0.36 \quad (2.28)$$

h_0 is the height of the zero-degree isotherm whose value for any earth station can be read off a map in [69].

The ITU-R model adopts the simple form of the power law model in equation 2.16 for specific attenuation but proposes a more elaborate procedure for estimating the frequency-dependent k and α coefficients outlined in [70]. The coefficients are given by

$$k = [k_H + k_V + (k_H - k_V) \cos^2 \theta \cos 2 \tau] / 2 \quad (2.29)$$

$$\alpha = [k_H \alpha_H + k_V \alpha_V + (k_H \alpha_H - k_V \alpha_V) \cos^2 \theta \cos 2 \tau] / 2k \quad (2.30)$$

where τ is the polarization tilt angle. Values of the horizontal and vertical elements of k and α are readily available for the frequencies 1 to 1000GHz in [70].

The total path attenuation in this model is given by the product

$$A = \gamma L_E \quad (2.31)$$

where γ is the specific attenuation and L_E is the effective length of the path. The effective length is the length of the link obtained after applying a horizontal reduction factor $r_{0.01}$ and a vertical adjustment factor $V_{0.01}$. $r_{0.01}$ is given by

$$r_{0.01} = \frac{1}{1 + 0.78 \sqrt{\frac{L_G \gamma_R}{f}} - 0.38 (1 - e^{-2L_G})} \quad (2.32)$$

From the figure, L_G is the ground projection of the slant path length and it is given by

$$L_G = L_S \cos \theta \quad (2.33)$$

To proceed with estimating the vertical adjustment factor $v_{0.01}$, it is required to test for the value of an angular parameter ζ given by

$$\zeta = \tan^{-1} \left(\frac{h_R - h_s}{L_G r_{0.01}} \right) \quad (2.34)$$

When this value is greater than the elevation angle θ , rain length parameter L_R is given by

$$L_R = \frac{L_G r_{0.01}}{\cos \theta} \quad (2.35)$$

Otherwise, it is equal to L_S as given in equation 2.26.

Also required as input into the $v_{0.01}$ calculations is another angular parameter χ . When the earth station is on latitude φ and φ fulfills the condition $|\varphi| < 36^\circ$, then χ in degrees is given by

$$\chi = 36 - |\varphi| \quad (2.36)$$

Otherwise, χ is taken as zero. Thus we can obtain the vertical adjustment factor as

$$v_{0.01} = \frac{1}{1 + \sqrt{\sin \theta} \left(31 \left(1 - e^{-(\theta/(1+\chi))} \right) \frac{\sqrt{L_R \gamma_R}}{f^2} - 0.45 \right)} \quad (2.37)$$

The effective path length L_E is given by the product

$$L_E = L_R v_{0.01} \quad (2.38)$$

The horizontal reduction factor and the vertical adjustment factor are peculiar to each link and location. This model bears a high level of accuracy for many locations on the globe but it has proved to be slightly inadequate in several locations outside the temperate regions that exhibit significantly higher rain rate exceedance levels. A few authors such as [71] and [72] have proposed adjustments for the model and for the correction factors.

2.6 Overview of Earth-Satellite Communication

Satellite communication links depend on transponders carried on artificial satellites orbiting the earth several thousand kilometres from the ground. The immense advantages of such a system over a terrestrial link are obvious. A major advantage is the enormous skip distance between transmitter and receiver that is made possible [73], [74]. With a satellite link, the total link distance possible between a transmitter on the ground and the eventual receiver can be up to 50% of the circumference of the Earth. In practice however, only about 40% of the Earth's circumference can be covered by a single satellite.

This implies that just 3 satellites separated by 120° of longitude can cover the entire planet with the same communication service [75].

Communication satellites are designed to carry high versatility transponders that are capable of receiving intelligent signals from a ground station and rebroadcast over a very wide area on the ground. The area covered by the beam is called its footprint (Figure 2-7). Any well-matched receiving antenna within its footprint can be used to capture the rebroadcast.

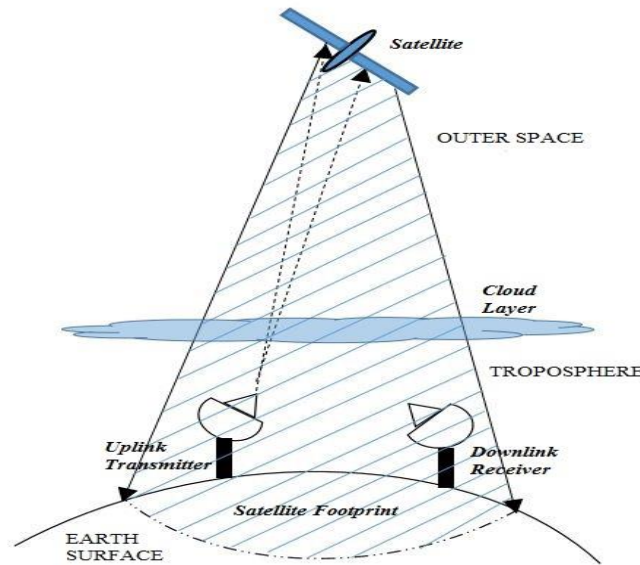


Figure 2-7: Satellite Link profile

2.6.1 Geostationary Orbits

An artificial satellite located in an orbit of distance 35,786 km from the ground as measured around the equator is called a geosynchronous or geostationary satellite. This is because at that height, the outward centrifugal force on the satellite is balanced out by the pull of the Earth's gravitational field (Figure 2-8). The results of the balance of forces is an orbit in which the satellite beacon is able to stay focused over the same location indefinitely. To achieve a geosynchronous altitude, the gravitational force must be equal to the centripetal force on the satellite such that [76],

$$F_C = F_G \quad (2.39)$$

If m is the mass of the satellite, then according to Newton's second law of motion, the equation 2.39 can be written as

$$ma_C = ma_G \quad (2.40)$$

Since m is equal on both sides, the important consequence of equation 2.40 is to obtain a point at which this centripetal and the gravitational acceleration are equal. Now,

$$a_c = \omega^2 r \quad (2.41)$$

where ω is the angular velocity of a satellite and r is the radius of the orbit from the centre of the Earth. Also,

$$a_G = \frac{GM}{\omega^2} \quad (2.42)$$

where G is the gravitational constant which equals $6.674 \times 10^{-11} \text{m}^3 \text{kg}^{-1} \text{s}^{-2}$ and M is the mass of the Earth. It is customary to make use of the known value of the product in the numerator of equation 2.42. The product is known as the Geocentric Gravitational Constant μ and its value is stated precisely as $3.986004418 \times 10^5 \text{ km}^3 \text{s}^{-2} \pm 0.0008$. Equating 2.41 and 2.42, we obtain

$$r = \sqrt[3]{\frac{\mu}{\omega^2}} \quad (2.43)$$

Whether a satellite will remain in a geostationary orbit depends on one single precondition: Its period in orbit and that of the earth must be equal. The earth has a period of one sidereal day as it rotates on its axis which equals 86164.09054 s. The satellite must be given this same period in orbit. With this in mind, we can launch the satellite to have an angular speed ω that makes this precondition possible. ω is the angle that the satellite must rotate through per second. If it makes a full revolution of 2π radians in one sidereal day then [76],

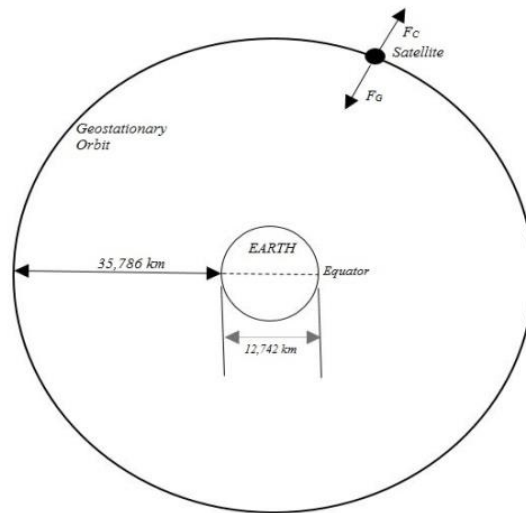


Figure 2-8: Geostationary satellite orbit relative to Earth's geometry

$$\begin{aligned} \omega &= \frac{2\pi}{86164.09054} \text{ rads}^{-1} \\ &= 7.2921 \times 10^{-5} \text{ rads}^{-1} \end{aligned}$$

With this value of ω , we can solve the equation 2.43 for orbital radius r to get 35,786 km.

2.6.2 Link budgeting for Downlink Reception

For rain attenuation studies and measurement, link budgeting is concerned with the losses and gains at the receive antenna. This does not differ much from terrestrial links except for the fact that free space loss (FSL) is much higher due to the much larger distance between the transponder and the earth station. For the purpose of link budgeting, the satellite transponder is regarded as an isotropic transmitter radiating energy equally in all directions with a power flux density given by [77]

$$P_i = \frac{P_s}{4\pi r^2} \quad (2.44)$$

where P_s is the power outflow or (energy outflow per unit time). The power of the transmitter is in practice highly directive and it is designed to be maximum in the direction of the receive antenna. If the power in that direction is P_m , then the gain of the transmitting antenna is the ratio

$$G = \frac{P_m}{P_i} \quad (2.45)$$

The Equivalent Isotropic Radiated Power (EIRP) of any communication satellite at a location is usually made available by the satellite operator. Ordinarily, EIRP is the product of P_i and antenna gain G . But in log units (dBW), it is a sum of the two parameters. There are only two reasons why the power received on the ground is always different from EIRP. The first reason is the many sources of loss on the link, while the other reason is that a perfect receive antenna does not exist. The link budget on the downlink can be summarized in the form an equation for the carrier-to-noise-ratio (C/N_o) of the received signal

$$\frac{C}{N_o} = EIRP + \frac{G_R}{T} - Losses \quad (2.46)$$

where the ratio G_R/T is the receive antenna gain to noise temperature ratio for the receive antenna in dB/K. It is a standard measure of antenna performance. The sources of loss on a downlink can vary widely from system to system depending on a myriad of factors. As mentioned earlier, the highest source of loss is the free space loss (FSL), which was discussed in section 2.3 along with a other sources of loss that have also been examined. Some other sources common to all links include:

- Directive (or pointing loss) loss, which can occur due to the receiving antenna not being positioned to receive the satellite beacon in the direction of maximum power.
- Loss due to polarization mismatch between incoming beacon and receive antenna.
- Device and cable losses, arising from transmission lines, splitters, connectors and other appendages attached to the receive antenna.

2.6.3 Sun Outage on Satellite Links

In a calendar year, the days of the March Equinox and the September Equinox are the days on which the sun passes closest to the earth. On these days, the apparent path of the sun can take it directly behind geostationary satellites. Radiation from the sun, which includes microwave radiations similar to that used by the satellites but of higher energy, blocks out satellites communication channels for several minutes over a few days around the equinox. This phenomenon is known as a “sun outage”. The volume of noise introduced into the earth-satellite channel prevents the earth station from receiving any appreciable intelligent content [78].

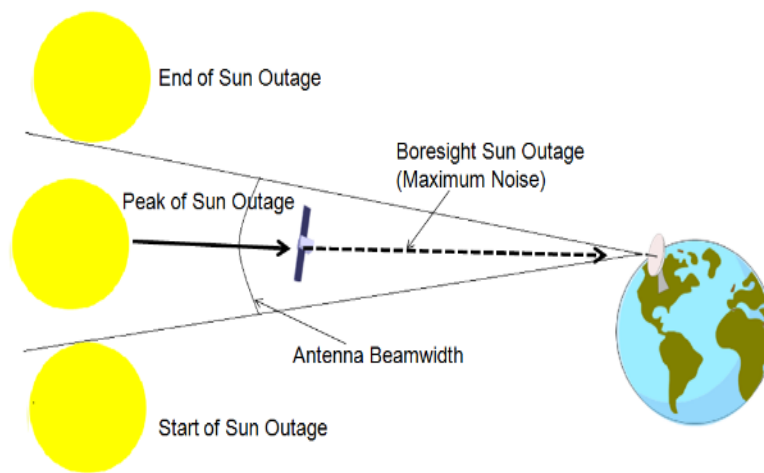


Figure 2-9: Dynamics of sun outage [79]

The brief period when the sun is directly behind the satellite is the point of maximum noise, referred to as the Boresight Sun Outage (figure 2.9), but the outage lasts as long as the sun lies within the beamwidth of the receive antenna. The ability to calculate and predict this event is crucial to preventing a total disruption of services that depend on the link.

2.7 Chapter Summary

In this chapter, some basic theoretical framework was laid for slant path rain attenuation studies. The behaviour of electromagnetic phenomena and how radio communication exploits it is presented. Common sources of loss of power content in radio waves are also discussed. The structure of rainfall and its behaviour on interaction with radio waves is also mentioned. The chapter outlines a few foundational rain attenuation models that form a basis for comparison and validation of the approach used for modelling it in this thesis. Lastly, a few basic ideas of satellite communication are discussed.

CHAPTER 3: MODELLING OF MEASURED ATTENUATION AT Ku BAND IN SUBTROPICAL RAIN

3.1 Introduction

This chapter reports the results of measurements carried out in order to draw empirical conclusions regarding the impairment caused by liquid precipitation on earth-satellite microwave links in subtropical climates. While such results may not be exhaustive due to limitations in time and resources, they are intended to form a basis for mathematical modelling and prediction which can then be applied exhaustively.

The measurement of rain attenuation is a complex process requiring a synchronized quantitative parameterization of several non-deterministic events and processes. At least two datasets are necessary for an elaborate measurement of rain attenuation. One is the rain rate data at the location, which is a purely stochastic quantity and the other is the Received Signal Level (RSL) on a practical link. Earlier work by [5] produced a measurement-based model of rain attenuation on a 19.5 GHz terrestrial link at the same location using rain gauge data and RSL measurements on their link in Durban, South Africa (29.86°S, 31.02° E). The present study looks at attenuation on a slant path link at the same location utilizing disdrometer measurements and Spectrum analyser logs of RSL levels.

Particulars of the two co-located measurement systems are first outlined. This is followed by a discussion of the results and analysis of the rain rate data captured. The actual attenuation measurements are then discussed under two separate headings. Attenuation measured in clear air is briefly discussed first and parameterized. This is followed by a more detailed outline and modelling of attenuation measured under rain conditions. A statistical validation of the proposed model is then presented, followed by a brief discussion of extreme rain attenuation conditions that lead to total signal squelching.

3.2 Measurement System Description

For a number of reasons, a reliable theoretical prediction method remains the ultimate approach to rain attenuation when planning the deployment of communication services. First of all, the cost of carrying out measurement campaigns can be prohibitive. Secondly, the range of measurement physically possible is limited in terms of link frequency, propagation path length, elevation angle, polarization type, modulation scheme and a number of other link parameters. A theoretical method will quite easily simulate a wide range of these parameters at little extra cost. A measurement-based model also needs to be location-specific in order to meet the requirement of future planning in that location or locations with similar rainfall patterns and climate. It is however important that any theoretical approach adopted has its basis on the results and models of extensive, painstaking and accurate measurement. Achieving the goal of creating a basis for theoretical prediction over a wide range of conditions must therefore be

the motivating factor and the express aim of a measurement campaign. A schematic of the entire measurement system is depicted in the Figure 3-1.

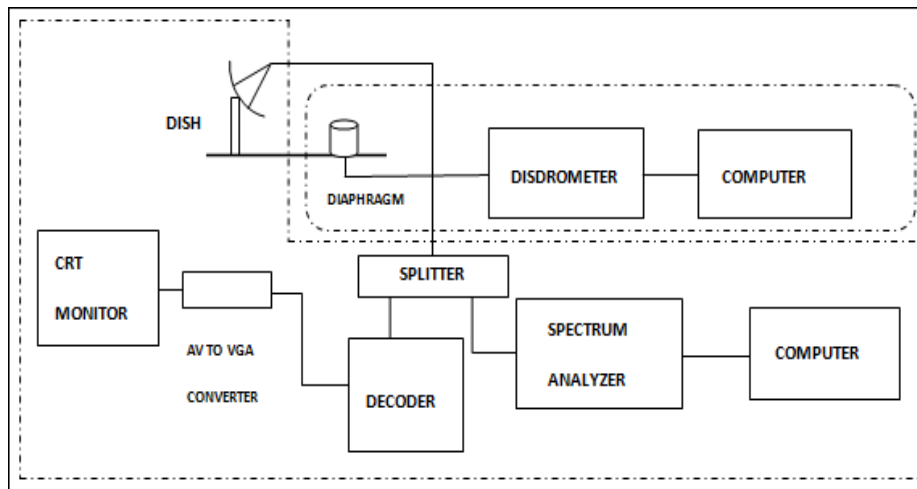


Figure 3-1: Schematic of the co-located dual measurement system

The measurement system used for this work was set up in the University of KwaZulu-Natal Howard Campus, Durban, South Africa. The system is installed on the roof of the six-storey Electronic Engineering building, making it free of potential physical obstructions to reception. A ground receiver system for a Ku band satellite TV service and a rain rate capturing system are the essential parts of the measurement. Figure 3-1 depicts the system in a schematic form. The disdrometer's diaphragm is less than 4 m from the receive antenna. The co-location of both systems is of vital importance as it creates the possibility of matching specific rain events with specific attenuation events. All rain attenuation events on the link are assumedly attributable to the precipitation events captured by the disdrometer. The disdrometer is fed directly to a computer, which stores the data collected. As shown in Figure 3-1, the spectrum analyser is fed from the Low-Noise Block downconverter (LNB) of the receive antenna through a splitter and a computer, a decoder and a visual monitor connected to it. No audio device was connected. Photos of the actual experimental set-up are presented in Figure 3-2.



Figure 3-2: Outdoor and indoor components of the measuring equipment set-up. Disdrometer diaphragm is 3.8 m from the receive antenna

3.2.1 Rain Rate Measurement

The intensity of rain events on the ground is measured in terms of rain rate in mmh^{-1} . At a much higher cost, the same parameter can be measured with a radar system. Modern ground level measurement of rain rate is done mostly by Rain Gauges or by Disdrometer. In this work, a Jos-Waldvogel impact type disdrometer (model RD-80) was used to capture rain rate at a frequency of 0.5 Hz (one measurement every 30 seconds). Figure 3-3 is a schematic of the disdrometer circuitry. The equipment is capable of capturing rain rates with a higher precision ($\sim 0.0001 \text{ mmh}^{-1}$) and frequency than traditional weather stations and rain gauges. In an impact type disdrometer, the momentum of rain drops falling on a diaphragm induces a piezoelectric current [80].

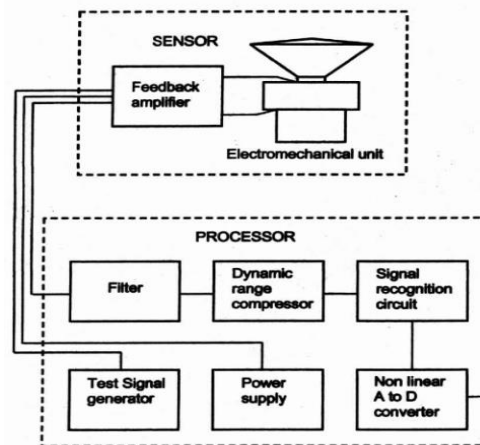


Figure 3-3: Schematic diagram of the Joss-Waldvogel impact disdrometer.

Through a series of microprocessors embedded in the processor stage (Figure 3-3), this current is converted into raindrop size, which is in direct proportion to drop momentum. Knowing the size of the raindrops and the frequency at which the diaphragm is impacted, a number of microphysical properties of rain such as rainfall rate, drop speed and drop shape can easily be deduced [81]. The Figures 3-4 and 3-5 are examples of the rain rate time series captured by the disdrometer.

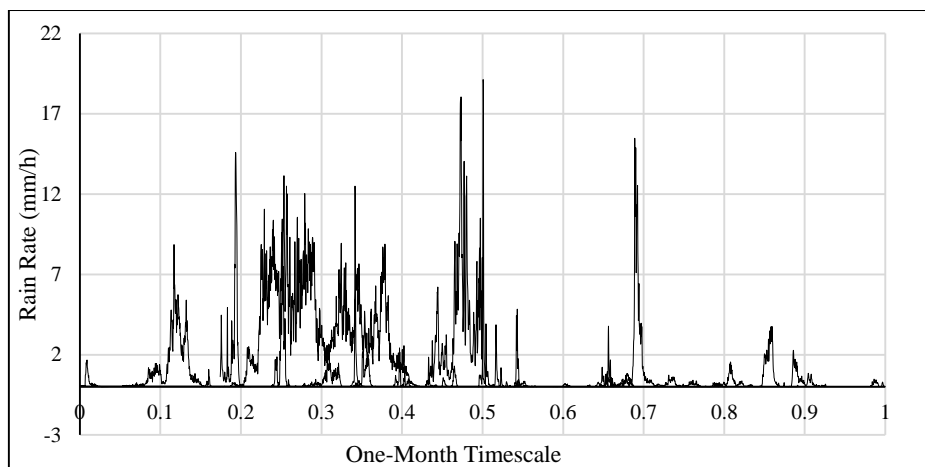


Figure 3-4: Time series of rain rate captured in the entire month of May, 2013

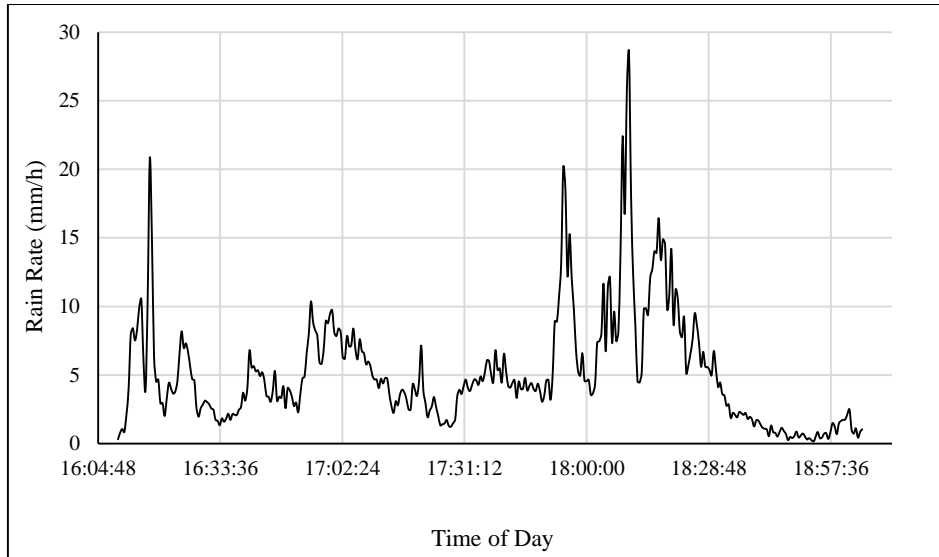


Figure 3-5: Time series of rain rate captured in a 3-hour period on 16th October 2014

3.2.2 The Satellite Beacon Receiver System

The satellite link profile is as depicted in the Figure 3-6. The satellite receiver is an offset parabolic antenna and a Low-Noise-Block downconverter (LNB) with frequency down-conversion to 950 -1950 MHz. The system receives High Definition Television (HDTV) via dedicated transponders on geostationary communication satellite Intelsat-20 (IS-20). The satellite is located at 68.5°E and has a true azimuth of 57.5° relative to Durban. The IS-20 satellite was launched in 2012. Its distance to the ground in Durban is 38,050 km and its elevation angle is 36.5° from the horizontal. The roof of the Electrical Engineering Building where the receiver is mounted is at an approximate height of 20.5 m from the ground but at a height of 176 m above sea level according to altimeter readings. The receiver dish diameter is 90 cm. From the satellite footprint contour, the recommended minimum dish size for optimal reception is 40 cm [82].

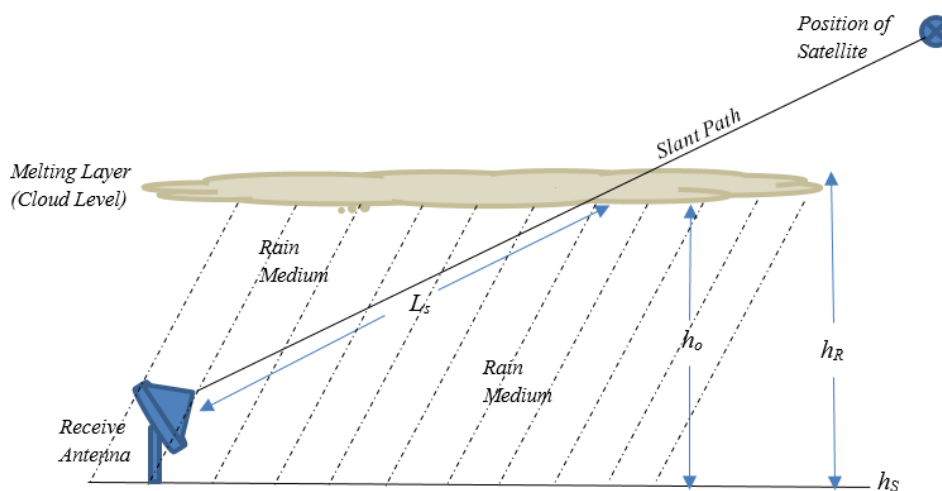


Figure 3-6: Basic physical profile of the satellite link.

In the figure 3-6, the height h_o is the height of the zero-degree isotherm in Durban. The position of the zero-degree isotherm varies throughout the year, hence a value that aggregates the annual average of this height can be read off for any location from a map provided by the ITU in the document [69]. The value for Durban is read as 4.6 km. The rain height h_R is then calculated as

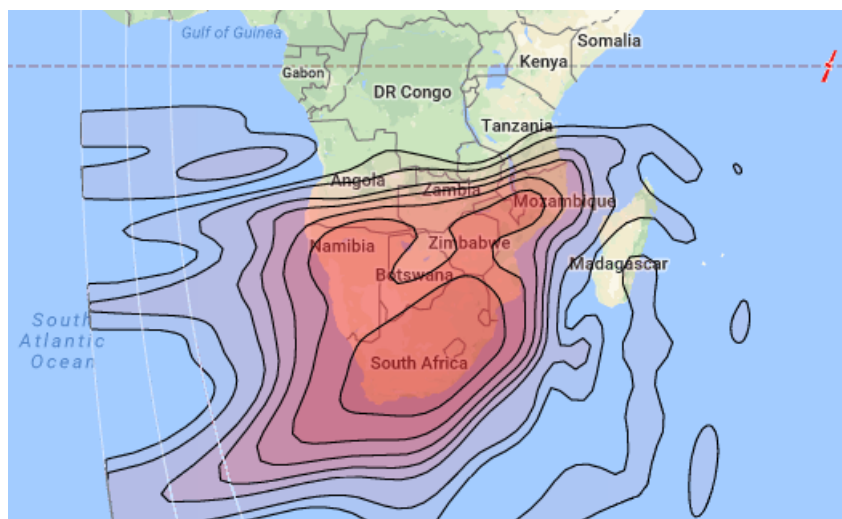


Figure 3-7: Footprint of the IS-20 communications satellite over southern Africa [82]

$$h_R = h_o + 0.36 \quad (\text{km}) \quad (3.1)$$

The slant path through the rain L_s is given by [8]

$$L_s = \frac{(h_R - h_s)}{\sin \theta} \quad (\text{km}) \quad (3.2)$$

where the height of receive antenna above sea level h_s is that at the roof of the said building stated earlier as 176 m or 0.176 km. A summary of the link parameters is presented in Table 3-1.

Table 3-1: Basic link parameters.

Parameter	Value
Elevation Angle (θ)	36.5°
Total distance to satellite	38,050 km
Longitudinal position of Satellite	68.5°E
Ground azimuth of satellite	57.5°
Height a.s.l. (h_s)	0.176 km
Rain Height (h_R)	4.96 km
Slant Path Length (L_s)	8.042 km
Beacon Central Frequency	12.6 GHz
Total bandwidth	40 MHz

The actual measurement of received signal level is achieved by a Rhodes and Schwarz FSH8 spectrum analyzer interfaced to the receiving via a splitter. A computer is connected to one end of the splitter for data storage. The other end of the splitter is connected to the signal decoder obtained from the satellite TV service vendor and then to a CRT display through which the visual quality of the signal can be monitored for distortions that occur during severe attenuation events. The satellite transmission to the ground is on vertical polarization and it is modulated in the 8-ary Phase Shift Keying (8-PSK) scheme with Forward Error Correction (FEC) code of 5/6 and symbol rate 30,000 bits/sec. The RSL measurement is carried out in form of sweeps conducted by the spectrum analyzer at a frequency of 1 sweep per minute. The sweep is done over one of the subcarrier bands identified on the transponder. It has a bandwidth of 40 MHz and a center frequency of 1.26 GHz after down conversion. Thus, the record captured contains the RSL values at individual frequencies across the band and the mean channel power, all in dBm. Measurement on this link is ongoing but the RSL results utilized for modeling in this thesis is based on measurements from all rain events from November 2013 to December 2014. An example of the RSL time series recorded by the spectrum analyzer is presented in the figure 3-8.

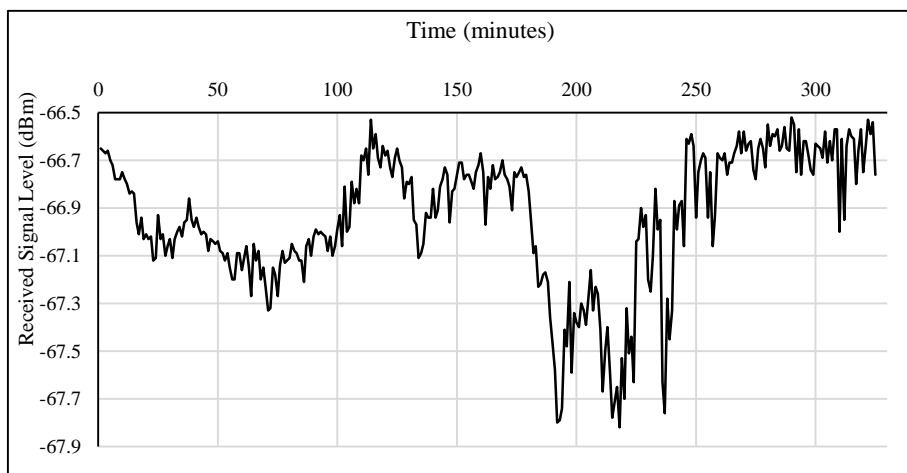


Figure 3-8: Time series of received signal level captured over a rainy period on 14th of November, 2013

An important advantage of the spectrum analyzer is that it features in-built channel filters such that, once given a set of suitable parameters during set up, it automatically gets rid of out-of-channel noises and rapid signal fluctuations due to atmospheric scintillation. This makes it unnecessary to pass the signal through a different filtration stage in order to ensure that the received signal only reflects fluctuations due to rain attenuation and other tropospheric sources. Scintillation effects are easily recognizable by the rapid rate at which they cause received signal to vary over time. Rain and clear air effects are markedly slower to reflect in received signal levels.

3.3 Link Budget Analysis

Table 3-2 summarizes all the gains and losses anticipated on the link and gives an estimated received power level as well as an estimated receiver sensitivity.

Table 3-2: Link Budget for Reception Footprint of Intelsat-20 Satellite over Durban ($\theta = 36.5^\circ$, $f = 12$ GHz)

STAGE	LINK	GAINS (dB)	LOSSES (dB)
Satellite-Antenna Downlink Transmission	EIRP (dBm)	85	
	Receive Antenna gain (dBi)	40	
	LNB gain	55	2
	Peripheral Cable Loss		3
	Free Space Loss		206
	Offset/Contour Loss		3
	Splitter Loss		7
	RF Attenuation through Spectrum Analyzer		20
	TOTAL	180	241
	Estimated Received Power Level (dBm)		≈ -61 dBm
Post-Antenna Processing	Noise Floor (at 40 MHz bandwidth)		-97 dBm
	5/6 8-ary PSK C/N Margin		25 dB
	LNB Noise Figure		0.3 dB
	Estimated Receiver Sensitivity (dBm)		≈ -71.7 dBm

The link budget only considers the satellite-earth transmission as the research interest is solely based on ground measurements over Durban. Firstly, the Effective Isotropic Radiated Power (EIRP) of the IS-20 satellite over Durban is determined from satellite footprint maps such as was retrieved from [82]. It is given as 55 dBW which is about 85 dBm. The received power level at the earth station can be estimated theoretically as:

$$P_{rx} = EIRP + G_{rx} + G_{LNB} - FSL - Losses \quad (3.3a)$$

where:

G_{rx} = Receive antenna gain

G_{LNB} = Low Noise Block (LNB) gain

FSL = Free Space Loss

The Free Space Loss (FSL) on the link which represents the highest loss factor, can be calculated from [11] and is given by:

$$FSL = 20\log_{10}(d) + 20\log_{10}(f) + 92.5 \quad (dB) \quad (3.3b)$$

where d is the total physical distance from the satellite to the ground which is 38,050 km and f is the carrier frequency in GHz which in this case is 12 GHz. From the equation (1b), we are able to estimate the value of FSL from the IS-20 satellite to the ground in Durban as 206 dB.

The top section of Table 3-2 summarizes a theoretically estimated analysis of link budget at the receive antenna location. The anticipated value of the RSL at any time during clear air at the location is obtained by summing up all the gains and losses. This sum yields a value of -61 dBm. In an investigation conducted for a line-of-sight terrestrial link in the 19.5 GHz band at the same location, [5] reported very similar link budget results for RSL levels in clear air. On the lower section of Table 3-2, post-receiver link budget figures are presented. The noise power is calculated over 40 MHz subcarrier bandwidth, with an assumed effective temperature of 290K. The noise power level is estimated using [83]

$$N_p = -174 + 10\log_{10}(BW)[dBm] \quad (3.4)$$

where BW refers to the subcarrier bandwidth which is 40 MHz as read from the spectrum analyzer. In addition, a Carrier-to-Noise (C/N) margin of 25 dB is assumed for this particular HDTV system under the stipulated 8-ary PSK modulation scheme. Theoretically therefore, the receiver sensitivity on this channel is approximately -71.7 dBm as presented in Table 3-1.

3.4 Statistical Analysis of measured rain rate data

As outlined in the previous section, several years of rain gauge and disdrometer data exists for Durban and has been used in various radio propagation research works. In the present work, measurement-based slant path rain attenuation modelling is approached using disdrometer data for 2013 and 2014. The rain events captured by the equipment were first analyzed based on a four-season cycle. Seasonal categorization given in [84] were adopted. Table 3-3 shows a seasonal and annual summary of processed rainfall rate measurements over this period at the site.

Table 3-3: Seasonal summary of rain rate data for 2013 and 2014

Season	Number of Samples	Maximum Rain Rate (mm/h)	Total Rainfall Time (Hours)	Percentage of Data (%)
Winter	9181	38.06	117.05	13.42
Spring	10392	23.69	100.52	15.18
Autumn	12866	32.9	181.1	18.79
Summer	36040	88.04	230.35	52.62

Annual analysis is also done based on the two-year period. Table 3-3 shows a seasonal and annual summary of processed rainfall rate measurements over this period at the site. On a seasonal scale, it is observed that more rainfall is experienced in the summer season than in other seasons. More than over 54% of rainfall in Durban occurs in the summer season, 18% in autumn and 15% in spring. The winter season with about 13% has the lowest amount of rainfall. This seasonal typically brings bouts of dry spell. As anticipated of a subtropical rain data, the greater majority of captured rain events fall into rainfall Stratiform structures, characterized by the predominance of low peak rain rate values for all seasons. However, we observe that convective rainfalls feature more prominently during summer and autumn seasons. This implies that these are the likely seasons to anticipate the worst earth-satellite link performance. The information presented in Table 3-4 illustrates the typicality of the Durban data of subtropical rain patterns.

Table 3-4: Peak Rain Rate Data for 2013 and 2014 by Rain Type

Season	Peak Rain Rate (mmh^{-1})			
<i>2013</i>	Drizzle (131 events)	Widespread (33 events)	Shower (46 events)	Thunderstorm (3 events)
Winter	4.994	9.888	21.982	-
Spring	4.923	9.903	32.894	-
Summer	4.991	9.961	36.083	88.042
<i>2014</i>	Drizzle (139 events)	Widespread (31 events)	Shower (28 events)	Thunderstorm (4 events)
Autumn	4.986	9.881	38.06	53.222
Winter	4.977	9.512	23.688	-
Spring	4.992	9.86	28.155	-
Summer	4.994	9.918	39.348	82.09

The classification of rain events as earlier discussed in section 2.4.6 was applied to the data. Stratiform events (drizzle and widespread) make up a large majority of the data. A few dozen shower events occurred in both years but there was only one thunderstorm event in 2013 and two in 2014. This pattern fits neither the typical temperate climate nor the typical tropical climate. The rain intensity pattern appears to fall somewhere in between, which in many ways defines a subtropical climate [85].

3.4.1 Rainfall Rate Exceedance over Durban

The randomness and variability of rainfall both in time and space dictates that it is to be handled in terms of probabilities when it becomes a vital parameter for any kind of engineering design. This holds true for communication link design. Typical values of rainfall availability are required for optimal link operation of both terrestrial (on the ground) and satellite systems (in the geostationary orbit). Therefore, it is necessary to ascertain these availabilities as obtained using seasonal and annual datasets in Durban.

Rainfall availability and rainfall exceedance are complimentary popular statistical tools applied in understanding local distribution of rainfall rates in radio links [2]. Even though the ITU-R P.837-7 document [86] provides a map off which $R_{0.01}$, the rain rate exceeded at 0.01% of the time can be read off for most locations on the globe, $R_{0.01}$ values obtained from measured data is often more valuable for system design. Thus, to compute rainfall exceedance at the location, rain rate values captured over the entire period was binned using a class rank of 1 mm/h. The probability of exceedance of rainfall rate is then computed as [87], [88],

$$Exceedance = \frac{\sum_i F_i \times 0.5}{N_D \times 24 \times 60} \times 100 \quad [\%] \quad (3.5)$$

where $\sum_i F_i$ is the cumulative frequency corresponding to the binned rain rate classes and N_D is the number of days for which measurements were undertaken.

The 30-second rain data was first converted to 1-minute integration time using the conversion relationship established by [49] as

$$R_\tau = u(R_T)^v \quad (3.6)$$

where τ is the required integration time, T the known integration time and u and v are power law regression coefficients. Using rain gauge and disdrometer data collected in Durban, Ahuna et al (2016) in [59] obtained values of $u = 1.004$ and $v = 1.0051$ fitted to data from Durban.

Figures 3-9 to 3-11 illustrate the annual and seasonal rain rate exceedance statistics over the period covered by the measured received signal level data. These graphs show that the summer and autumn seasons have the highest values of rainfall exceedance. On the other hand, the seasons of winter and spring have the lowest exceedance profile due to the inevitable dry spells experienced during these seasons.

A summary of the average annual and seasonal rainfall rate exceedance values at 10%, 1%, 0.1% and 0.01% are presented in Table 3-5. $R_{0.01}$ value for the entire period of measurement covered in this work is 69 mm/h. For the individual years, $R_{0.01}$ is 70 mm/h for 2013 and 67 mm/h for 2014. The year 2013 witnessed significantly more rainfall than 2014 in Southern Africa in general. Many parts of the region registered severe droughts in 2014. Comprehensive analysis of disdrometer data for the years 2009 and

2010 at the same location are reported by [4, 55]. Their results show good agreement with the present work considering the fact that the years covered by the present work had considerably less rainfall.

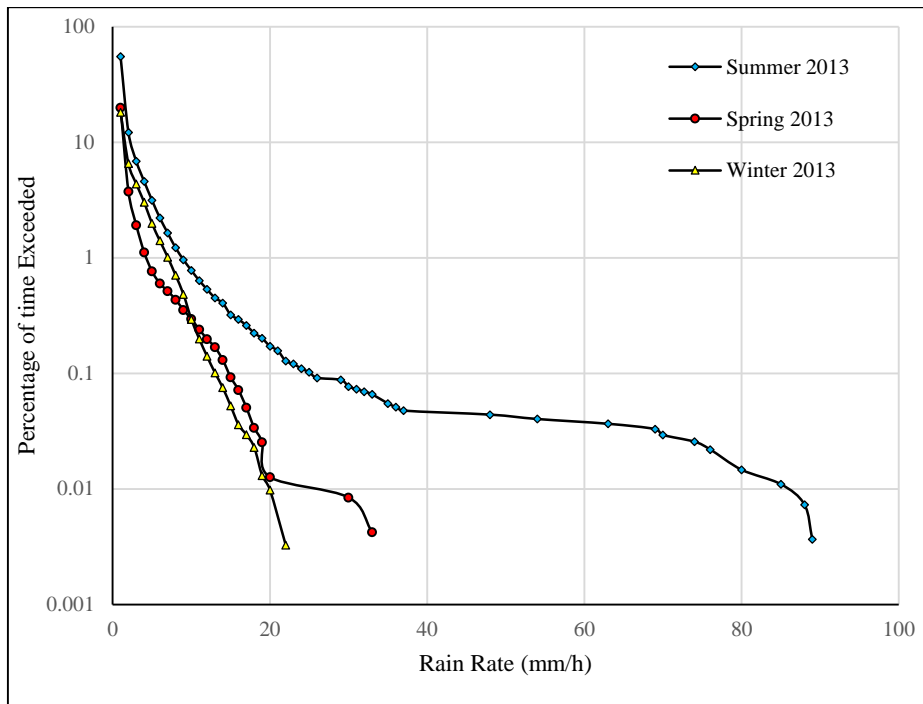


Figure 3-9: Seasonal Rain Rate Exceedance in Durban for 2013

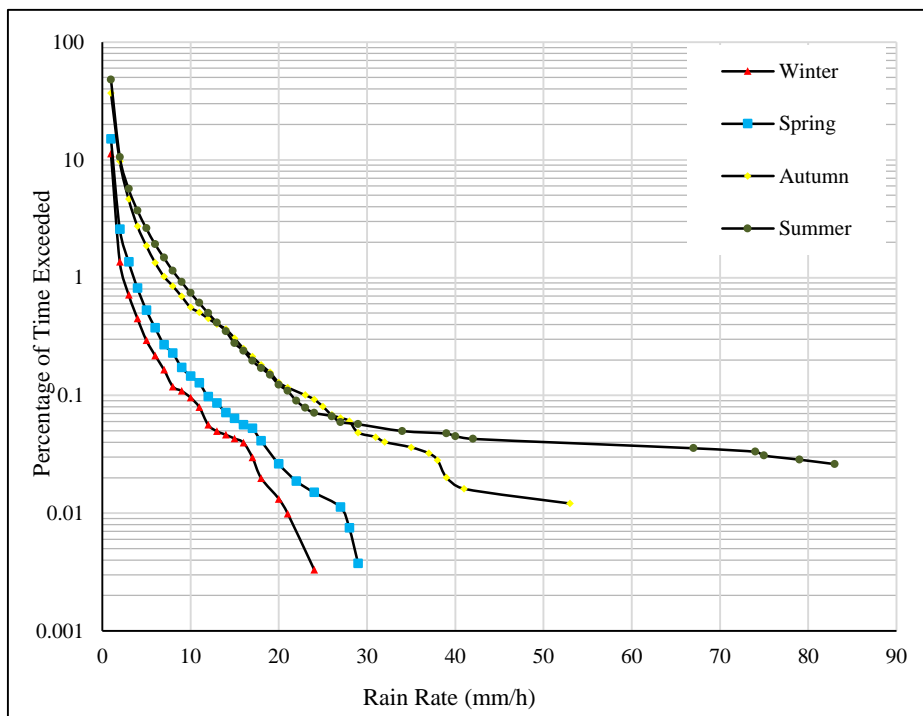


Figure 3-10: Seasonal and Rain Rate Exceedance in Durban for 2014

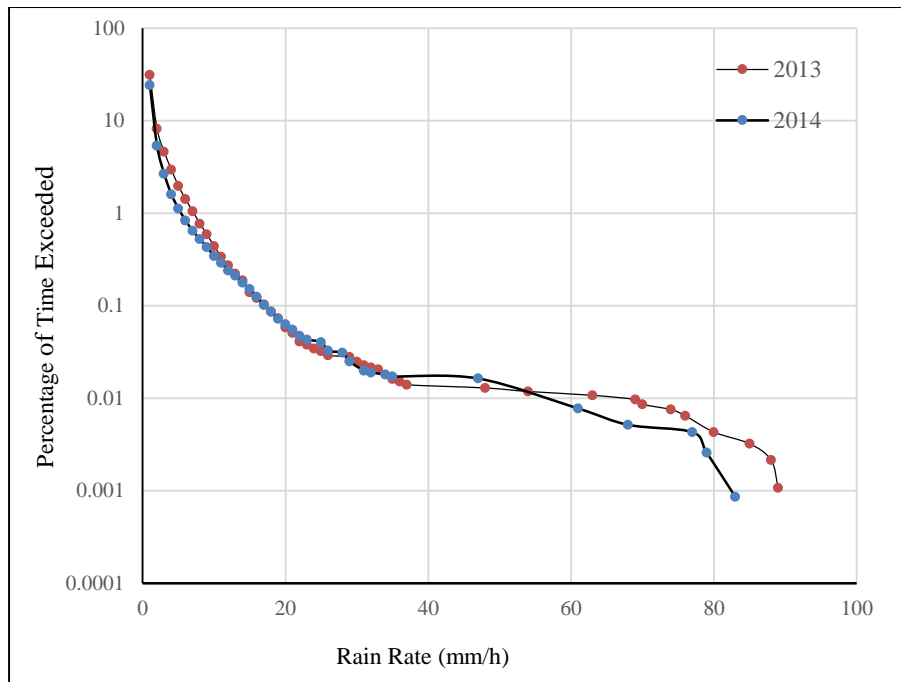


Figure 3-11: Annual and Rain Rate Exceedance in Durban for 2013 and 2014

Table 3-5: Average Seasonal and Annual Rain Rate Exceedance Statistics in Durban

SEASONS	RAINFALL RATE EXCEEDED (mm/h)			
	10%	1%	0.1%	0.01%
Summer	2.16	8.62	21.4	87
Autumn	1.9	7.17	23	54
Winter	1.06	2.39	9.5	21
Spring	1.22	3.6	11.7	27.2
Annual	1.6	5.2	17	69

3.5 Modelling of Clear Air Attenuation from Measured RSL

Clear-air condition is the general term used to describe periods of zero precipitation. While rain attenuation is the primary focus of the work, the variations recorded in RSL levels during clear air is a significant parameter to examine. The theoretical sources and models of clear air attenuation are explored in chapter two. Signal propagation through clear air in satellite systems is subject to a wide array of random spatial and temporal variations that directly affect the received signal on any wireless communication link. The variations under clear air are clearly secondary when compared to system performance in rainfall. But they require a separate analysis as they also impact the quality of reception on the ground. Clear air reception is also of importance because it serves as a reference level for quantifying the attenuation level under rain condition. The true level of rain attenuation is reckoned as the difference between the received signal in clear air and that received during rainfall.

3.5.1 Results and modelling of measured RSL in Clear-Air

The received signal on the link under clear air are obtained from the Spectrum Analyser sweeps recorded on the days and periods during which the disdrometer registers no precipitation (days of dry spell). As noted earlier, these sweeps were carried out every minute and the modelling done in the present work was done with the first 14 months' data from November 2013 to December 2014. This represents more than 600,000 values of received channel power.

In order to obtain a realistic capture of signal level in clear air, the RSL data in each month as well as the disdrometer data collected in the same month were closely examined. With the aim of obtaining the monthly variation pattern, a total of 160 to 200 hours of each month during which the disdrometer registered precipitation as being 0 mmh^{-1} were isolated. The RSL values recorded by the spectrum analyser during those same hours of the month were extracted. The equipment records RSL in dBm, which is a logarithmic scale. A direct averaging of logarithmic values will introduce significant error margins to the results. To avoid this, the values were converted to watts (W) and a simple arithmetic mean of the average for each month obtained. The result is then converted back into dBm. The conversions were done using the expressions

$$P_{dBm} = 10 \log_{10}(P_{mW}) \quad (3.7)$$

$$P_{mW} = 10^{\frac{P_{dBm}}{10}} \quad (3.8)$$

where P_{dBm} and P_{mW} are the power in dBm and power in mW respectively.

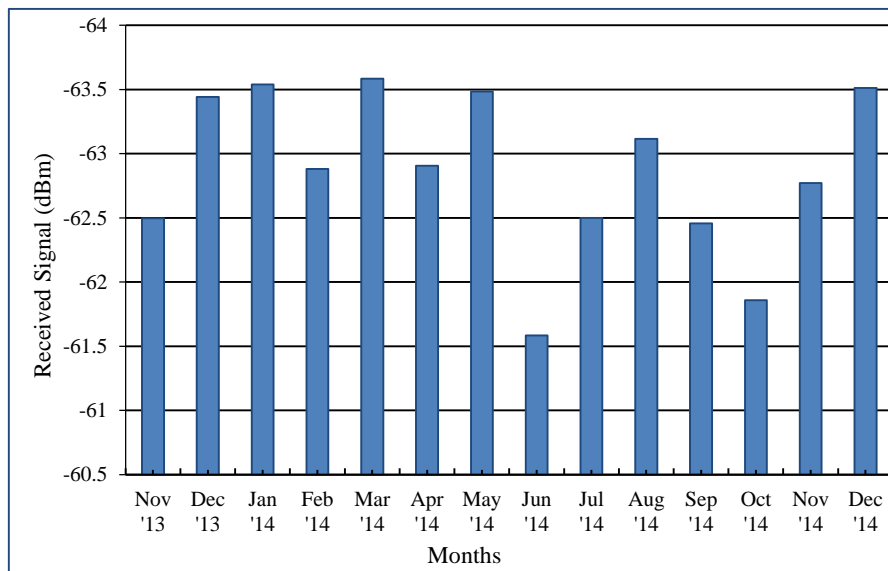


Figure 3-12: Variation of Monthly Averages of Clear Air Signal over Durban ($\theta = 36.5^\circ, f = 12 \text{ GHz}$)

The resulting analysis shows that the average clear-air received signal varied between -63 dBm and -62 dBm during each month. Fig. 3-12 shows that the lowest average monthly RSL levels in clear air

occurred in the month of June 2014, which marks the peak of the winter season in Durban and typically coincides with long periods of cloudless sky and low humidity. Further observation shows that the received signal in clear air did not drop as low as -64 dBm level throughout the period of measurement. From the link budget analysis in Table 3-2, clear air reception is theoretically estimated to be around -61 dBm. This is adopted as the reference RSL value for clear air conditions in this work. Being a coastal city, clear air reception in Durban is highly affected by fog and lower stratus cloud cover. The 1 to 2 dB fluctuation in clear air RSL is therefore likely to be primarily attributable to variations in the atmospheric conditions arising from fluctuations in temperature, relative humidity and atmospheric pressure through the seasons. Losses due to these three factors have the most significant influence on excess atmospheric loss [89]. A summary of the average monthly values of these parameters for the period of measurement is presented in Table 3-6.

The mean change in the *RSL* level or excess attenuation, ΔRSL_{clear} due to average monthly fluctuation in clear air values is given by:

$$\Delta RSL_{clear} = RSL_{ref} - RSL_{monthly} \quad (dB) \quad (3.9)$$

where RSL_{ref} and $RSL_{monthly}$ are reference RSL and average monthly RSL respectively.

Table 3-6: Monthly Average of RSL in clear air and Atmospheric Parameters over Durban

MONTH	Average RSL(dBm)	PRESSURE (hPa)	TEMP (K)	RELATIVE HUMIDITY	ΔRSL_{clear}
Nov 2013	-62.497	1014	294	79	1.497
Dec 2013	-63.442	1016	295	81	2.442
Jan 2014	-63.54	1013	297	79	2.54
Feb 2014	-62.88	1013	297	78	1.88
Mar 2014	-63.585	1014	296	80	2.585
Apr 2014	-62.907	1019	294	75	1.907
May 2014	-63.485	1018	292	77	2.485
Jun 2014	-61.585	1019	289	68	0.585
Jul 2014	-62.5	1022	288	69	1.5
Aug 2014	-63.115	1020	291	74	2.115
Sep 2014	-62.457	1019	292	74	1.457
Oct 2014	-61.858	1019	292	74	0.858
Nov 2014	-62.771	1017	294	75	1.771
Dec 2014	-63.512	1014	296	77	2.512

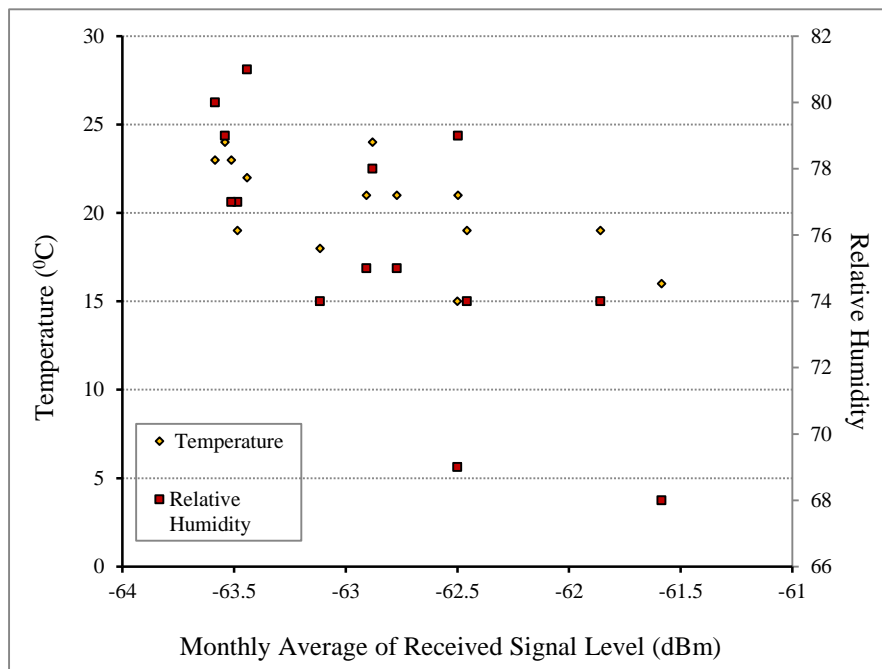
The clear air RSL data can be utilized to develop a model for predicting the average monthly change in clear air RSL (ΔRSL_{clear}). Assuming other clear air effects to be negligible, we apply the method of

multiple regression analysis to obtain an empirical relationship that can be employed to predict ΔRSL_{clear} as a function of the average monthly values of atmospheric temperature, T_{atm} in Kelvin, pressure P_{atm} , in HectoPascals and relative humidity H_{atm} for this location and during these months. In multiple linear regression, we model the relationship between one dependent variable and two or more other independent variables by fitting a linear equation to the known data of all the variables. The proposed relationship is the a zero-intercept linear equation:

$$\Delta RSL_{clear} = \eta P_{atm} + \beta T_{atm} + \sigma H_{atm} [dB] \quad (3.10)$$

where η , β and σ are regression coefficients obtained from the multiple regression from the clear air dataset in Table 3-6. These coefficients are given as -0.00343, -0.01481 and 0.1281 respectively as obtained from clear air atmospheric conditions over Durban. A close examination of the scatter plots presented in Figures 3-13 and 3-14 show that clear air RSL falls with increasing atmospheric temperature and relative humidity while it rises with increasing atmospheric pressure.

From equation 3.7 and the estimated values of σ , β and η , the average drop in the value of clear air RSL relative to the reference value obtained from link budget can be obtained for any particular month by plugging in the average monthly figures of temperature, pressure and humidity.



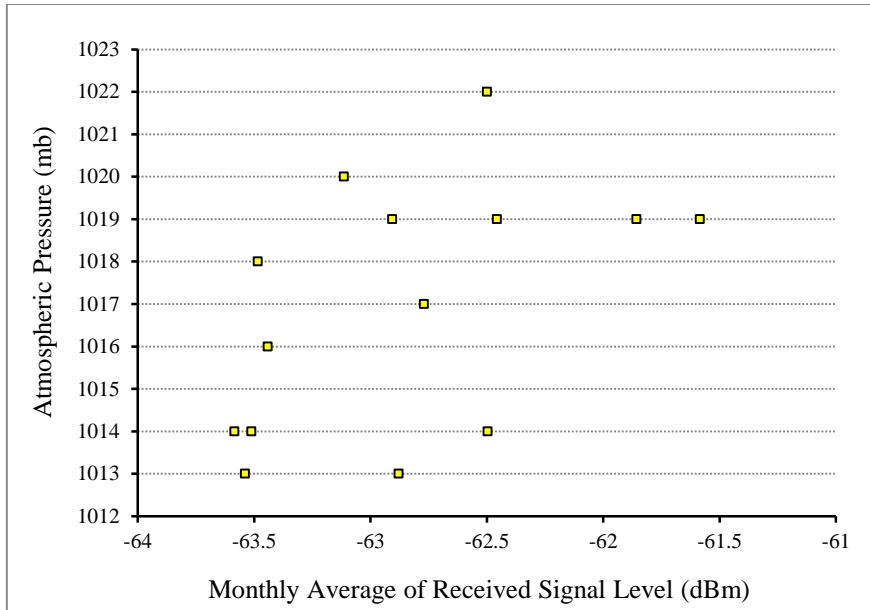


Figure 3-14: Variation of monthly averages of atmospheric pressure with average monthly RSL in clear air.

3.6 Modelling of Measured Rain Attenuation

3.6.1 Correlation of Rainfall Spikes with RSL Values

Having real time data for RSL and rain rate that were collected from the same location presents several advantages for modelling rain attenuation. Importantly, it creates a scenario in which all significant rain attenuation occurrences can be matched in the time domain to the specific rain spikes recorded at the same time at the location. This matching can be carried out by a number of different approaches. Since the direct dependence of rain rate to attenuation is well established [65, 66], it is often safe to assume that in a rain event, the highest level of attenuation dip is directly matched to the highest rain spike in the event. Thereafter, the remaining parts of the rain events are identified from the minimum attenuation point by applying event duration statistics from the rain rate data. The accuracy of this method depends on correctly locating the maximum peaks in the rain event no matter the overall pattern of the precipitation-attenuation distribution.

In this work, a rigorous comparison of the time series of both measurements obtained for the earth-satellite RSL and the rain rate measurement system was undertaken on an event-by-event basis in order to correlate their patterns in the time domain. This process was carried out for 79 individual events that occurred at the location between November 2013 and December 2014. The pattern of attenuation relative to precipitation is clearly observed in these plots and are distinguishable by the rain peaks and attenuation dips in the plots. Both the rain peaks and the corresponding attenuation troughs appear in groups. Within each rain event, the groups of rain peaks bear a remarkable similarity in shape and in number to the groups of troughs occurring in the RSL time series recorded at the same time. Specific rain spikes need to be assigned to specific RSL values to obtain the actual path attenuation. In order to

do this, the groups of rain spikes were assigned to the groups of RSL troughs. The peak values of rain in each group is matched to the lowest values of RSL in the counterpart group. Depending on the density of the peaks and troughs and the clarity of the patterns, the number of points extracted from each group for the matching process can be as few as two or as much as ten. Figures 3-15 to 3-18 illustrate a few examples of how the groups of rain spikes were matched with the attenuation troughs.

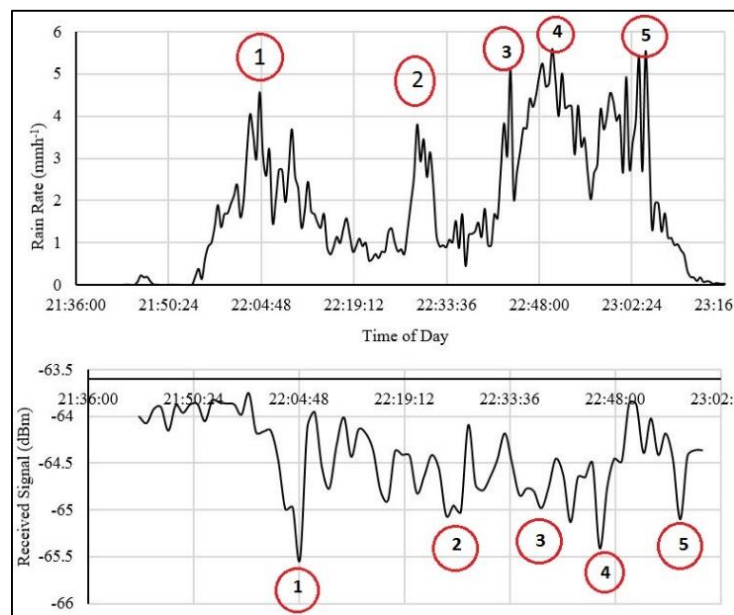


Figure 3-15: Assignment of rain peaks to RSL troughs for a drizzle event on 04/04/2014.

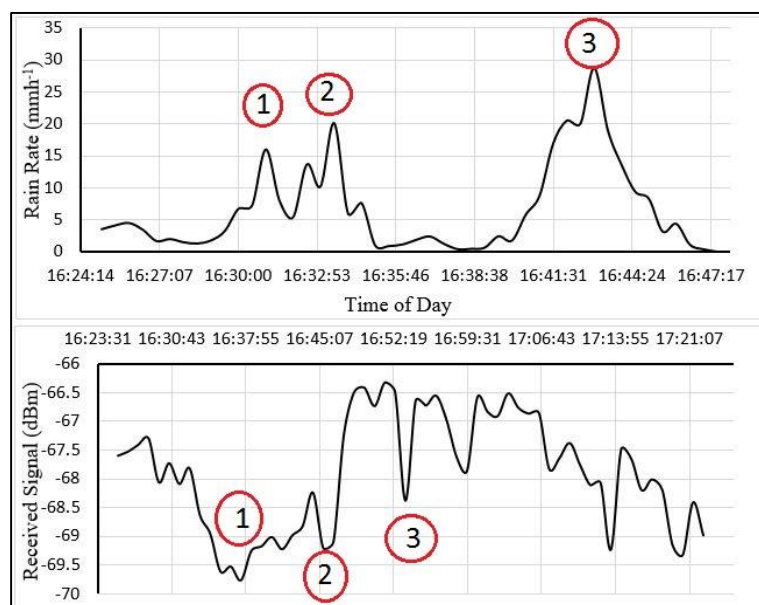


Figure 3-16: Assignment of rain peaks to RSL troughs for a shower event on 20/11/2013

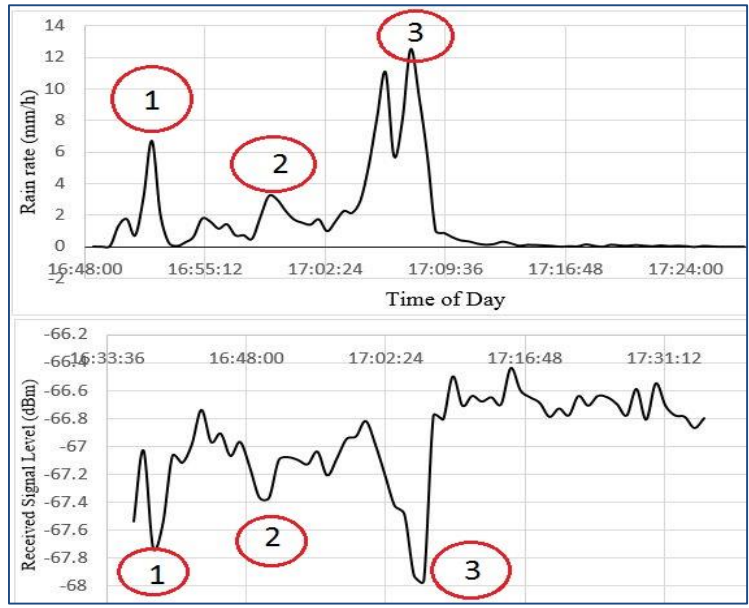


Figure 3-17: Assignment of rain peaks to RSL troughs for a widespread event on 15/12/2014

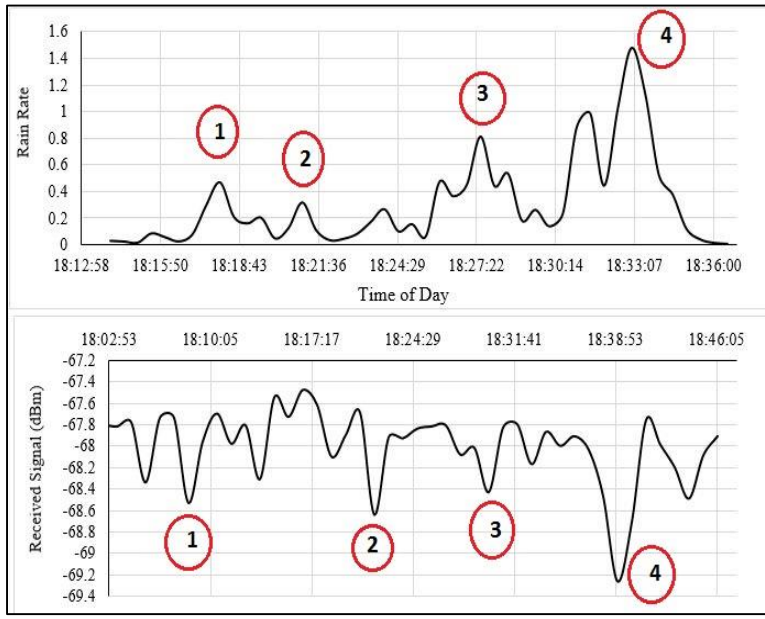


Figure 3-18: Assignment of rain peaks to RSL troughs for a drizzle event on 12/06/1013

In many of these events, an appreciable shift in time exists between the two sets of data. This time difference is traditionally attributed to factors such as irregularities in path geometry, rain structure, drop velocity and other effects that are usually left without investigation. Some other likely implications of the time lapse are however more fully explored in chapter six of this work. The fact that the rain peaks are responsible for the attenuation troughs is not in doubt however because outside the two patterns along the time axis (both before and after), both time series remain flat until the next rain event, which might be up to a few days later or earlier. When the apparent time difference between the matching peak/trough pair is too large, the sequential order of the peaks and troughs is ignored and the peak that

occurs nearest to a trough is paired with it. The actual attenuation due to each rain spike matched is given by

$$A_{R(t)} = RSL(t) - RSL_{monthly} \quad (3.11)$$

where $A_{R(t)}$ is the attenuation due to the rain spike $R(t)$ recorded at a particular time t , $RSL(t)$ is the RSL value matched with rain spike $R(t)$ and $RSL_{monthly}$ is the average monthly RSL value obtained for that particular month as presented in the previous section. $RSL_{monthly}$ is used as the datum RSL for estimating rain attenuation because only the attenuation induced in the channel that results in dragging RSL value below that point can be attributed to liquid precipitation. The rest is due to clear air effects. It becomes especially important to reckon with the contribution of $RSL_{monthly}$ in the final point rain attenuation figure because at frequencies below 15 GHz, this parameter could account for as much as 40% of the attenuation measured at rain rates of 5 mm/h and lower [88].

3.6.2 Measured Earth-Space Attenuation Statistics

Rain attenuation measurements in dBm extracted from 79 events over 14 months using the approach described in section 3.6.1 was analysed on a monthly, seasonal and annual basis. Table 3-7 presents a summary of the entire point attenuation data. Clearly, the system suffered more severe impairment during the summer season, with attenuation peaking at 8.66 dB. It should be noted that while the peak value of received signal expected on the link is -61 dBm, the noise floor for the system is -71.7 dBm. This implies that only an attenuation margin of 10.7 dB is actually measurable by the system. The signal gets completely squelched as it approaches this maximum and the equipment is unable to capture any further signal degradation.

Table 3-7: Seasonal Attenuation Statistics over Durban

Season	Sample Population	Maximum Attenuation (dB)	Percentage of Data (%)
Autumn	1252	8.33	26.07
Winter	683	3.23	14.22
Spring	1058	6.28	22.03
Summer	1809	8.66	37.67

Figures 3-19 to 3-26 present a preliminary analysis of the results of the measurement in the form of monthly patterns for 8 of the 14 months. The scatter plots are obtained by selecting average values of measured attenuation from the wide range of values represented in the data obtained for each rain rate bin. The months of April (end of Autumn), October (early in summer) and November in 2014 represent the months during which the highest fade events occurred while June 2014 was the month with the least attenuation.

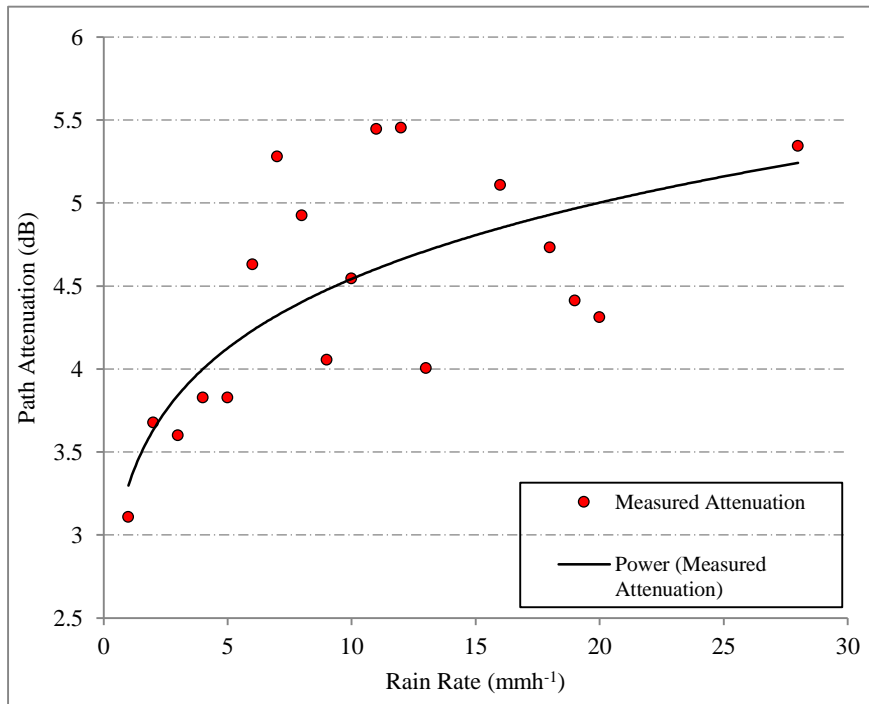


Figure 3-19: Variation of measured attenuation with rain rate in Nov 2013 ($\theta=36.5^\circ$, $f=12\text{ GHz}$)

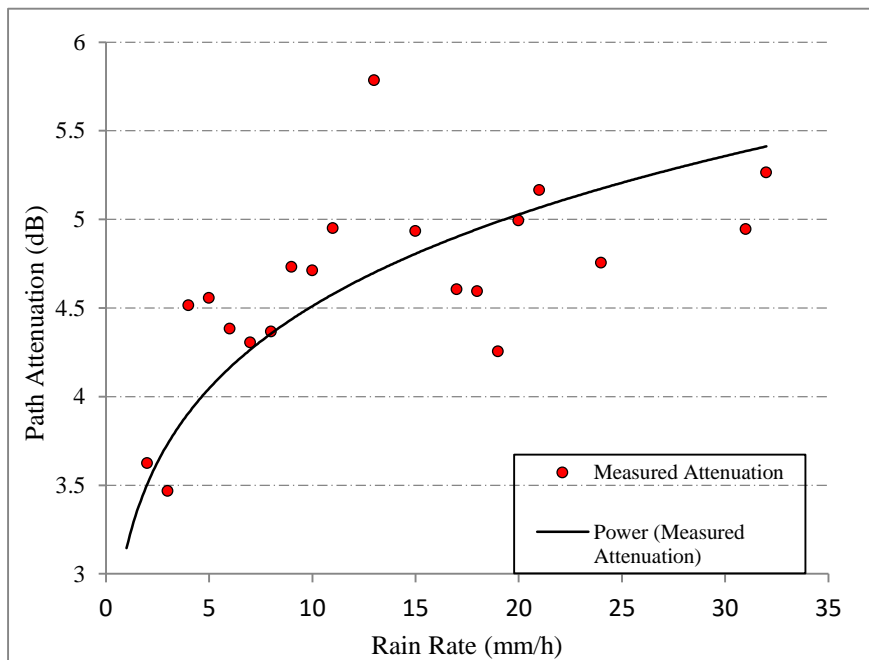


Figure 3-20: Variation of measured attenuation with rain rate in December 2013 ($\theta=36.5^\circ$, $f=12\text{ GHz}$)

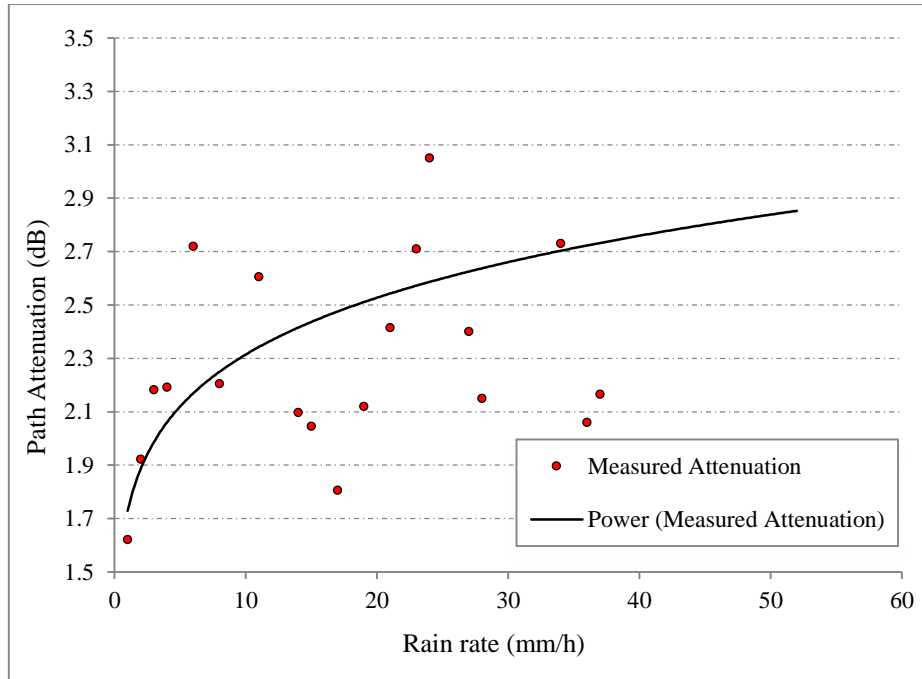


Figure 3-21: Variation of measured attenuation with rain rate in February 2014 ($\theta=36.5^\circ$, $f=12\text{ GHz}$)

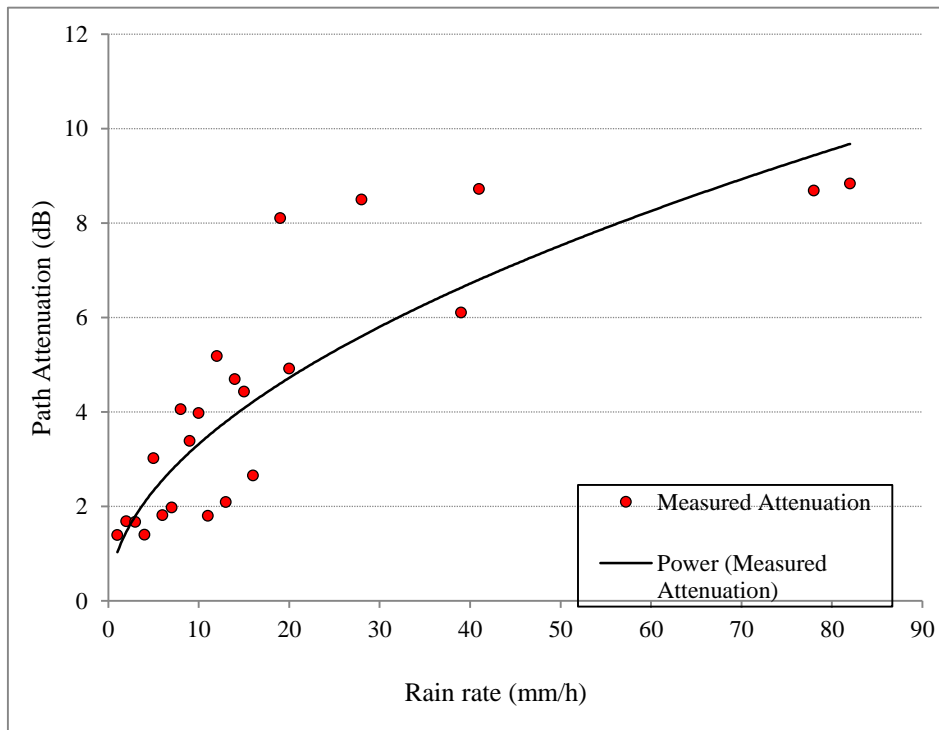


Figure 3-22: Variation of measured attenuation with rain rate in April 2014 ($\theta=36.5^\circ$, $f=12\text{ GHz}$)

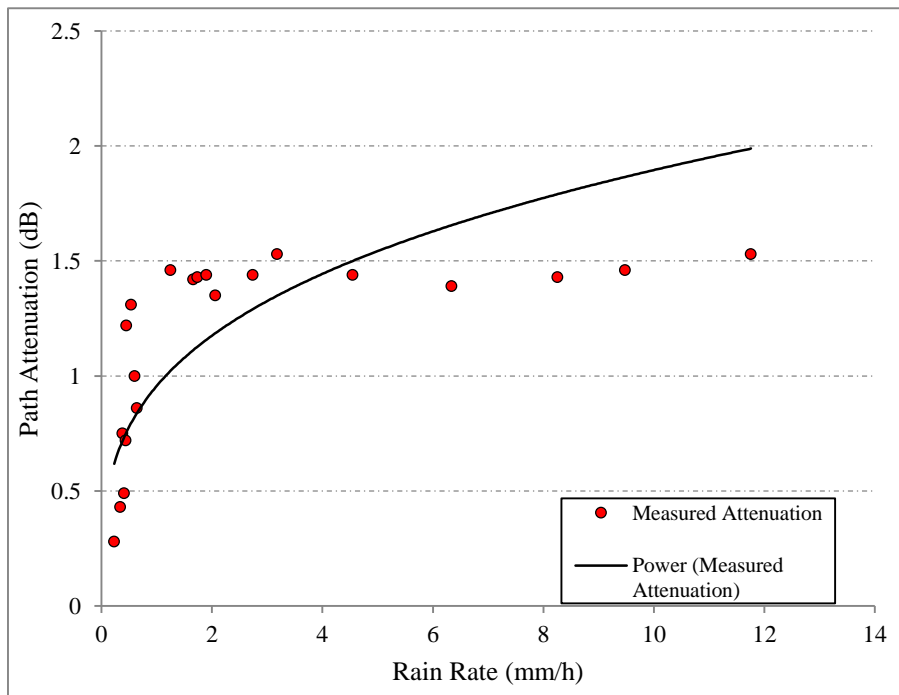


Figure 3-23: Variation of measured attenuation with rain rate in June 2014 ($\theta=36.5^\circ, f=12\text{ GHz}$)

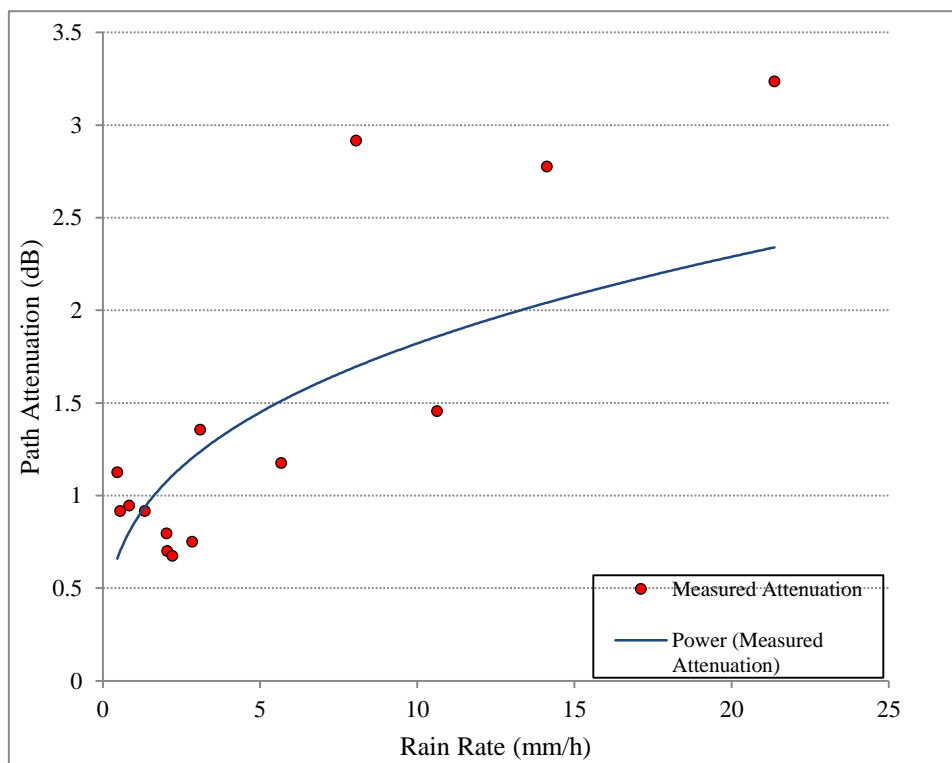


Figure 3-24: Variation of measured attenuation with rain rate in August 2014 ($\theta=36.5^\circ, f=12\text{ GHz}$)

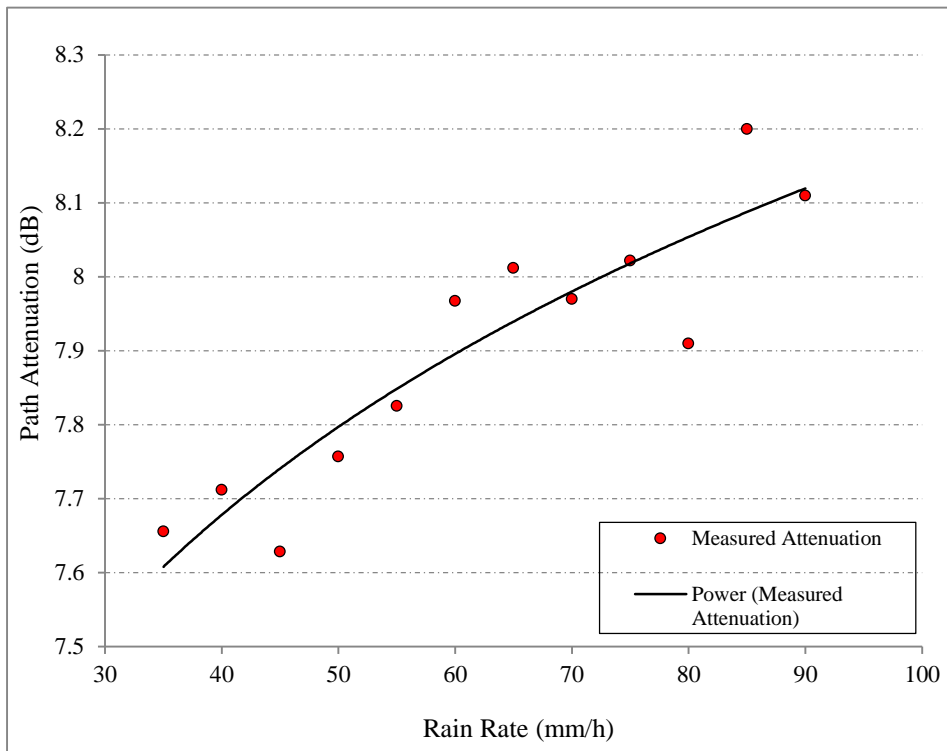


Figure 3-25: Variation of measured attenuation with rain rate in October 2014 ($\theta=36.5^\circ, f=12\text{ GHz}$).

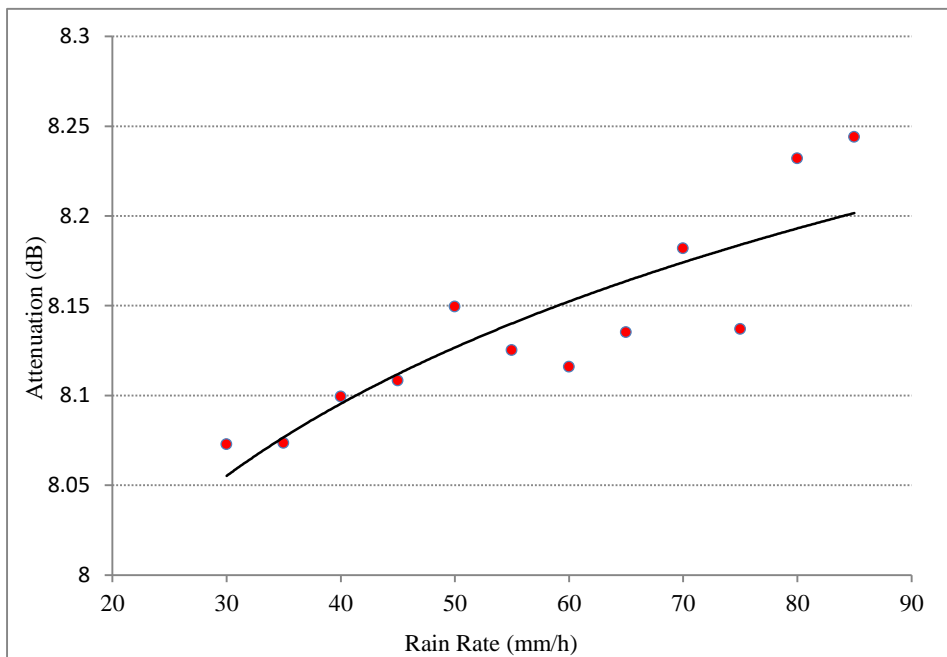


Figure 3-26: Variation of measured attenuation with rain rate in November 2014 ($\theta=36.5^\circ, f=12\text{ GHz}$).

3.6.3 Rain Attenuation Bounds over the Earth-Satellite Link

Theoretical models give a single attenuation figure for a given rain rate value but for measured fade, a range of attenuation values were recorded for each rain rate. In this work, the attenuation at each rain rate is classified by bounds. Figure 3-27 presents a scatter plot of all attenuation values recorded for each rain rate. The coinciding points of equal attenuation for each rain rate were represented by a single point. The Figure (3-27) illustrates the width of the range of attenuation values that were measured at each rain rate. The minimum attenuation margins recorded in each 1 mm/h-size bin are placed in the minimum bound, the highest values in a maximum bound, and an average bound created separately by taking a mean of the two.

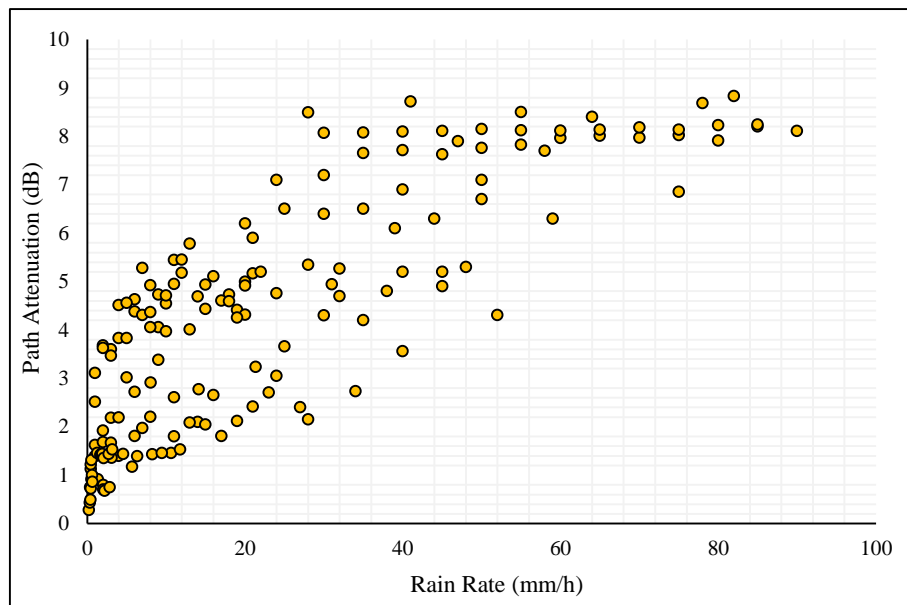


Figure 3-27: Scatter plot of all coincident attenuation points measured at each rain rate.

Aggregated values of attenuation experienced for the measurement period at various rain rates up to the maximum rain was mathematically modelled as a function of the rain rate. The relatively wide variation of the values of measured attenuation that is obtained for each 1 mmh^{-1} bin of rain rate was taken care of by developing a separate model for each bound. It has been established that path attenuation due to rain, A_p as a function of rain rate R obeys both logarithmic and power law relationships of the form [65]

$$A_p = aR^b [dB] \quad (3.12)$$

$$A_p = a + b \ln R \quad [dB] \quad (3.13)$$

where a and b are the regression coefficients. Taking inspiration from this early model, the point attenuation values were used as input into a computer algorithm to obtain both power law and logarithmic expressions that accurately model the attenuation measured on the link for each of the bounds earlier created. The governing expressions thus were obtained are presented in Table 3-8 below.

The Coefficient of Determination (R^2 values) for each model obtained was also computed and they are presented along with the expressions. These values serve as a first test of the actual fit of the model to the measured data. An R^2 of 0.8 for example indicates that the model will conform with exactness to the measured data 80% of the time. The lowest R^2 value for all the models is 0.8342, which is the value estimated for the logarithmic model of the maximum bound while the highest is 0.9111 for the power law model in the minimum bound. The accuracy offered by this range of R^2 values give an immediate indication that the models are likely to be useful tools for predicting rain attenuation on slant paths in Durban and for similar subtropical climates. Further validation of the models with other models was carried out and are presented in the following section.

Figure 3-28 presents minimum, average and maximum slant path rain attenuation curves in Durban, South Africa with its logarithmic models, while figure 3-29 shows the same data with the power law models. The irregularity seen in the scatter plot of actual measured attenuation is due to the wide spatial variation of rainfall which makes it impossible to obtain a regular rain attenuation pattern, hence the importance of empirical models. For most of the year, the attenuation increases steadily as a function of rain rate up to about 20 mmh^{-1} . Above this rain rate, the attenuation tends to level out irrespective of rain rate.

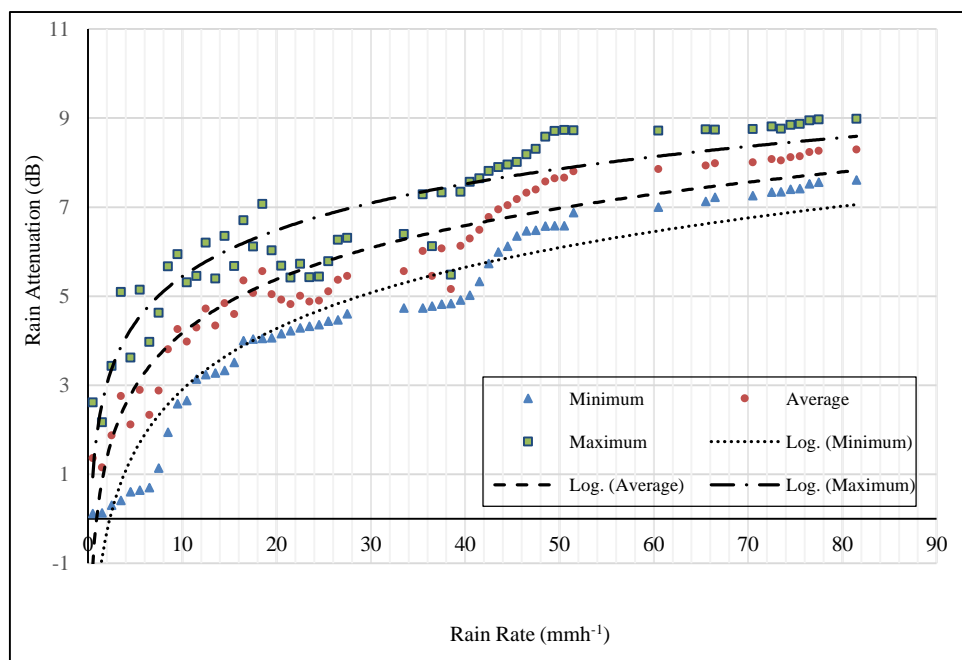


Figure 3-28: Logarithmic Models of Rain Attenuation Bounds model ($\theta = 36.5^\circ$, $f = 12 \text{ GHz}$)

Table 3-8: Logarithmic and Power Law Models of Slant Path Attenuation

Rain Attenuation Bounds	POWER-LAW MODEL		LOGARITHMIC MODEL	
	FUNCTION	R^2	FUNCTION	R^2
Maximum	$2.7567R^{0.2693}$	0.8662	$1.9841 + 1.5051\ln(R)$	0.8342
Average	$1.3387R^{0.5482}$	0.8999	$0.1601 + 1.7418\ln(R)$	0.9
Minimum	$0.2165R^{0.8811}$	0.9111	$-1.6643 + 1.9821\ln(R)$	0.9058

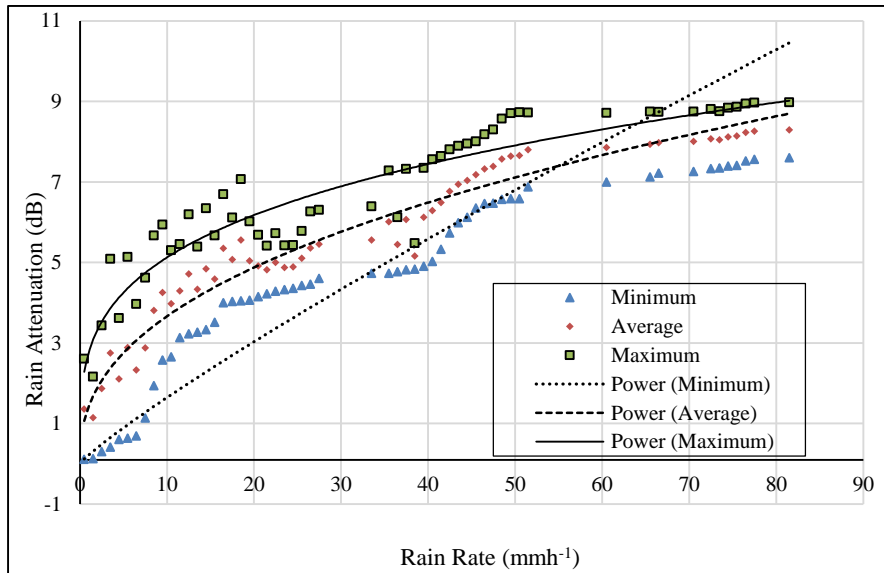


Figure 3-29: Comparison of measured Rain Attenuation with ITU-R model ($\theta = 36.5^\circ, f = 12 \text{ GHz}$)

3.6.4 Slant Path Rain Attenuation Exceedance Statistics

Geostationary satellites when launched into their orbital positions can have footprints that span several hundreds of kilometres. The nature and severity of tropospheric turbulence faced by the dedicated transponders on these satellites that arise as a direct result of the non-homogeneity of precipitation effects over the reception area is often too diverse to predict in a deterministic manner [2]. Depending on the severity of the local rain events, several pockets of impairment and even outage problems around the ground receiving area can occur. It is therefore traditional to handle the anticipated link impairments due to rain in probabilistic terms. Thus, earth-satellite links are designed such that they are required to experience as low a probability of outage over the year as possible, especially without the aid of fade self-aware fade mitigation feedback systems [90]. Precisely, they are designed for availability during 99.99% of the year. The attenuation that will likely occur during 0.01% of the year, $A_{0.01}$ is of extreme importance.

The measured total path attenuation due to rainfall that will be exceeded on the slant path link at 0.1%, 0.01% and 0.001% were estimated based on the seasonal and annual rain cycle in Durban as discussed in the chapter two. The rain attenuation exceedance curves obtained from these attenuation measurements during the stated measurement period is presented in Figure 3-30. The figure shows that the winter season is the season during which the satellite broadcast system will have the lowest amount

of rain impairment both in severity and in duration. In the other seasons, impairment levels are not only likely to be more severe but such levels are equally likely to last for higher percentages of time. Autumn and spring seasons tend to suffer more. This suggests that the winter season is the best season for satellite broadcasts in subtropical climate. At rainfall exceedance of 0.01%, attenuation values of 5.7, 8.0, 2.3 and 7.8 dB are estimated over the satellite link for summer, autumn, winter and spring seasons respectively. At 0.001%, estimates for these respective seasons are 6.1, 8.87, 3.15 and 8.24 dB.

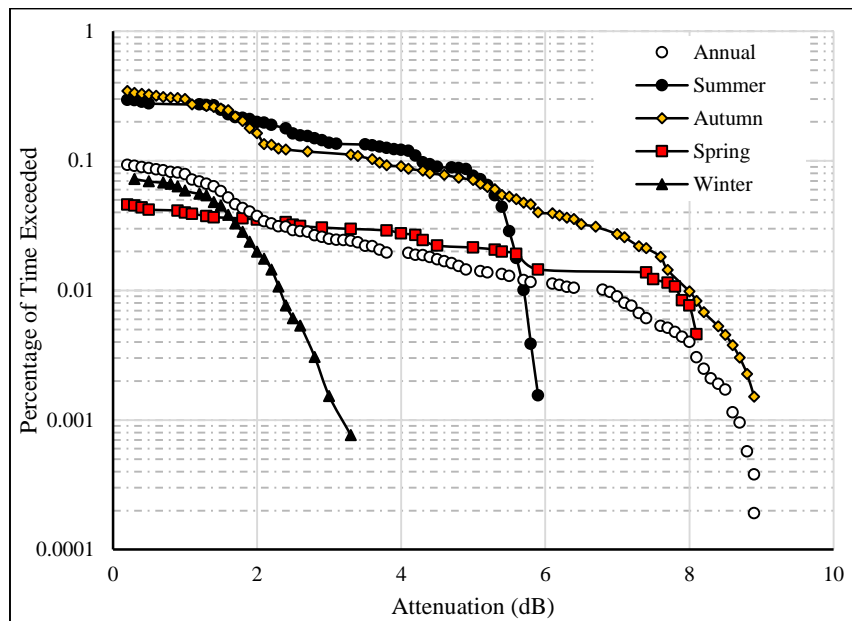


Figure 3-30: Seasonal and Annual Slant Path Attenuation Exceedance Probability in Rainfall over Durban, ($\theta = 36.5^\circ$, $f = 12 \text{ GHz}$).

A summary of the seasonal and annual rainfall exceedance is presented in Table 3-9. The annual rainfall exceedance curve is closest to that of the spring season, which implies that this season is responsible for the shape characteristics of the annual attenuation distribution in Durban.

Table 3-9: Seasonal Values of Path Attenuation Exceedance

Season	Rainfall Attenuation Exceeded (dB)		
	$A_{0.1}$	$A_{0.01}$	$A_{0.001}$
Summer	4.2	5.65	6.1
Autumn	3.6	8	8.87
Winter	0.3	2.3	3.15
Spring	0.2	7.8	8.24
Annual	0.2	6.3	8.9

3.6.5 Validation of the Proposed Measurement Model

To validate the earth-satellite rain attenuation measurement model for a wider applicability, the model was validated by comparison with four other previously existing models that have been widely applied for predicting slant path rain attenuation. The validation was carried out with a two-pronged approach. One is based on the ITU-R recommendation embedded in the document ITU-R P.311-16 [91] for the validation of measured attenuation with another prediction model. In the said recommendation, a model-validation parameter (or test variable) V_i is defined such that

$$V_i = \ln \left\{ \left(\frac{A_m}{A_p} \right) \left(\frac{A_m}{10} \right)^{0.2} \right\} \quad \text{for } A_m < 10 \text{ dB} \quad (3.14)$$

$$\text{and} \quad \ln \left(\frac{A_m}{A_p} \right) \quad \text{for } A_m \geq 10 \text{ dB} \quad (3.15)$$

where A_m is the measured attenuation and A_p is the attenuation predicted by a different model. A root-mean-square-error parameter is then obtained from the mean and standard deviation of V_i as

$$RMS(V_i) = \{Mean^2 + St. Dev^2\}^{1/2} \quad (3.16)$$

As with all RMSE-based error parameters, the smaller the values of V_i and $RMS(V_i)$ compared to the maximum expected values of the parameter of interest, the more favourably the model compares to the existing ones in terms of scientific reliability.

The second model validation parameter is the Chi-Square test. This is a common parameter for testing a proposed hypothesis. It estimates a parameter (the χ^2 value), which is given by [92]

$$\chi^2 = \sum \frac{(O_i - E_i)^2}{E_i} \quad (3.17)$$

where O_i is the observed value, which is in this case the measured value and E_i is the expected value, that is, the value obtained from the existing model. Chi-squared test is a statistical tool that allows the comparison of the results of an observation with that of what is expected by making enabling a decision to be made whether to accept or reject the Null Hypothesis. The Null Hypothesis essentially states that:

“There is no statistically significant difference between the observed and the expected value of a measured parameter”

We shall either accept this or reject it by comparing the value of χ^2 obtained to a “critical value” read off a Chi-Square distribution table for the exact conditions of the test we are performing. We accept the hypothesis if the chi-squared value falls within and below the critical value and we reject it if it is higher than the critical value. There are two basic conditions for a chi-squared test. One is termed the number

of degrees of freedom. This is given by $(N-1)$, where N is the number of observation points we are using for the hypothesis. The other condition is the confidence level. This defines a percentage for how certain we are that we are accepting the null hypothesis. This percentage coincides with $100(1-\alpha)$, where α is the area under the tail of the chi-square curve from which we are to read our critical value. For example, imposing a confidence level of 95% for our test will imply that we use the critical value that coincides with our number of degrees of freedom under $\alpha = 0.05$ column. Statistically, this means that we are 95% sure of our decision to either accept or reject the null hypothesis.

As noted earlier, the measurement system employed in this work has only a 10.7 dB margin of attenuation measurement possible since it has a noise floor of -71.7 dB and an estimated maximum received signal of -61 dB from link budget. For this reason, the test variable was calculated only up to the values of rain rate that yield an attenuation value of 11 dB in the prediction models. This is because attenuation values above this level lacks valid statistical correlates in the measured data. The prediction models were calculated as total path attenuation for a link of the same path length as the measurement link, since the measurement model is based on total path attenuation rather than specific attenuation. The comparison was done using the proposed power law models of measured data rather than the logarithmic models as both yield results that lack any significant statistical variation between them.

Details of the models adopted for the comparative validation have been explored in chapter two. The following is a brief outline of things to note about them and some reason(s) they were selected.

a). Olsen Model

The Olsen model (section 2.5.1) was the first successful power law relation between rain rate and path attenuation. It has been applied widely over a long period and diverse link types and once enjoyed the status of being the in-force ITU-recommended model for system planning. It employs frequency dependent regression coefficients.

b). Garcia-Lopez Model

The Garcia-Lopez model (section 2.5.4) improves on the basic power law model for slant paths by introducing new coefficients a , b , c and d in a more composite expression. The new coefficients were obtained by regression from long-term measured data but they are location-specific. While no values were specified for subtropical Africa in this model, the coefficients specified for Australia were adopted rather than the “global” values. This is because Australia approximates the rainfall pattern in South Africa better than any other region, having a large area with typical subtropical weather.

c). Crane Global Model

The Crane Global model (section 2.5.3) was developed specifically for estimating the path attenuation over links with path length ranging from a link-specific threshold up to 22.5 km. It has been applied widely for a diverse array of link types. It makes provision for predicting on both terrestrial and slant path links. It employs a sum of three exponential factors as a multiplier to improve on the basic power law expression. It also has the advantage of making use of the $R_{0.01}$ value for the year in question to estimate a few parameters peculiar to the model as well as being location specific. It provides a table for predicting the $R_{0.01}$ for various regions of the world. Durban falls in the region D3 on the Crane global scale and it recommends an $R_{0.01}$ of 63 mm/h for the region [31]. This is especially close to the value obtained from our disdrometer measurement for 2014 which is 69 mm/h. The latter value was used.

d). ITU-R Model

The in-force ITU-R model (section 2.5.5) was also used as one of the models for validating the measurement. This model introduces a parameter called the “effective path length” L_E . L_E is obtained after applying both vertical and horizontal correction factors to the path length L_S . The resulting length factor is then multiplied by the specific attenuation obtained by a well-known power law expression. This model is regarded as the current universal standard for modern link planning. Figure 3-31 shows the behaviour of the proposed model in comparison with the prediction models.

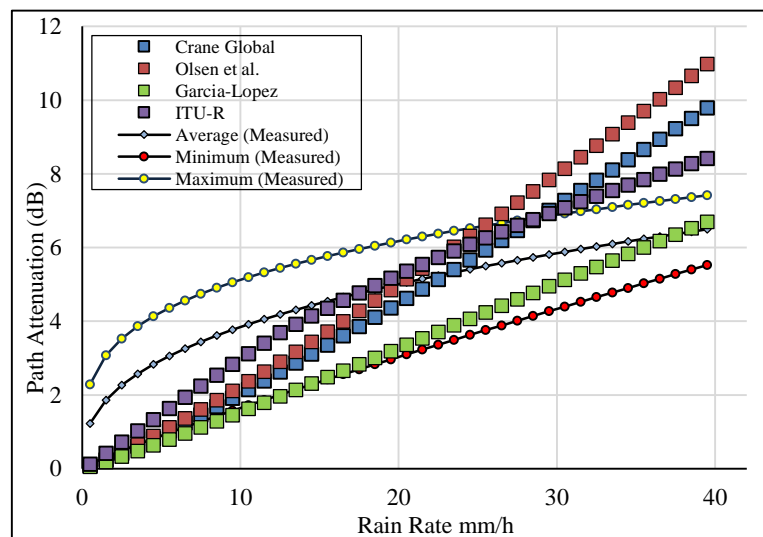


Figure 3-31: Performance of the bounded measurement-based models compared with existing models in the 11 dB path attenuation margin.

From zero to about 7.5 dB, the minimum and maximum bounds form an envelope within which the other models are contained while the average bound occupies an approximate median position between them. The best agreement is seen between the minimum bound and the Garcia-Lopez model. The other

three prediction models gradually slide into some overestimation at rain rates of about 30 mm/h and above. This pattern partly illustrates the peculiarity of slant path attenuation in subtropical rain.

Statistical validation of the measurement is more precisely illustrated by the values of RMS (V_i) and chi-square presented in Tables 3-10 and 3-11 respectively. Overall, the average RMS error seen in the measurement is 2.04, which represents an 18.5% average variation of the measured data from predicted data. The models conform best to the Garcia-Lopez, Olsen and the ITU-R models. This is probably because these models are strongly influenced by specifics of location and local rain patterns, which is equally the expected strong point of the measurement model. The worst performance is seen in the Crane model, especially in the maximum bound. This model being basically a function of frequency and path length, the peculiarities of location do not play a big role in its implementation. While the level of conformity of the measured data to known theoretical models represents a validation, the extent of non-conformity suggests non-reliability of the theoretical models for the particular link and rain pattern/climate.

Table 3-10: RMS Error values of measured attenuation bounds against some existing models

Prediction Model	RMSE(<i>Minimum Bound</i>)	RMSE(<i>Average Bound</i>)	RMSE(<i>Maximum Bound</i>)
Olsen	2.18	1.84	2.21
Garcia-Lopez	1.51	1.81	1.21
Crane Global	1.96	2.8	3.28
ITU-R	2.12	1.85	1.69

On the Chi-square scale, the test rejects the Crane Global model in all of the bounds of rain fade measured. This likely demonstrate the unsuitability of the Crane Global model for prediction in the Durban environment and similar environments and for similar links. The test registers a verdict of acceptance in all the other instances. Overall, the measurement results are validated as being in high conformance with theoretical predictions. The cases of hypothesis rejection are such that the margin of difference between the estimated Chi-square value and the critical value are not exactly outrageous.

Table 3-11: Chi-Square test results of measured attenuation against expected values from some existing models

Model	Minimum Bound		Average Bound		Maximum Bound	
	χ^2 Score	Critical Value	χ^2 Score	Critical Value	χ^2 Score	Critical Value
Olsen	24	77.981*	21	75.624*	19	76.778*
Garcia-Lopez	29	123.225*	22	89.931*	34	91.67*
Crane Global	86	77.981#	110	75.624#	117	77.778#
ITU-R	33	123.225*	26	123.225*	16	118.752*

Key to test result: * = Model accepted, # = Model rejected

3.7 Reception Outage at Slant Paths due to Rain Attenuation

A few rain events during the period of report of measurement resulted in high levels of attenuation on the link leading to total signal squelching. Typically, this occurs when the received signal drops down to and below -71 dBm. On such days, as shown in the synchronized time series of rain rate and received signal in Figures 3-32 and 3-33, a single high spike or two in the rain rate triggers a comparatively long period during which the received signal essentially remains low and flat, merely fluctuating within a difference of 1 to 2 dB or less. This pattern is seen in every rain event that resulted in total squelching of the TV reception.

As seen in Figure 3-32, a single group of rain spikes triggered the long period of low, flat received signal levels. But in other examples such as the event illustrated in Figure 3-33, two different groups of rain spikes are seen to be responsible for two separate periods of signal outage. The brief period of low rain rate in between them also registered a spell of improved reception. Equal number of groups of rain peaks result in equal number of outage “flats” in the received signal time series. It is to be noted however that the signal remained at outage levels for several minutes after the second group of rain peaks had given way to near-zero rain rate values, that is after rain had almost totally subsided.

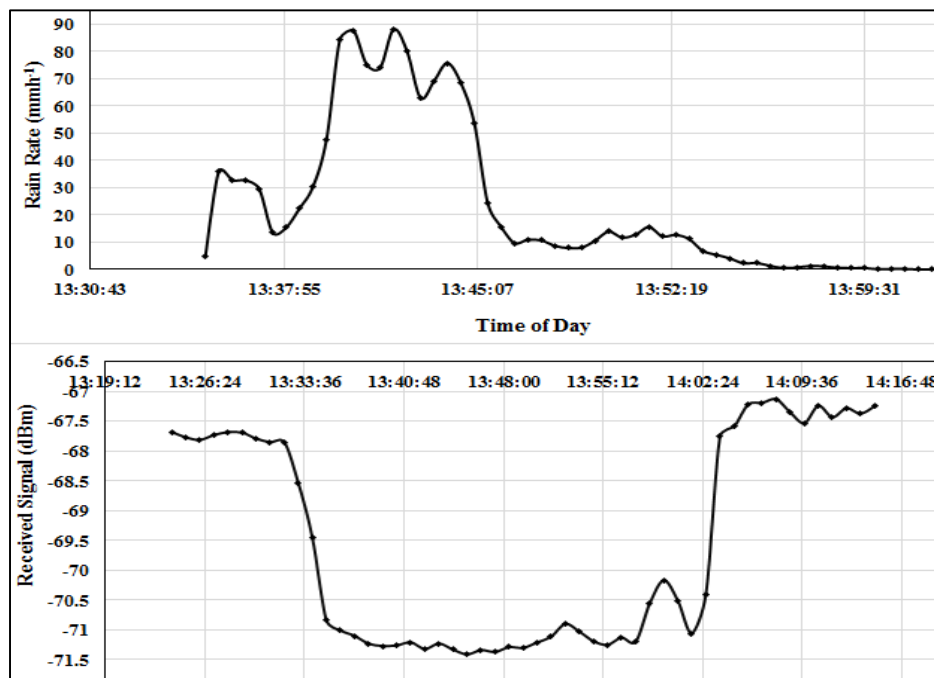


Figure 3-32: Synchronized attenuation-precipitation time series during a 2013 thunderstorm event that resulted in loss of reception.

The events illustrated in Figures 3-32 and 3-33 respectively represent the highest rain events of 2013 and 2014. The event in Fig. 3-32 features a year-high rain rate of 89.5 mmh^{-1} for 2013 while the event in Figure 3-33 includes the year-high rain rate of 82.09 mmh^{-1} for 2014. The extended period of outage experienced is atypical for a subtropical location such as Durban, occurring only a few times in a rain season (typically when the $R_{0.01}$ value is exceeded).

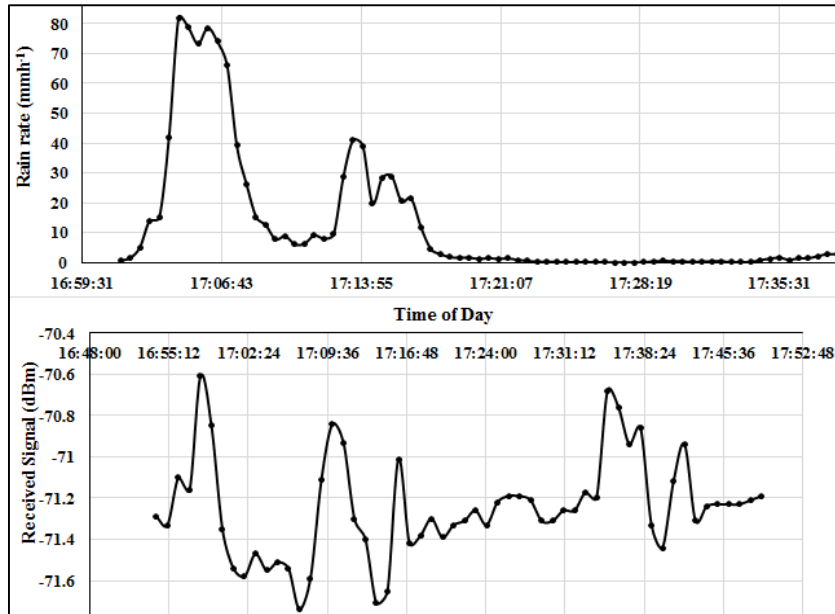


Figure 3-33: Synchronized attenuation-precipitation time series during a 2014 thunderstorm event that resulted in a loss of reception

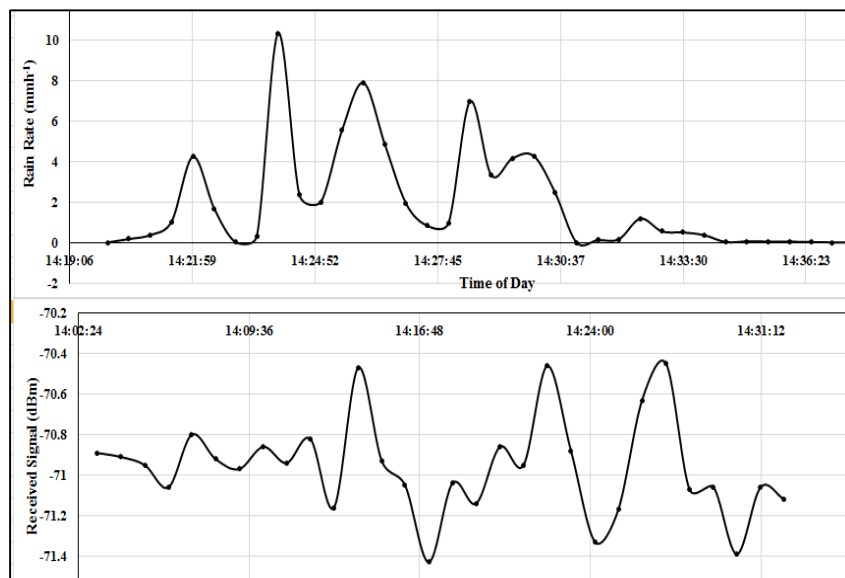


Figure 3-34: Synchronized attenuation-precipitation time series during a 2014 shower event that resulted in loss of reception

The more common pattern of signal squelching is seen in the events in figures 3-34 and 3-35. Both are shower events with peak rain rates of 28.5 mmh^{-1} and 10.35 mmh^{-1} respectively. But both events resulted in signal squelching, albeit for very short instances.

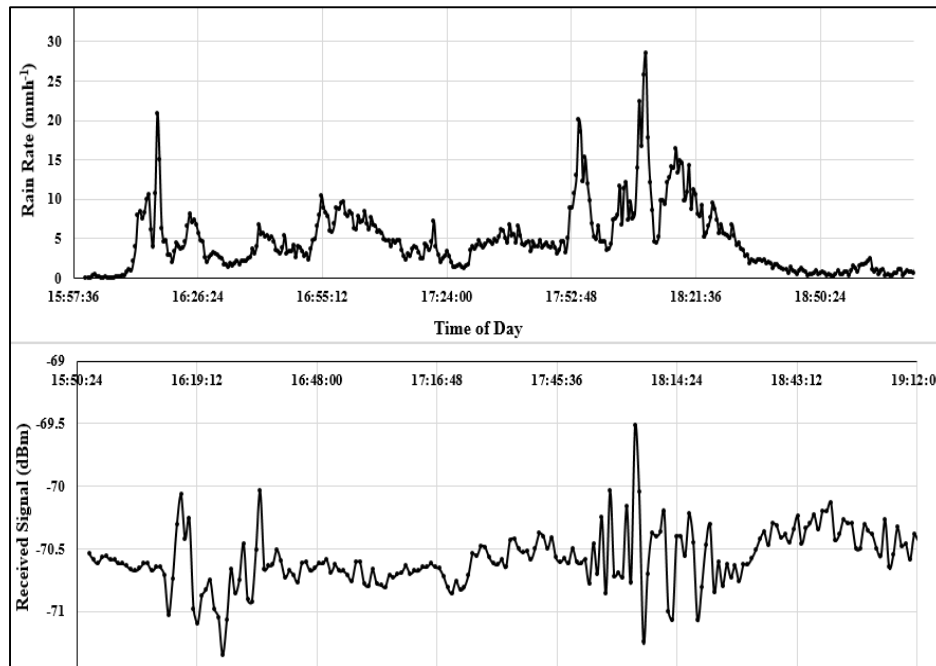


Figure 3-35: Synchronized attenuation-precipitation time series during a 2014 shower event that resulted in loss of reception

As seen in the matching timeline of the received signal, the reception at these relatively low rain rates instantaneously dropped below the -71 dBm mark (the level at which squelching usually occurs) several times during the rain event. This results only in momentary loss of reception but it also persists for a little longer than the time of occurrence of the peak rain rates. The reason behind such unexpected severity of the rain attenuation at such relatively low rain rates (compared to the $R_{0.01}$ values) is partly explained by the long path length in the rain zone which is not necessarily covered by the disdrometer. But it is a common phenomenon throughout the measurement period.

It should be noted that total squelching can occur on a slant path at other times due to heavy fog conditions and a few other less common events. The pattern of squelching covered in this work is with specific reference to periods of actual precipitation at the receive antenna only. Other forms of squelching were not studied.

The actual nature of occurrence of total squelching of the signal on a satellite TVRO link consistently but slightly varies from general theory of rain attenuation, which assumes that attenuation will bear a direct correlation to rain rate all through the rain event [65]. Outage persists for several minutes after the spike in rain rate that triggered it had subsided. Instantaneous squelching also occurs sometimes at relatively low rain rates at which it is not anticipated. The dynamics observed on the link needs to be put into consideration in future planning of rain attenuation mitigation schemes on such slant path links. Such a scheme must be based on an intelligent system that can anticipate not only the behaviour of rain spikes but also simultaneously anticipate that of the received signal level.

3.8 Chapter Summary

This chapter outlines the results of measurements of the received signal level on a microwave satellite TV link and the rain rate data accumulated by a disdrometer co-located with the microwave receive antenna. Signal attenuation statistics over the link as extracted by matching the rain rate spikes with the RSL dips in the time domain was reported. The minimum and the maximum attenuation statistics at each rain rate was sorted into separate bounds and an average bound was created from the data. The data was used as input into a computer algorithm to obtain power law and logarithmic equations for each bound by regression analysis. Rain rate and attenuation exceedance probability for various seasons of the year at the location are analysed and presented. The rain attenuation model was compared with four theoretical models for statistical validation. The results of the comparison are presented. Lastly, a brief report on the pattern of observation of signal squelching on the link is also presented in the chapter.

CHAPTER 4: GENERATION OF RAIN ATTENUATION TIME SERIES FROM MEASUREMENT-DERIVED PDFS BY MARKOV CHAIN PRINCIPLE

4.1 Introduction

The long term purpose of a rain attenuation measurement campaign such as was reported in chapter three is to provide an empirical basis for evolving a climate-specific prediction system that can be applied to any other hypothetical link for system planning and post-deployment evaluation and improvement. While the results of rain attenuation apply directly only to the specifics of the experimental link used for the measurement, it essentially presents an empirical picture of what is statistically a random variable. Rain attenuation qualifies as a random variable because rainfall is a random event and the occurrence of rain spikes obey the mathematical principles of random, being products of natural events that vary widely both in spatially and temporally [50], [62], [87].

In this chapter, some random number characteristics of the results of rain attenuation measurement on the Ku-band satellite TV link reported in chapter three shall be extracted. These characteristics shall be used to evolve a Markovian method for generating rain attenuation time series that will fit subtropical rain conditions. With such results, several datasets of future seasonal and annual statistics of rain attenuation are projected based on measurements carried out during the past years and seasons [8].

4.2 Basic Markov Chain Principles

The fundamental logic behind the Markov model follows from classical Newtonian world view in which in the real world, the future is usually independent of the past, given that the present is known. The canonical probabilistic model for time-sequential data which is random in nature is a Markov Chain [93, 94]. If the present state of the variable is known, the process of the future states does not depend on the past states either they are known or not. Markov models can apply to any temporal data such as the weather, the stock market, commodity prices and so on. The property of being independent of past states is sometimes described as the chain being memoryless. For our purpose, we define a random variable array $A(k)$ representing all the values of A at k discrete instances of time in a dynamic for all cases from $n = 1$ to $n = k$ as

$$A(k) = [A_1, A_2, A_3, \dots, A_n, \dots, A_{k-1}, A_k] \quad (4.1)$$

We can describe the sequence as Markovian if the probability of occurrence of A at any instant of time t_n is such that

$$P(A_i/A_1, A_2, A_3, \dots, A_{i-1}) = P(A_i/A_{i-1}) \quad (4.2)$$

Hence,

$$P(A_1, A_2, A_3 \dots A_n) = P(A_1), P(A_2/A_1), P(A_3/A_2) \dots P(A_n/A_{n-1}) \quad (4.3)$$

The array in equation (4-1) defines the entire state space of A_k and each member defines a *state* of the random variable. The variable possesses the Markov property if and only if for any state A_n , all the elements of the matrix of future states [$A_{n+1}, A_{n+2} \dots A_{k-1}, A_k$] are independent of the past states but dependent only on the present state. This model describes a first-order discrete time Markov Chain. Higher orders depend on how far back we look down the chain in order to predict the next state. Certain variables such as Brownian Motion and Poisson processes yield continuous time Markov chains. The discrete time Markov chain is a simplified version of the continuous time Markov chain which is obtained by extracting the states of the random variable at given regular instants of time from the continuous state space [95].

The occurrence of rain attenuation on any communication link over a time period is a random variable predicated upon by the occurrence of rain rate spikes interacting with the satellite beam. These spikes are time-variant and take on random values. Thus we can conclude that rain attenuation will canonically occur in a Markovian process. This conclusion forms the basis for adopting a Markov model for generating rain attenuation time series under varying conditions and it can be achieved by deriving the Markov parameters of the rain attenuation time series obtained from actual measurements.

Prediction of rain attenuation over a communication link for whole periods of rain seasons and years shall be attempted by mathematically parameterizing two vectors that represent how the rain attenuation occurs in the time domain and how it changes or transitions in the time domain. The important Markov parameters for simulating rain attenuation time series are basically mathematical characterizations of these two dynamics.

To generate the rain attenuation time series for a period, a season or a year as the case may be, we shall obtain the following:

A. *The State Probability Matrix*

A sequential array of the probability of occurrence of every successive state of the time-varying random variable is termed the state probability matrix. The entire state space of the variable is defined for a given set of conditions – which are usually guided by its limitations for occurring in time and space. The discrete probability of occurrence of each state is then obtained based on these conditions. For all the possible states occupied by the random variable, we can define a matrix of probabilities such as

$$P_k = [P_1, P_2, P_3 \dots P_n \dots P_{k-1}, P_k] \quad (4.4)$$

where each element is the discrete probability of occurrence of each state in the A_k array. P_k is the state probability matrix of A_k . It always a $(1 \times k)$ matrix whose elements must fulfil the probability density function condition of adding up to unity. This array is equivalent to and obtainable from the complete Probability Distribution Function (PDF) of the random variable, either discrete or continuous. To apply the state probability matrix for simulating a Markovian sequence, the distribution must be tested to ascertain the distribution type. The Figure 4-1 illustrates the state space probability vector.

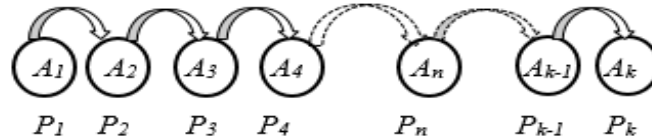


Figure 4-1: State Space and State Probability Matrix

The variable in question being rain attenuation in this case, the state probability matrix coincides with the PDF of measured rain attenuation over the period defined.

B. State Transition Probability Matrix

Every chain or sequence is basically a series of transitions between states. While the state probability matrix defines the probability of occupying each discrete state, the state transition matrix is a little more complex array. It is a $(k \times k)$ matrix that describes the probability of occurrence of all changes of state that the random variable can possibly experience. It includes the probabilities of transition from each state back to itself and to all the other states in the state space. Consider a five-state random variable illustrated in Figure 4-2, all the elements of the (5×5) state transition probability matrix are as shown in the figure.

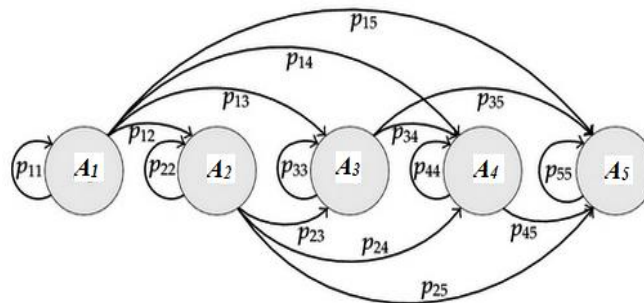


Figure 4-2: State transition probabilities of a 5-state Markov Chain.

Algebraically, if the probability of transition from a state p_i to a state p_j is p_{ij} and the random variable occupies k possible states, then the state transition probability matrix is given by

$$P_T = \begin{bmatrix} p_{11} & p_{12} & \dots & p_{1k} \\ p_{21} & p_{22} & \dots & p_{2k} \\ p_{31} & p_{32} & \dots & p_{3k} \\ \vdots & \vdots & \ddots & \vdots \\ p_{k1} & p_{k2} & \dots & p_{kk} \end{bmatrix} \quad (4.5)$$

An N -state Markov chain generated by obtaining the product of the state probability matrix and the transition probability matrix will be a PDF of the rain attenuation time series in a future time period given by

$$P_{1sim} = P_T \times P_k \quad (4.6)$$

This product yields a $I \times k$ matrix that represents a first iteration of the Markov-generated PDF. Its parameters can be utilized to generate a time series that simulates A_k with the MATLAB code. If P_k represents the state probability matrix of rain attenuation for an entire summer season for example, then the first iteration represented by the vector P_{sim} is the state probability matrix simulated to represent the PDF of attenuation time series summer season of the following year. For the second year after that, two transitions would have occurred. Thus, the second iteration will be given by

$$P_{2sim} = P_T^2 \times P_{1sim} \quad (4.7)$$

A third iteration for obtaining the rain attenuation PDF of the summer season in the third year after the year represented by P_k will be given by

$$P_{3sim} = P_T^3 \times P_{2sim} \quad (4.8)$$

This can be done for a seasonal PDF or an annual PDF as is required for system planning and design. For the n th year or season after the one for which measured attenuation data is available,

$$P_{n-sim} = P_T^n \times P_{(n-1)sim} \quad (4.9)$$

The state transition probability matrix is held unchanged in the process but the state probability matrix of the previous year (or season) is used to simulate that of the present year. For the PDFs under consideration in this work having several thousands of states each, a few transitions is adequate for planning towards link deployment. Higher orders will be successively less useful as repeated transitions of a Markov chain takes it towards a statistical steady state in which subsequently produces the same resultant PDF or one with no significant difference from the previous iteration [95].

In the equations 4-7 to 4-9, the product on the right hand side will always yield a $I \times k$ matrix which is of the same distribution type as P_k from equation 4-6. As shall be demonstrated, the distribution is lognormal in this case. The resultant discrete PDF represented by the left hand side is used to generate the required rain attenuation time series.

4.3 Probability density functions of measured attenuation

From the results of measured slant path rain attenuation reported in chapter three, a time series of attenuation for every period for which we have the rain rate time series is available can be generated. In the expressions for measured attenuation model presented in bounds in Table 3-8, the most significant for system planning is the maximum bound. This is because system design is aimed at preparing the link to handle the worst conditions that can occur in nature rather than the best conditions. Thus, we can generate measured monthly, seasonal or annual rain attenuation time series for the Ku-Band link using the governing power law expression for measured slant path attenuation on the measurement link given as

$$A = 2.7567R^{0.2693} \quad (\text{dB}) \quad (4.10)$$

The time series thus generated presents a full statistics of the rain fade that occurs on the link at every instant of time of precipitation throughout the period covered. The rain time series used is a record of the rain rate captured at 30-second intervals during all precipitation events at the location. Similar rain rate data accumulated by the disdrometer throughout the years 2015 and 2016 were incorporated into the work at this stage. Hence, the attenuation time series will also be a reliable estimate of the attenuation measured on the link at 30-second intervals during all rain events in the period. From this time series, the probability distribution of the rain attenuation was estimated and the fitting distribution of the PDF was determined [96].

The attenuation time series for each of the four seasons of summer, autumn, winter and spring of 2013/2014 seasonal cycles were simulated separately while that of each of the years 2013, 2014, 2015 and 2016 were also done separately. A bin resolution of 0.01 dB was applied to the seasonal data while a bin of 0.1 dB was applied to the annual data.

In all the cases, the PDFs of the rain attenuation data were found to obey the lognormal distribution. A random variable X is lognormal-distributed if the quantity $\ln(X)$ exhibits a normal distribution and the mean σ and standard deviation μ of $\ln(X)$ are such that X can be obtained as

$$X = e^{\mu + \sigma Z} \quad (4.11)$$

where Z refers to the standardized normal variable.

In terms of the lognormal-distributed rain attenuation A_i , the probability of occurrence of a certain bin of attenuation A_i at a given time instant is given by [96]

$$P(A_i) = \frac{1}{\sqrt{2\pi}\sigma A_i} \exp\left(-\frac{\ln(A_i/\mu)^2}{2\sigma^2}\right) \quad (4.12)$$

where of $\ln(A_i)$ respectively. The lognormal characteristics of the PDFs was confirmed by RMS error and Chi-square analyses values obtained when holding the estimated PDF as the expected value and the fitted as the observed value. The parameters used to carry out a lognormal fit of the raw data are presented in Table 4-1. The results of the statistical error analysis presented in Table 4-2 demonstrate conclusively that the seasonal and annual attenuation statistics are indeed a lognormal fit. Examples of the measurement model-generated time series of rain attenuation are presented in Figures 4-3 and 4-4.

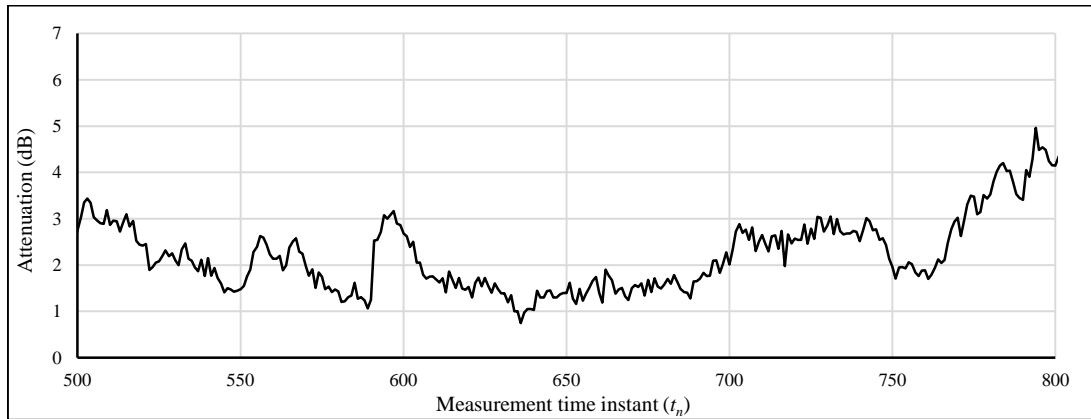


Figure 4-3: Rain attenuation time series in the 500th to 800th time instant of rain during winter season in Durban in 2013 ($f=12.6$ GHz, $\theta = 36.5^\circ$, $t_n = 30$ seconds).

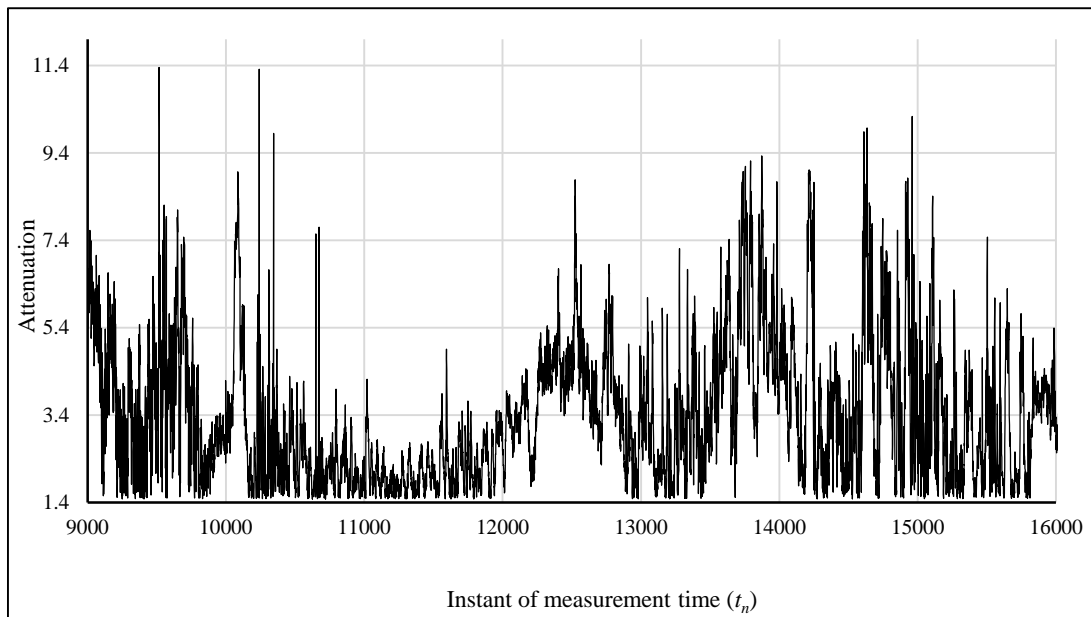


Figure 4-4: Rain attenuation time series in the 9,000th to 16,000th time instant of rain in Durban in 2016 ($f=12.6$ GHz, $\theta = 36.5^\circ$, $t_n = 30$ seconds).

Table 4-1: Lognormal parameters of the seasonal and annual rain attenuation PDFs

Period	μ of $\ln(A_i)$	σ of $\ln(A_i)$
Winter	0.678338939	0.219818394
Spring	0.572859016	0.20204145
Summer	0.647848347	0.202631008
Autumn	0.724339311	0.173741231
2013	0.880215825	0.106941349
2014	0.862730118	0.100167138
2015	0.909487664	0.132613641
2016	1.039428176	0.179421822

Table 4-2: Error Analysis of the lognormal-fitted attenuation statistics

Period	RMS Error	χ^2 Value	χ^2 Critical Value	Chi-Test Result
Summer	0.0042	0.0596	616.878	Accept
Autumn	0.00579	0.0829	605.667	Accept
Winter	0.07432	1.3677	592.909	Accept
Spring	0.00806	0.129	620.241	Accept
2013	0.02712	2.4287	108.77	Accept
2014	0.00776	0.0841	103.158	Accept
2015	0.00748	1.6627	98.484	Accept
2016	0.00575	0.0955	104.576	Accept

In the Figures 4-5 to 4-12, the PDFs of the slant path attenuation time series during the four subtropical rain seasons of 2013 and 2014 are presented, while Figures 4-9 to 4-12 are the PDFs of the measured slant path attenuation time series for all rain spikes recorded for each of the years 2013, 2014, 2015 and 2016. A numerical integration of the discrete PDFs gives a result that closely approximates to unity.

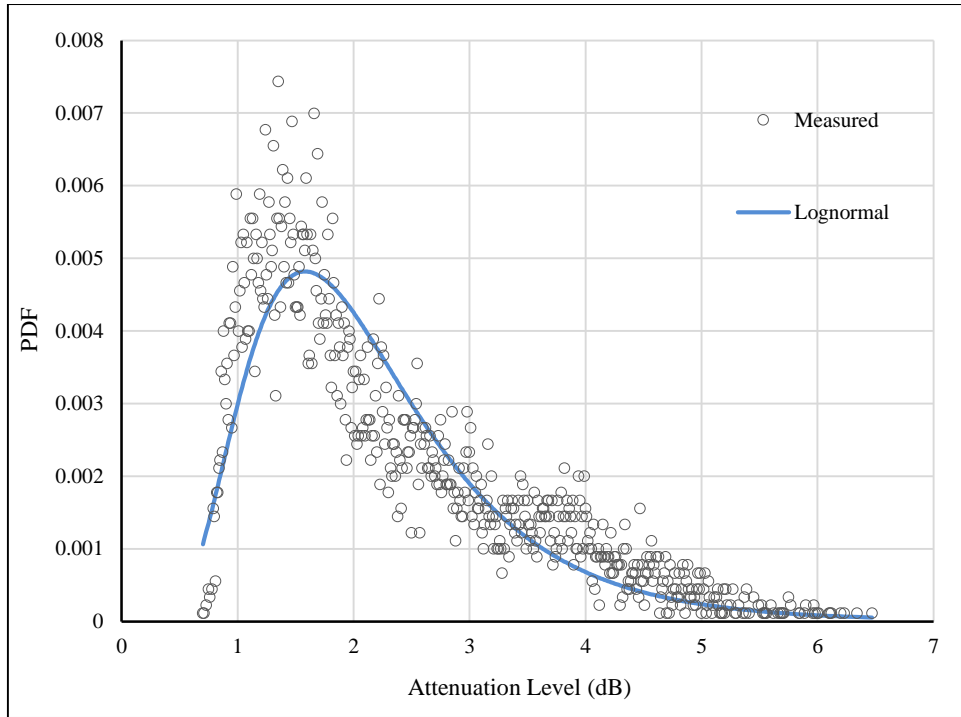


Figure 4-5: PDF of slant path rain attenuation statistics in a winter season in Durban. ($f = 12.6$ GHz, $\theta = 36.5^\circ$)

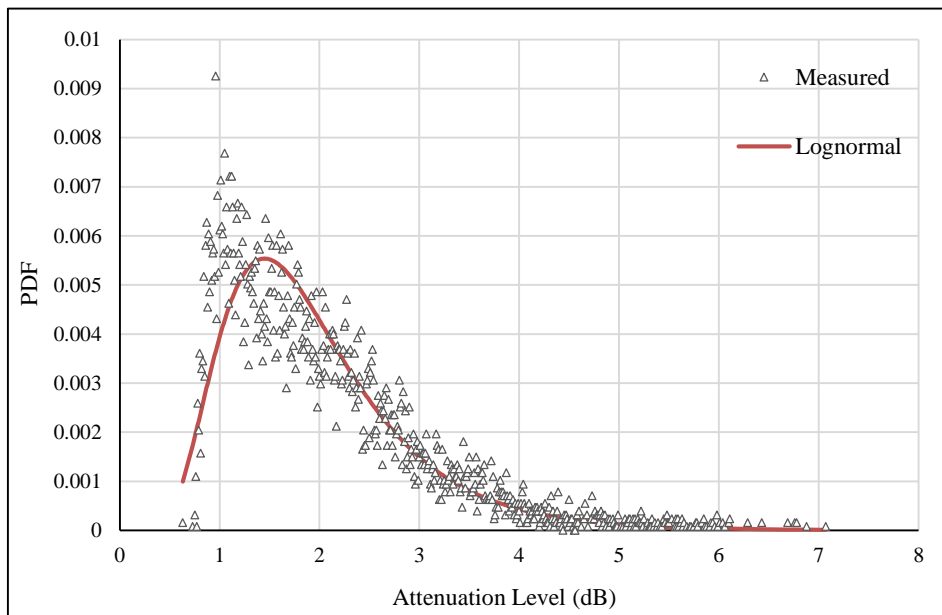


Figure 4-6: PDF of slant path rain attenuation statistics in a spring season in Durban. ($f = 12.6$ GHz, $\theta = 36.5^\circ$)

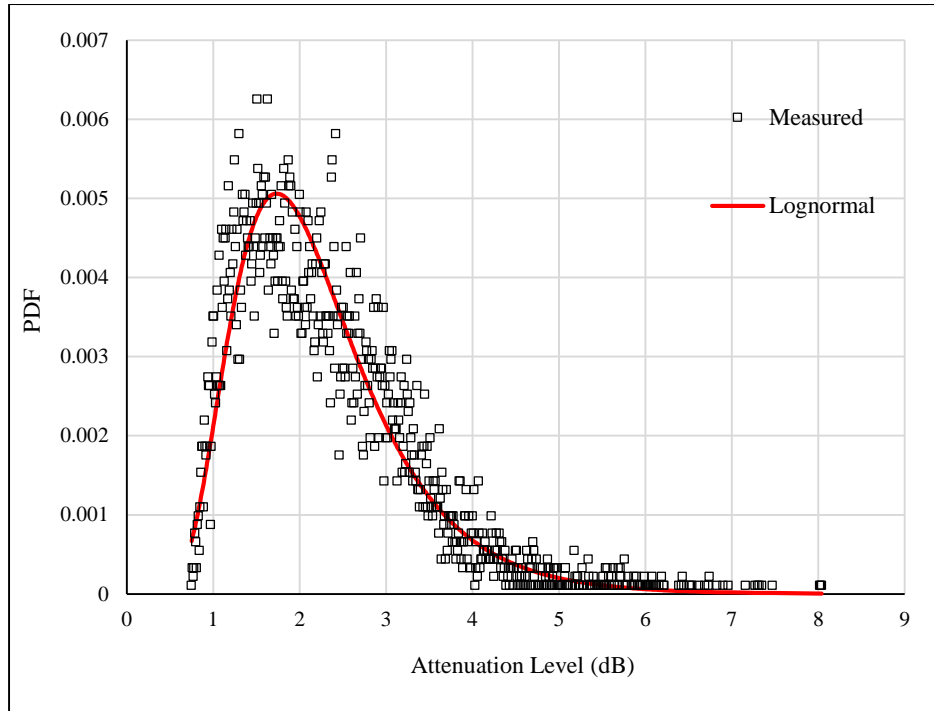


Figure 4-7: PDF of slant path rain attenuation statistics in an autumn season in Durban. ($f = 12.6$ GHz, $\theta = 36.5^\circ$)

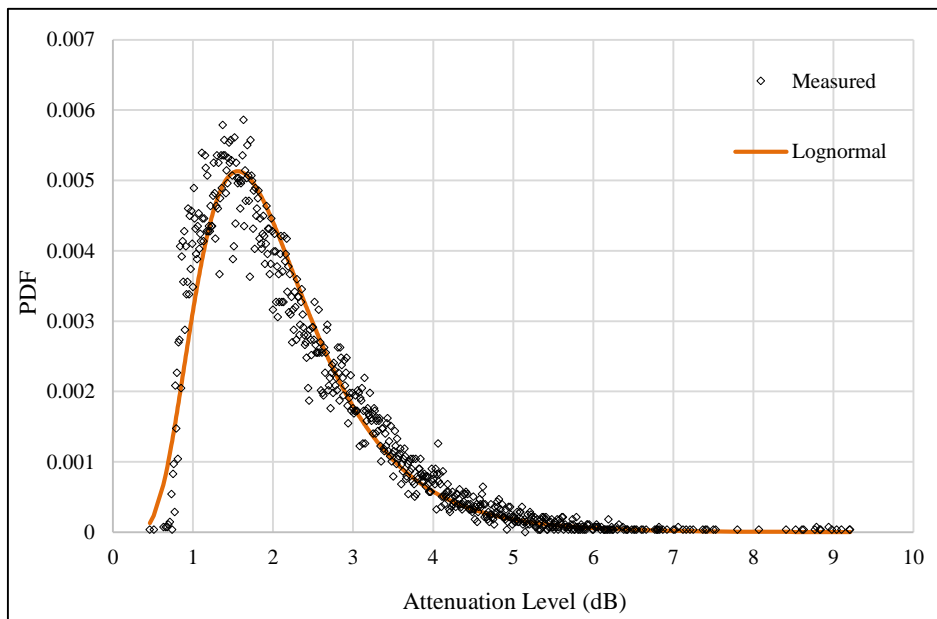


Figure 4-8: PDF of slant path rain attenuation statistics in a summer season in Durban. ($f = 12.6$ GHz, $\theta = 36.5^\circ$)

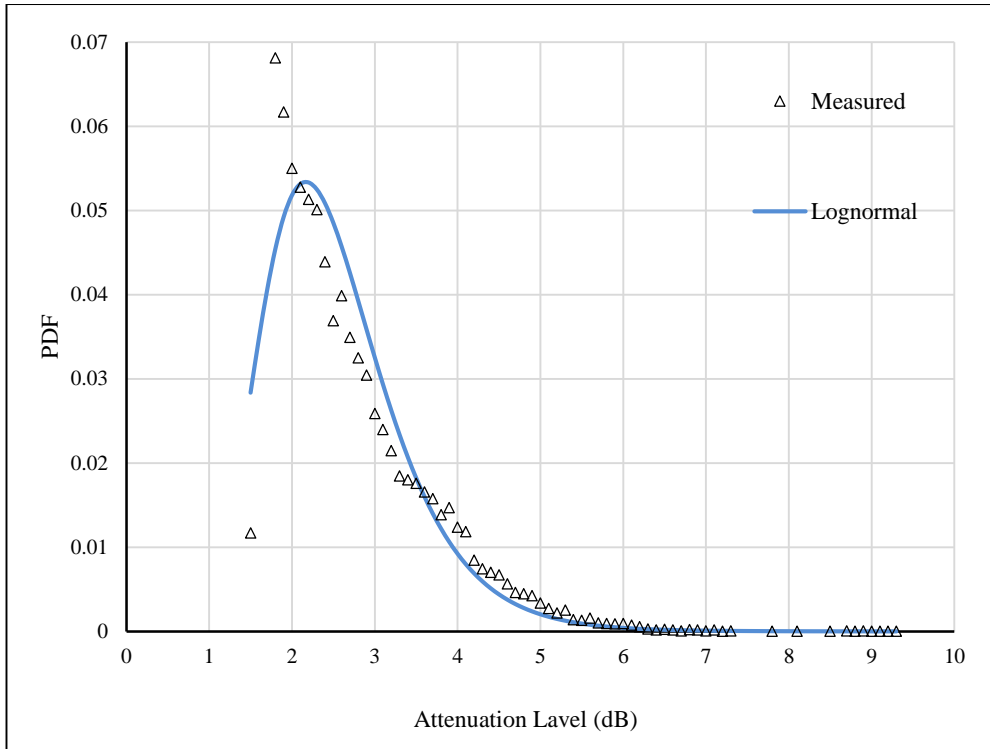


Figure 4-9: PDF of slant path rain attenuation statistics in 2013 in Durban. ($f = 12.6 \text{ GHz}$, $\theta = 36.5^\circ$)

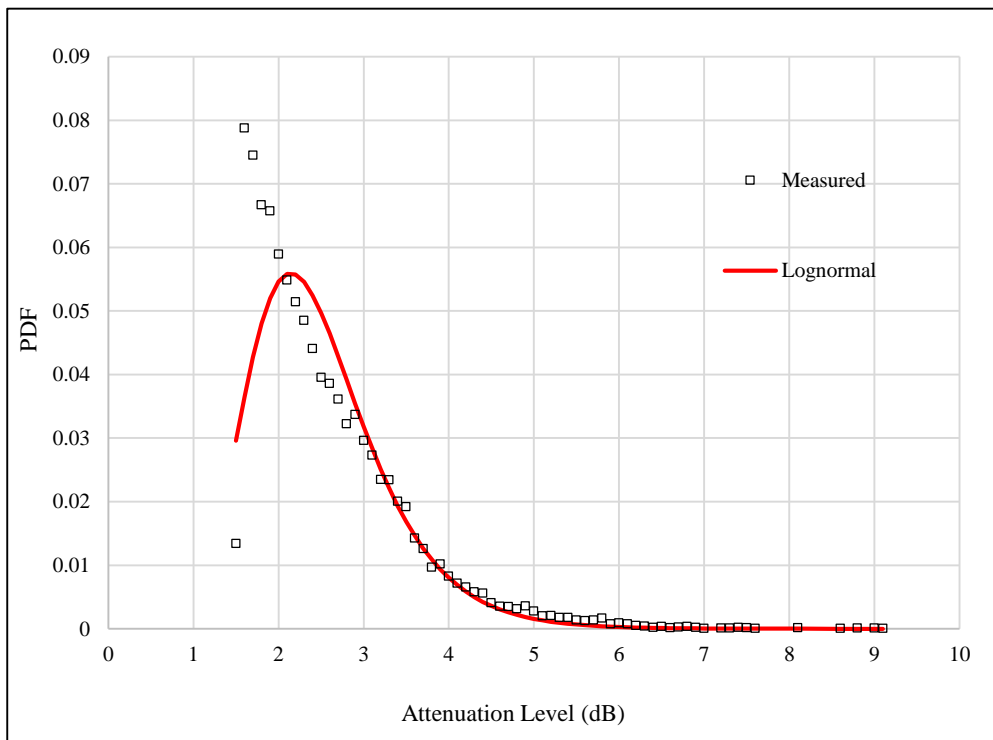


Figure 4-10: PDF of slant path rain attenuation statistics in 2014 in Durban. ($f = 12.6 \text{ GHz}$, $\theta = 36.5^\circ$)

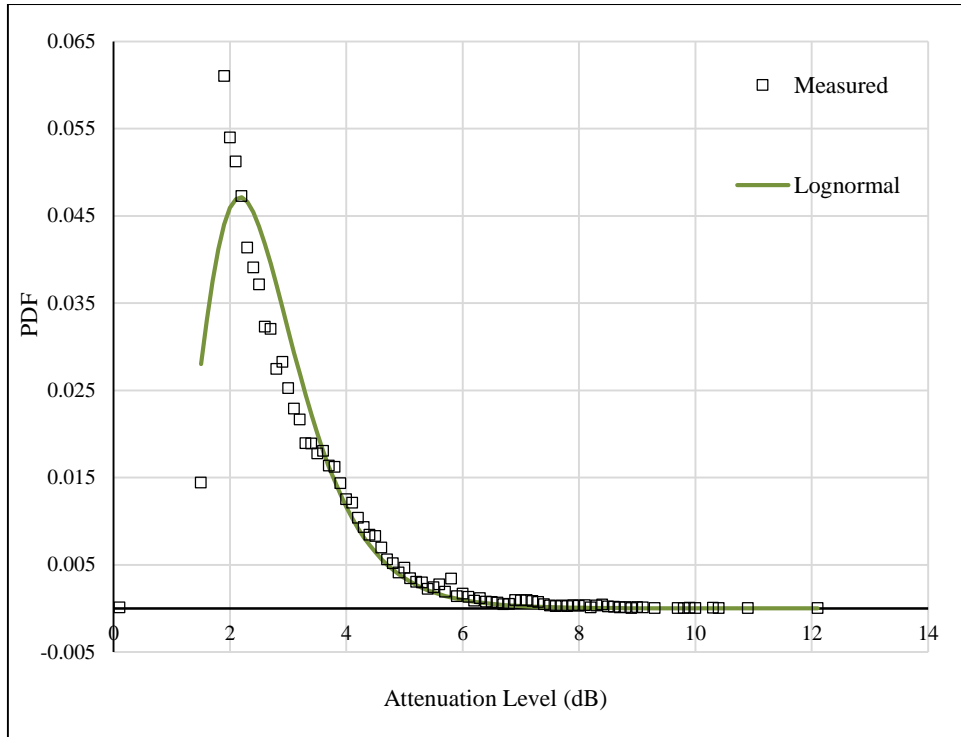


Figure 4-11: PDF of slant path rain attenuation statistics in a 2015 in Durban. ($f = 12.6 \text{ GHz}$, $\theta = 36.5^\circ$)

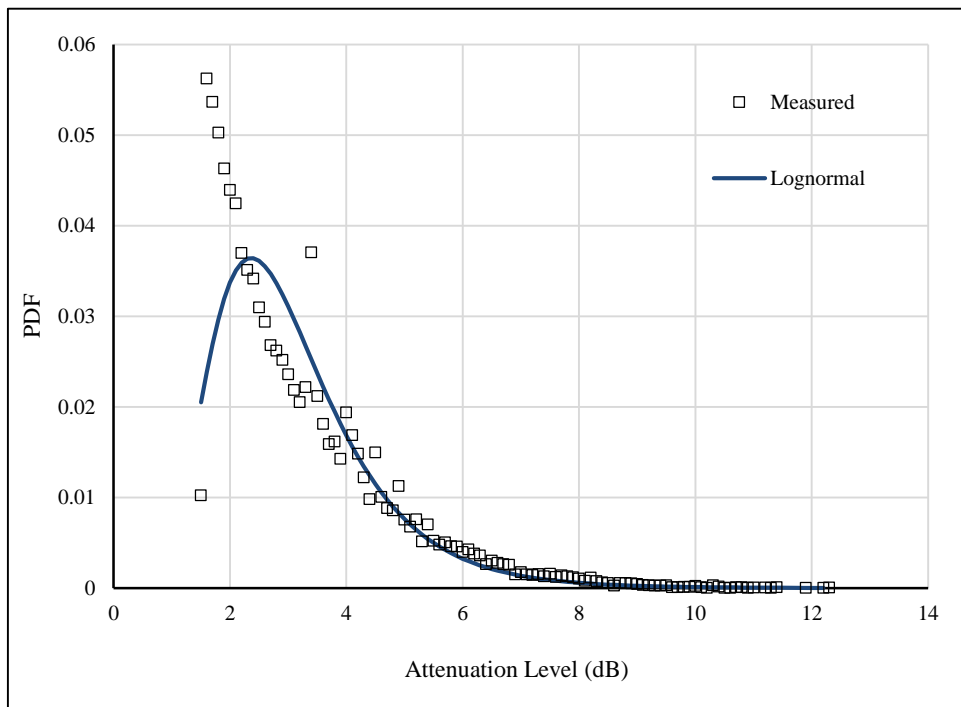


Figure 4-12: PDF of slant path rain attenuation statistics in 2016 in Durban. ($f=12.6 \text{ GHz}$, $\theta = 36.5^\circ$)

4.4 State Transition Probability Matrix and Fade Slope Statistics

The nature of transition of a random variable between two states is often dependent on one intrinsic property of the system or the other. While the next state assumed remains entirely random, it is possible

to determine the probability of transition between any two states in the state space [94]. For rain attenuation occurring over a range of time, the fade slope ζ defined in equation 4-12 is related to the transition probability at the given attenuation level as it expresses the rate at which the attenuation state is changing temporally at that particular time instant [97].

$$\zeta (A_k) = \frac{A_{k+1} - A_{k-1}}{2} \quad (4.12)$$

where ζ is measured in decibels per simulation time unit (dB/STU). The simulation time unit is the time between the occurrence of attenuation A_k and A_{k+1} . ζ can be approximated as $\tan \alpha$ over the range of attenuation represented by the portion of the curve indicated in the Figure 4-13.

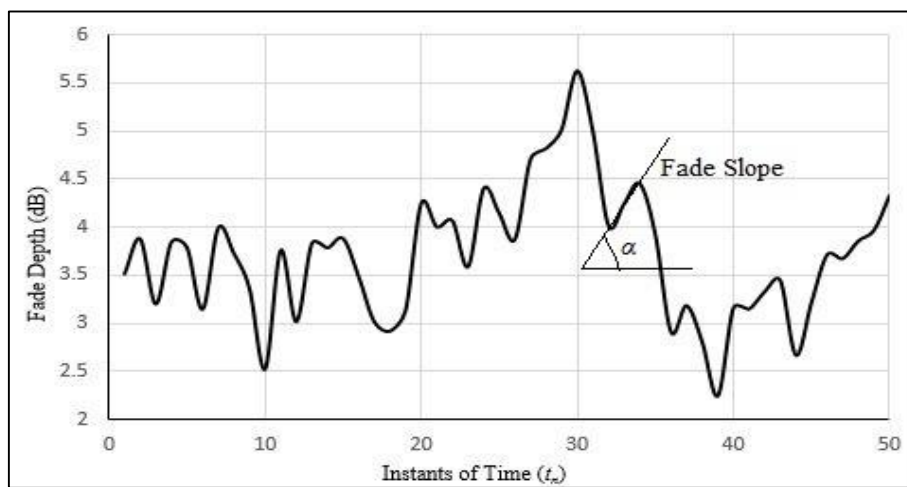


Figure 4-13: Illustration of fade slope using a 50 t_n rain fade time series during Summer in Durban. ($f=12.6$ GHz, $\theta = 36.5^\circ$)

By inspection and from literature, it is easily deduced that the probability density function of fade slope is a Gaussian (normal) distribution [97], [98], [99]. As seen from Table 4-3, a simple error analysis of the PDF of the fade slope of the measured attenuation model indicates a very good fit for the Normal distribution. The state transition probability matrix is derived from the general model of fade slope PDF for the desired time period, which in this case coincides with the seasonal and annual cycles of subtropical rainfall [100], [101]. The Gaussian-fitted model of fade slope was obtained using the expression [95]

$$P_\zeta = \frac{1}{\sigma\sqrt{2\pi}} e^{-\frac{(\zeta-\mu)^2}{2\sigma^2}} \quad (4.13)$$

where μ is the arithmetic mean of the measured fade slope and σ is its standard deviation.

Table 4-3: Error analysis of the normally-distributed attenuation statistics

Period	RMSE of fitted Gaussian PDF
Winter	0.001358502
Spring	0.001911021
Summer	0.00140679
Autumn	0.001950714
2013	0.001373703
2014	0.001804793
2015	0.002034156
2016	0.002031804

The $N \times N$ state transition probability matrix is derived from the Gaussian fade slope PDF. Each discrete element of the fade slope PDF (P_{ζ}/A_k) represents the fade slope at a certain attenuation level A_k . The next sequential element (P_{ζ}/A_{k+1}) represents the fade slope at the next bin resolution (0.01 dB for seasonal data and 0.1 for the annual data). During a transition from an attenuation state A_i to any other attenuation state A_j in the time series, the transition probability P_{ij} (Figure 4-14) corresponds to the value of P_{ζ} that most nearly approximates [101]

$$P(\zeta = (A_j - A_i)/2|i) \quad (4-14)$$

The fade slope PDF is a discrete array, being derived from real data. Thus, this approximation is done by using a MATLAB code to perform an integral sum around the estimated fade slope value that corresponds to the value of ζ in equation 4-14.

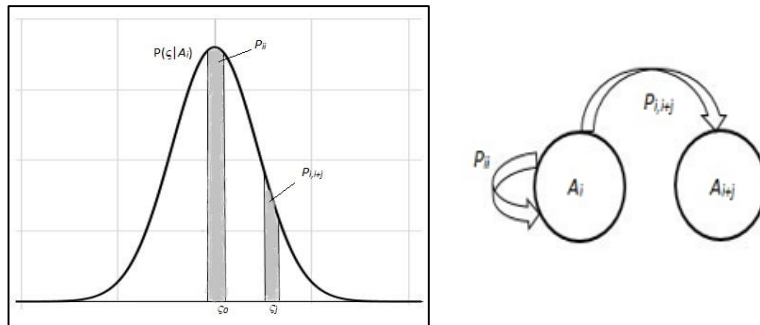


Figure 4-14: Approximation of each element of the state transition probability matrix from fade slope PDF

The Figures 4-15 to 4-18 present the PDFs of fade slope for each of the four rain seasons of the years 2013 and 2014 in Durban, South Africa while Figures 4-19 to 4-22 show the annual fade slope PDF for

the years 2013 to 2016 at the same location. The data was obtained by calculating the fade slope corresponding to each slant path attenuation event obtained from the measurement model based on disdrometer data as reported in chapter 2. The area under each of the curves integrates to unity. The Gaussian-fitted discrete PDF is used for the simulation. In the Table 4-4, the values of mean μ and standard deviation σ parameters of the Gaussian distributed fade slope for each dataset, used for the fitted PDF, are presented.

Table 4-4: Gaussian mean and standard deviation for periodic datasets of fade slope

Period	μ	σ
Winter	-4.12757E-05	0.221646345
Spring	-3.0458E-05	0.293613523
Summer	2.04553E-05	0.25804257
Autumn	-0.000285915	0.279587725
2013	1.63873E-06	0.271351487
2014	-4.76619E-06	0.270441366
2015	3.09309E-05	0.351753864
2016	-3.88423E-05	0.420769372

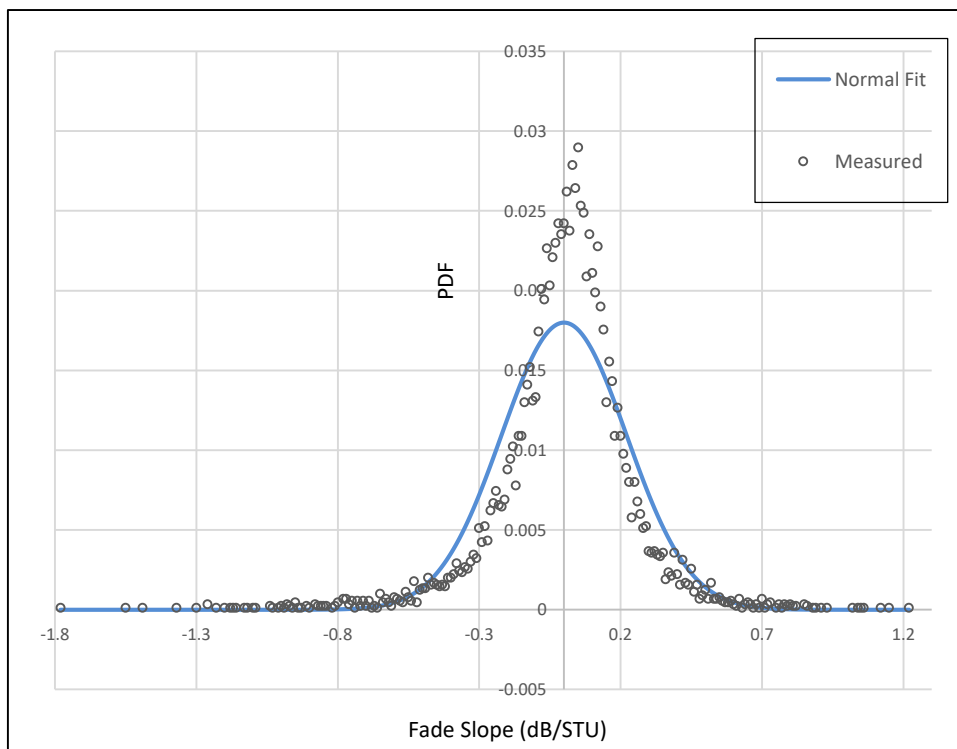


Figure 4-15: PDF of the fade slope of measured attenuation in a subtropical winter season

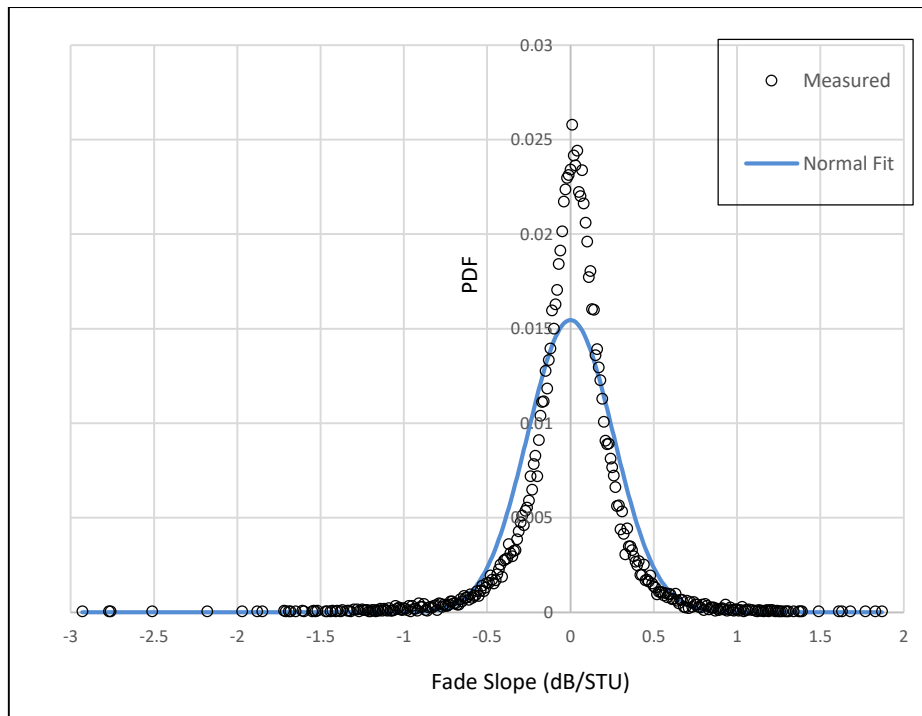


Figure 4-16: PDF of the fade slope of measured attenuation in a subtropical summer season

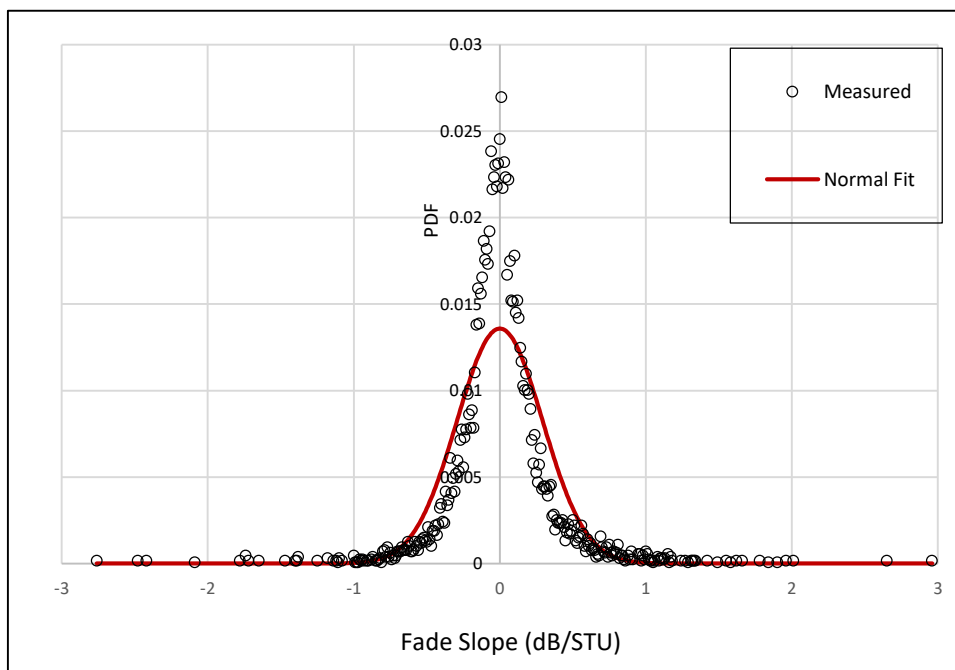


Figure 4-17: PDF of the fade slope of measured attenuation in a subtropical spring season

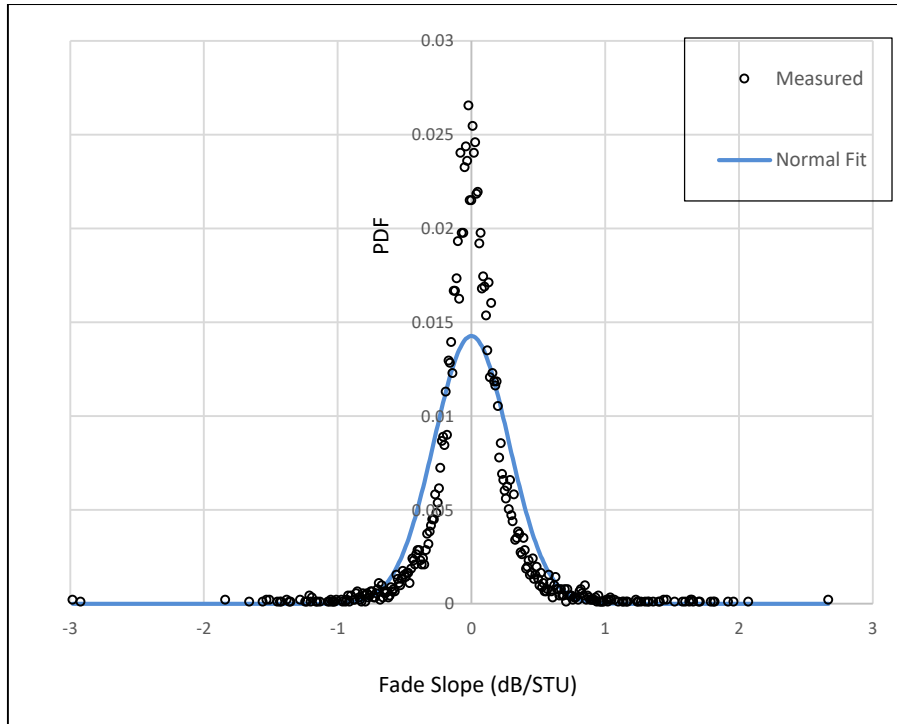


Figure 4-18: PDF of the fade slope of measured attenuation in a subtropical autumn season

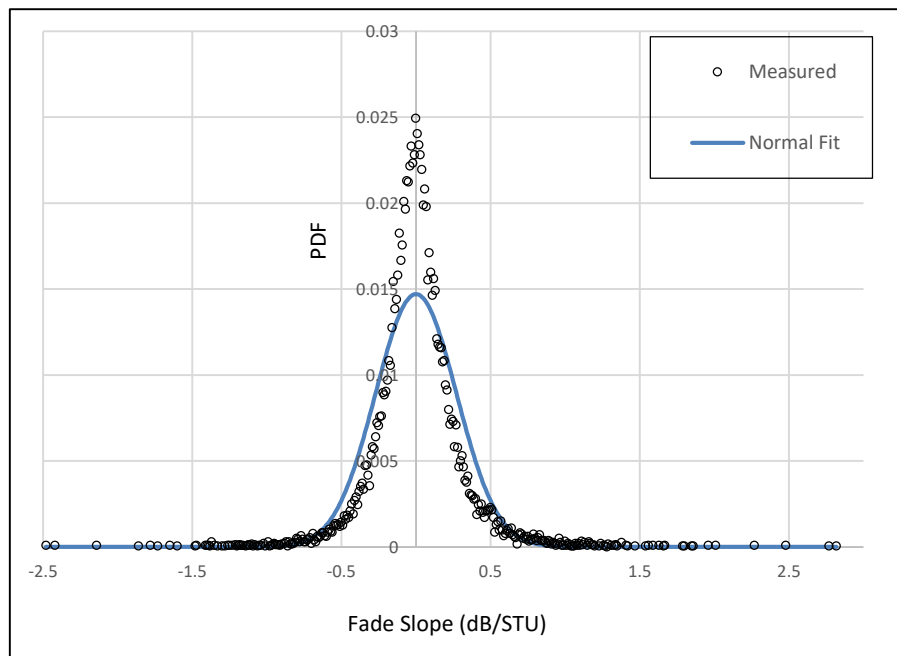


Figure 4-19: PDF of the fade slope of measured attenuation in 2013 in Durban

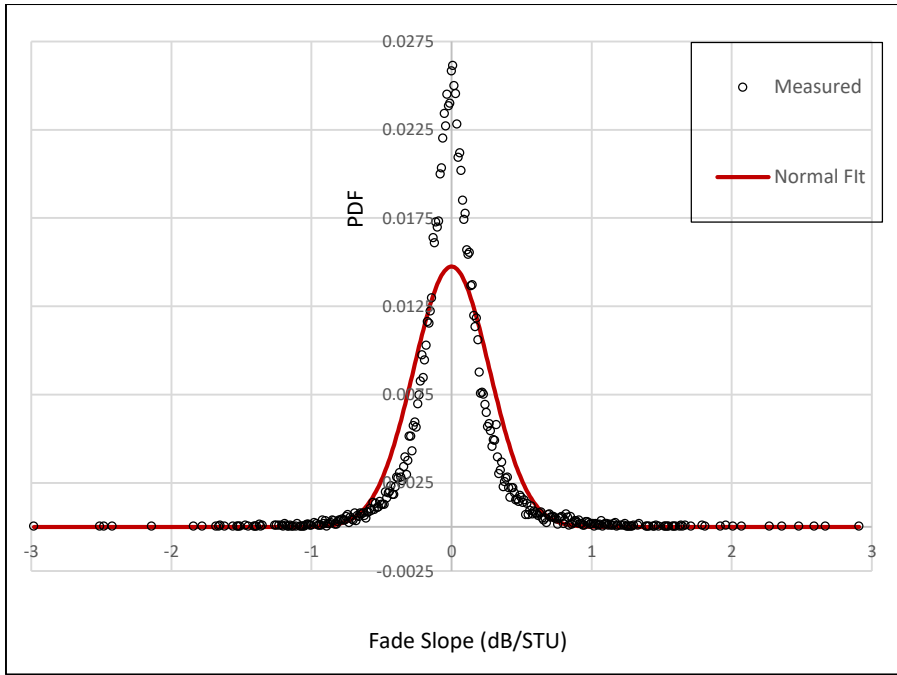


Figure 4-20: PDF of the fade slope of measured attenuation in 2014 in Durban

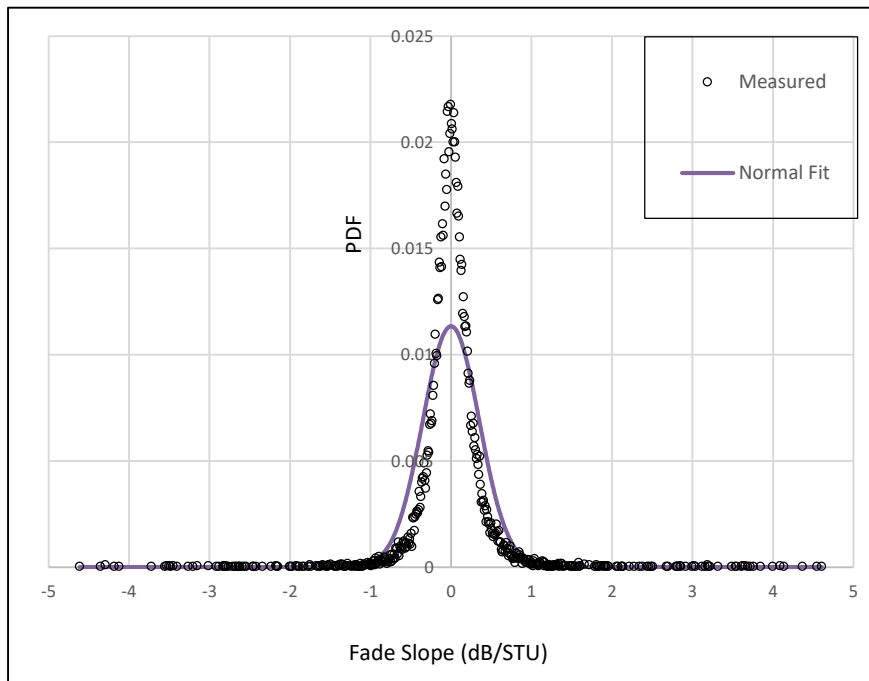


Figure 4-21: PDF of the fade slope of measured attenuation in 2015 in Durban

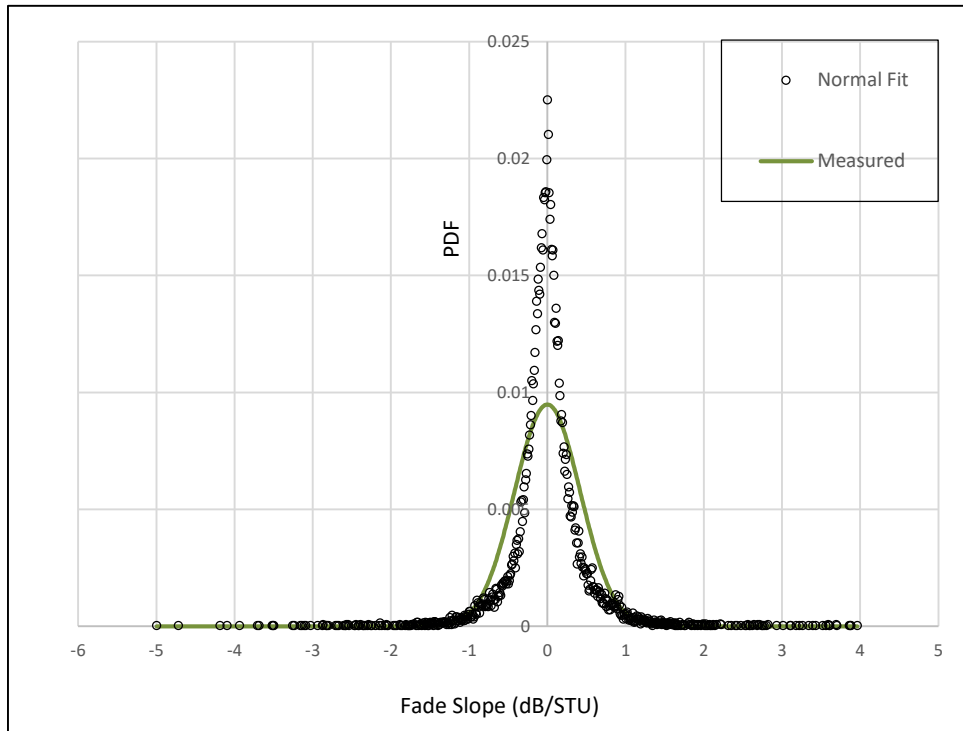


Figure 4-22: PDF of the fade slope of measured attenuation in 2016 in Durban

4.5 Markov-Generated Path Attenuation Time Series

For each year and season, the simulations represented by expressions in equations 4.6 to 4.9 were carried out up to the 5th transition. Each transition represents the PDF of rain attenuation in the following year or season. All resulting PDFs from the will of necessity be lognormal-distributed discrete PDFs since the $I \times k$ matrix is lognormal.

The Markov-generated PDFs were transformed into actual values of the rain attenuation time series they represent using a MATLAB code. Figure 4-23 to 4-27 are a few examples of the attenuation time series generated for the first transition. The results are presented juxtaposed with the time series of the actual rain attenuation measured on the experimental link in those same instants of time. The simulated data can be used for projecting the anticipated performance of a link far beyond the period of measurement at the location and for projecting the effectiveness of fade mitigation schemes well into the future.

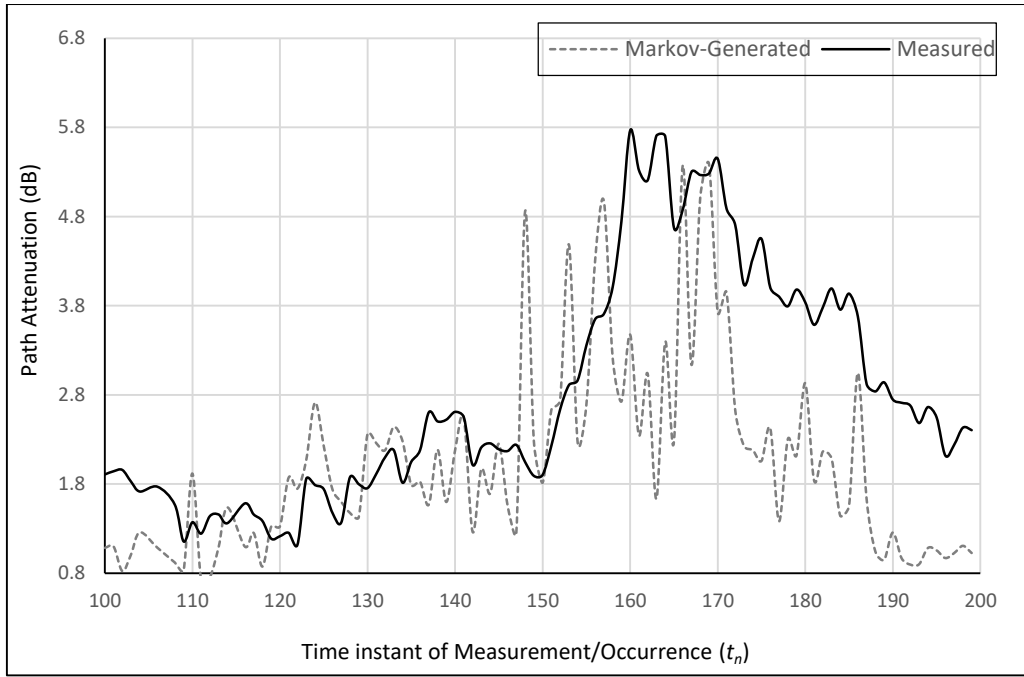


Figure 4-23: Comparison of measured and simulated slant path rain attenuation time series for the 100th to 200th time instant during a subtropical winter season.

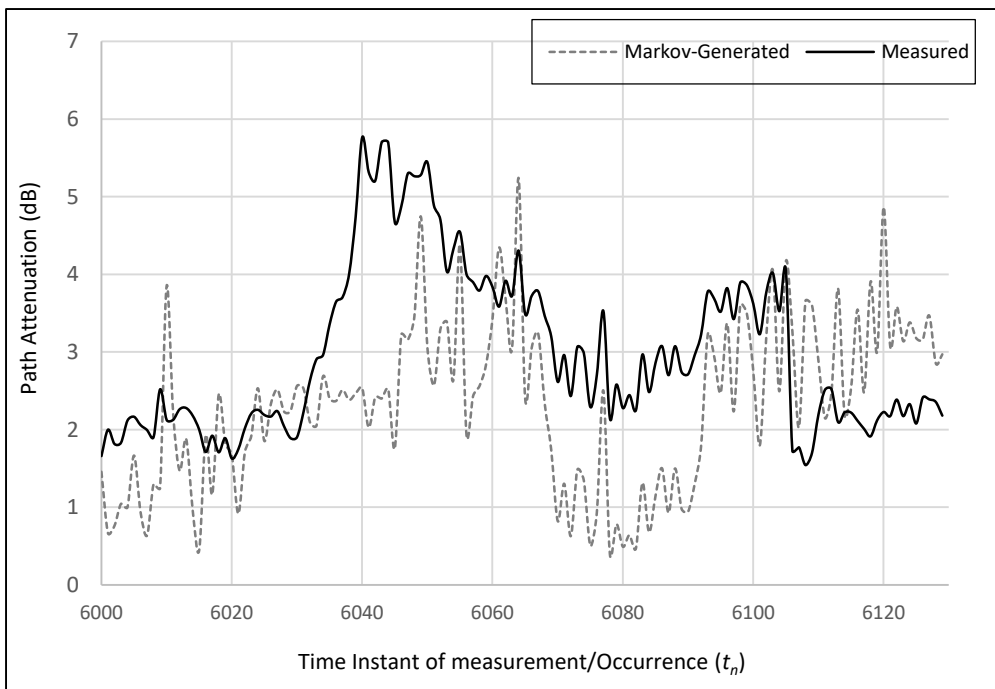


Figure 4-24: Comparison of measured and simulated slant path rain attenuation time series for the 6000th to 6150th time instant in 2013.

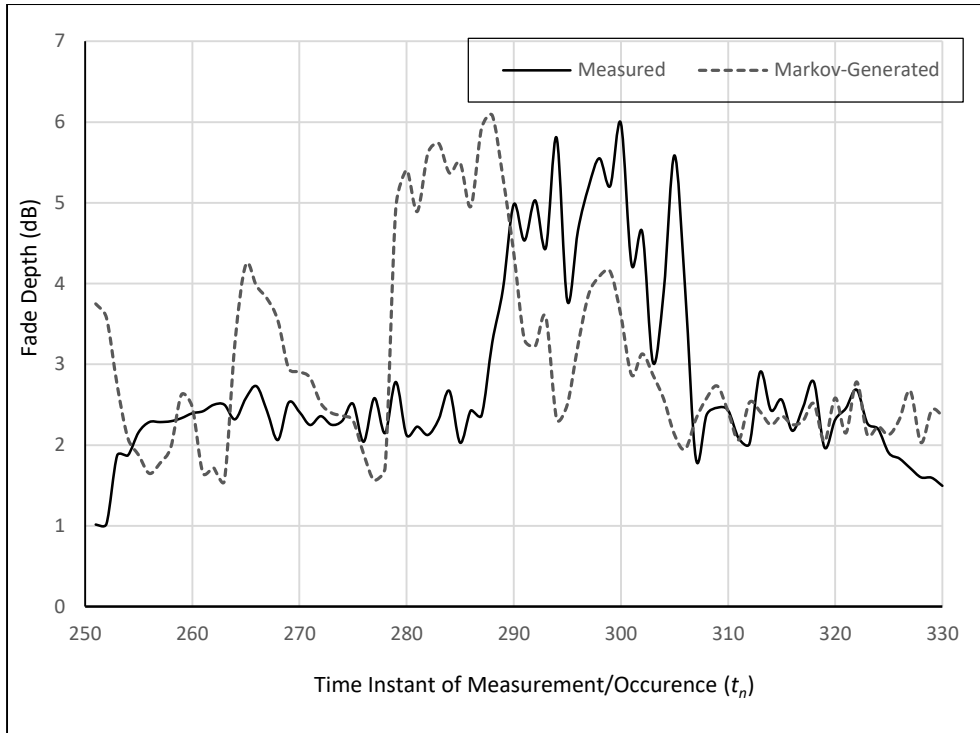


Figure 4-25: Comparison of measured and simulated slant path rain attenuation time series for the 250th to 330th time instant in 2014

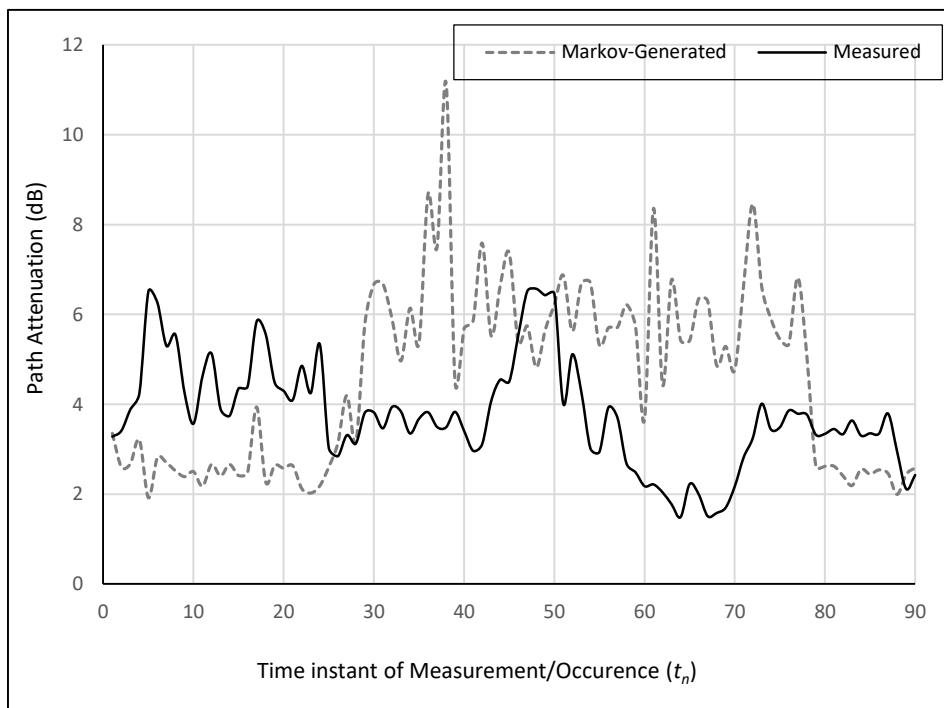


Figure 4-26: Comparison of measured and simulated slant path rain attenuation time series for the 1st to 90th time instant in 2015

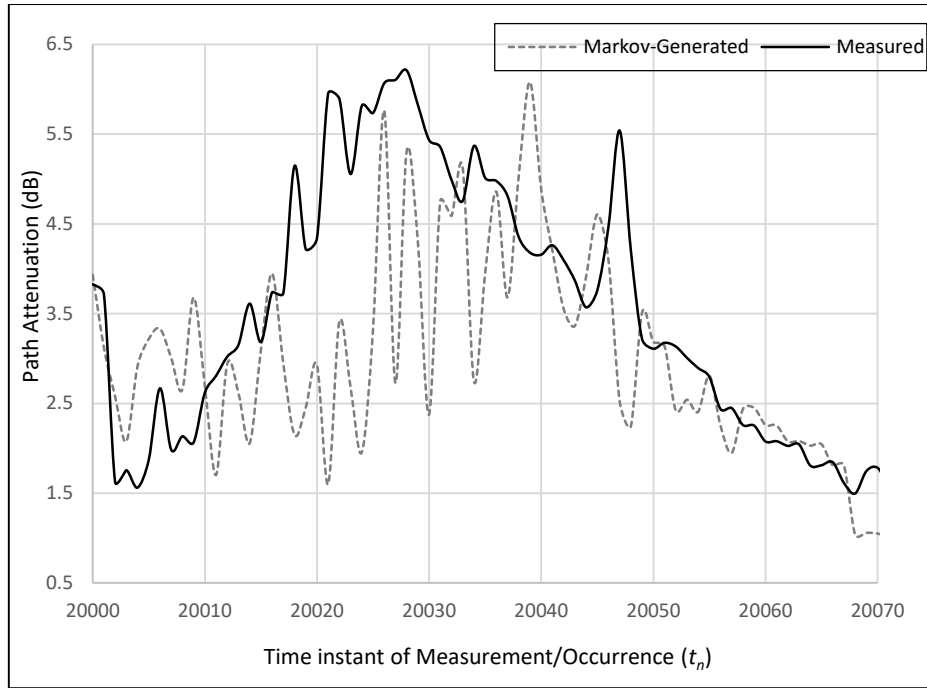


Figure 4-27: Comparison of measured and simulated slant path rain attenuation time series for the 20,000th to 20,070th time instant in 2016

4.6 Exceedance statistics of Markov-Generated slant path attenuation

A useful parameter that is required to be predicted with fairly good accuracy for a planned radio link is the $A_{0.01}$ value, that is the rain attenuation that will be exceeded over it in 0.01% of the year. This follows from the stated goal of designing a link for availability during 99.99% of the year [46], [47]. The rain attenuation statistics predicted in the reported Markov simulations for the first transition, which is the first time period following the period for which measurement data was generated, was statistically analysed to obtain the seasonal and annual exceedance probability at various attenuation levels.

As seen in the figures 4-28 to 4-35, the Markov-generated data exhibits slightly higher values of exceedance probability especially at the low to medium attenuation levels. The probability of exceedance tends to converge in both models as we approach the higher attenuation levels except for the summer season and for the year 2013. In the Table 4-5, we see that $A_{0.01}$ is significantly higher in 2015 and 2016 because both years exhibited a significant increase in rain intensity and duration compared with 2013 and 2014.

Table 4-5: Measured and Markov-Generated $A_{0.01}$ values

Time Period	Attenuation Exceeded at 0.01% of time (dB)	
	Measured (Model)	Markov-Generated
Winter	5.4	5.6
Spring	5.7	5.4
Autumn	5.9	6.5
Summer	6.2	7.3
2013	6.3	6.3
2014	6.4	6.8
2015	8.3	8.7
2016	9.1	10.4

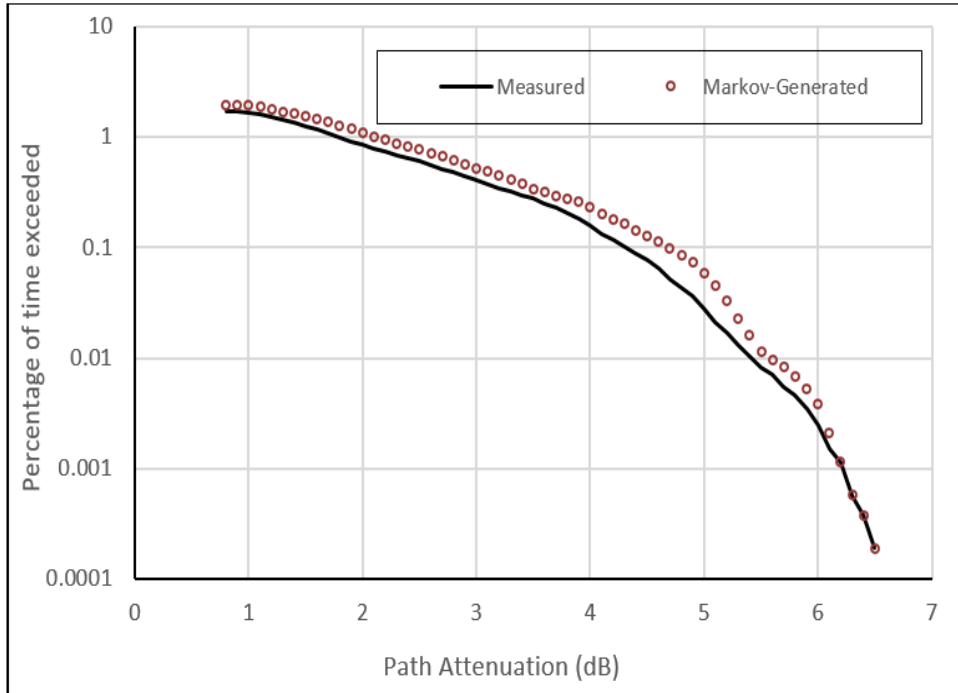


Figure 4-28: Rain attenuation exceedance for measured and Markov-generated statistics in winter

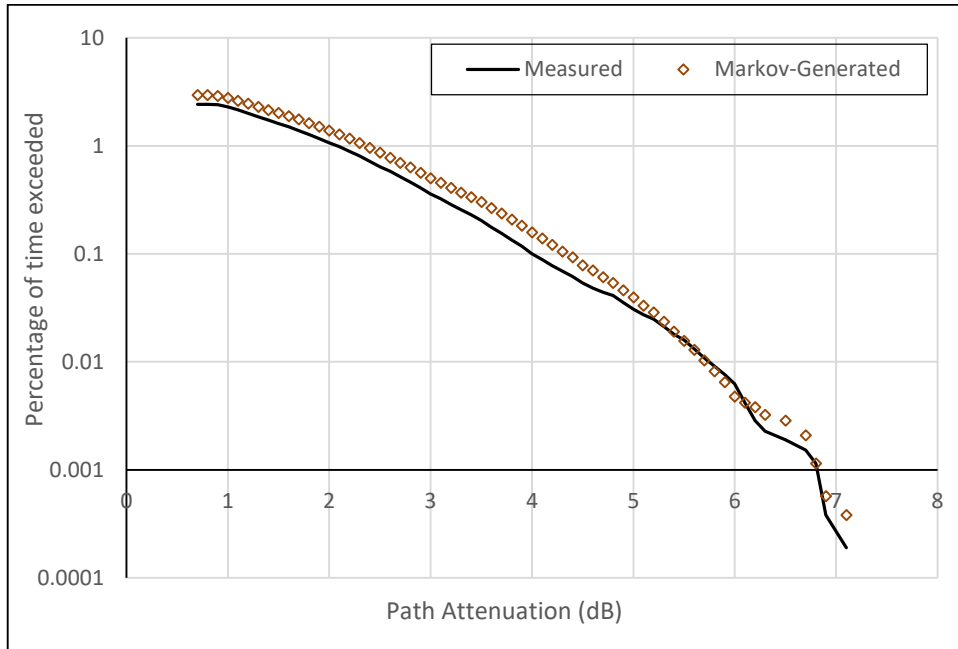


Figure 4-29: Rain attenuation exceedance for measured and Markov-generated statistics in spring

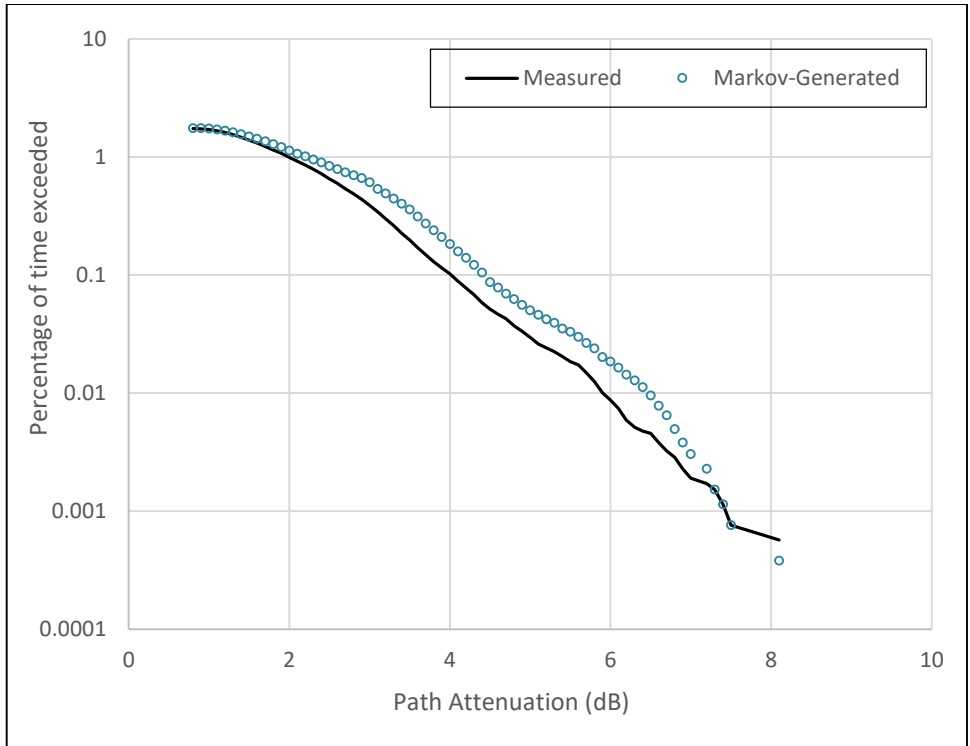


Figure 4-30: Rain attenuation exceedance for measured and Markov-generated statistics in autumn

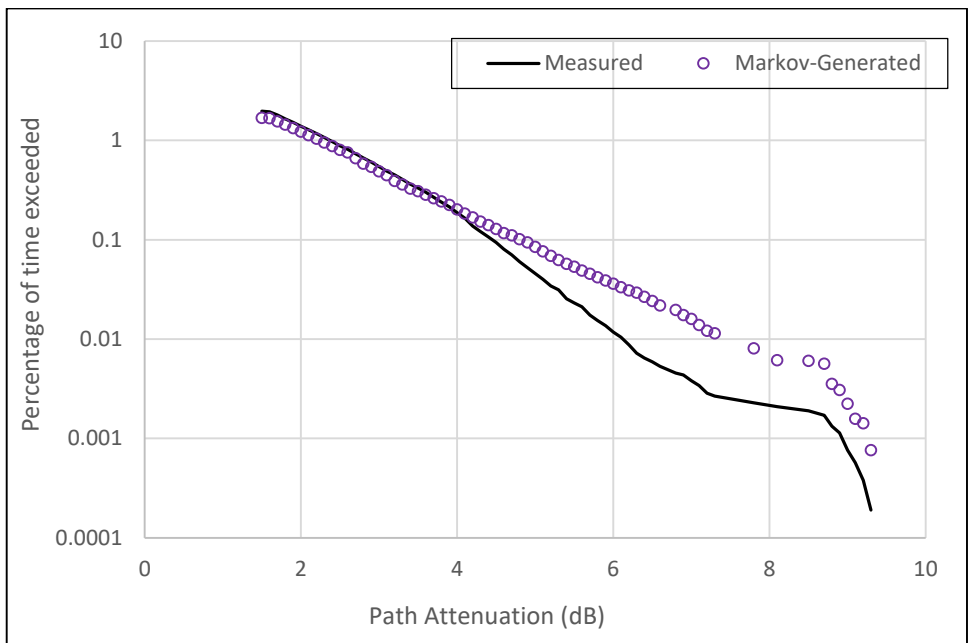


Figure 4-31: Rain attenuation exceedance for measured and Markov-generated statistics in summer

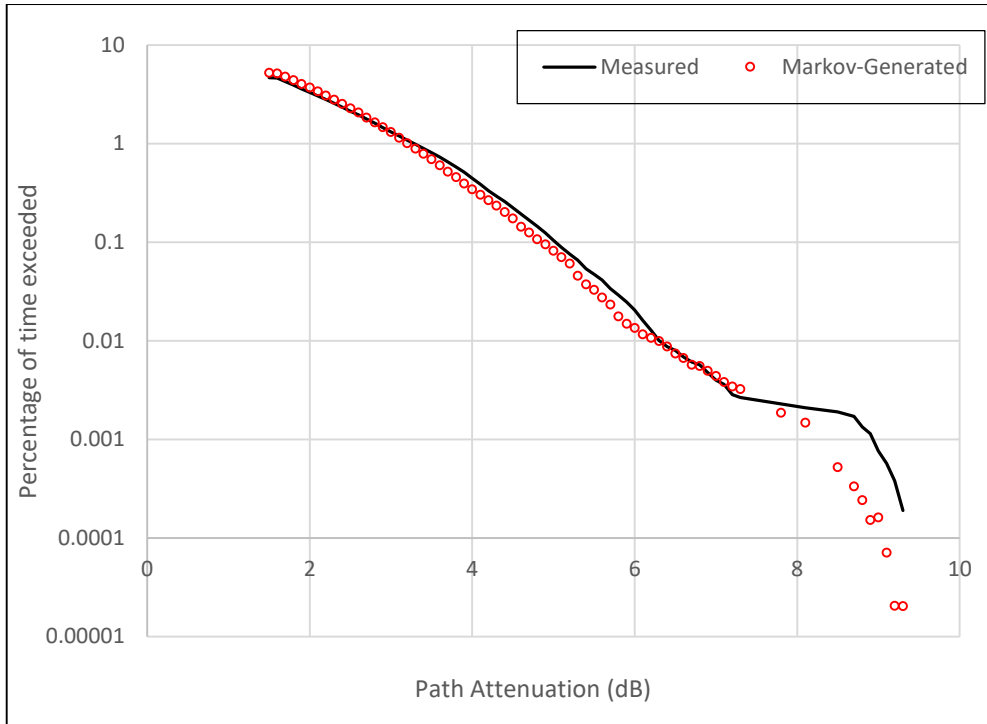


Figure 4-32: Rain attenuation exceedance for measured and Markov-generated statistics for 2013

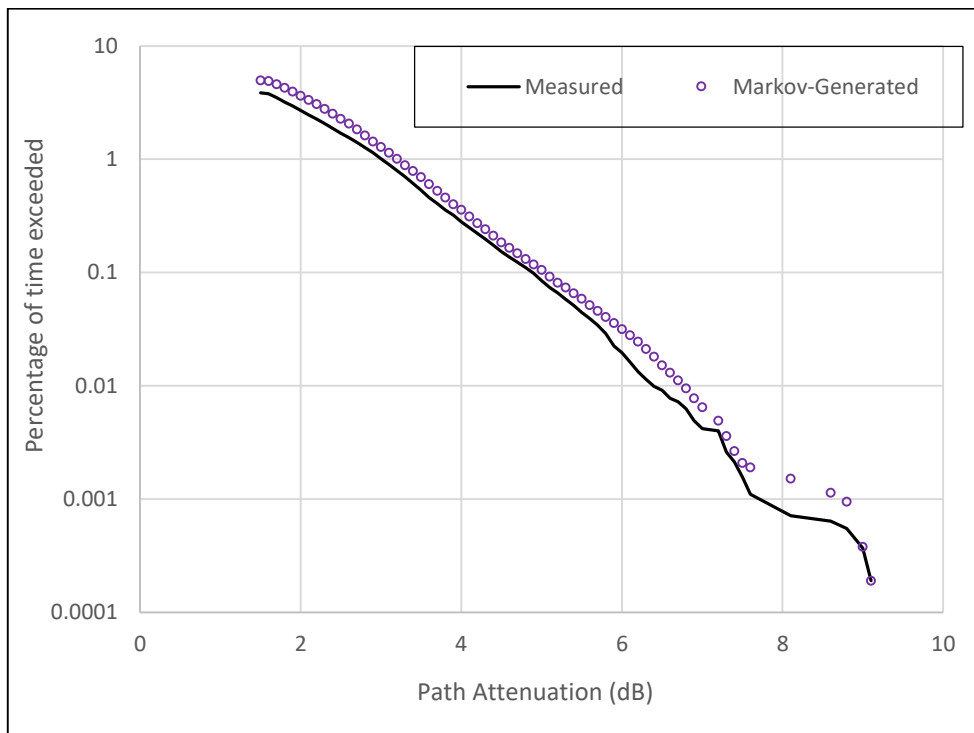


Figure 4-33: Rain attenuation exceedance for measured and Markov-generated statistics in 2014

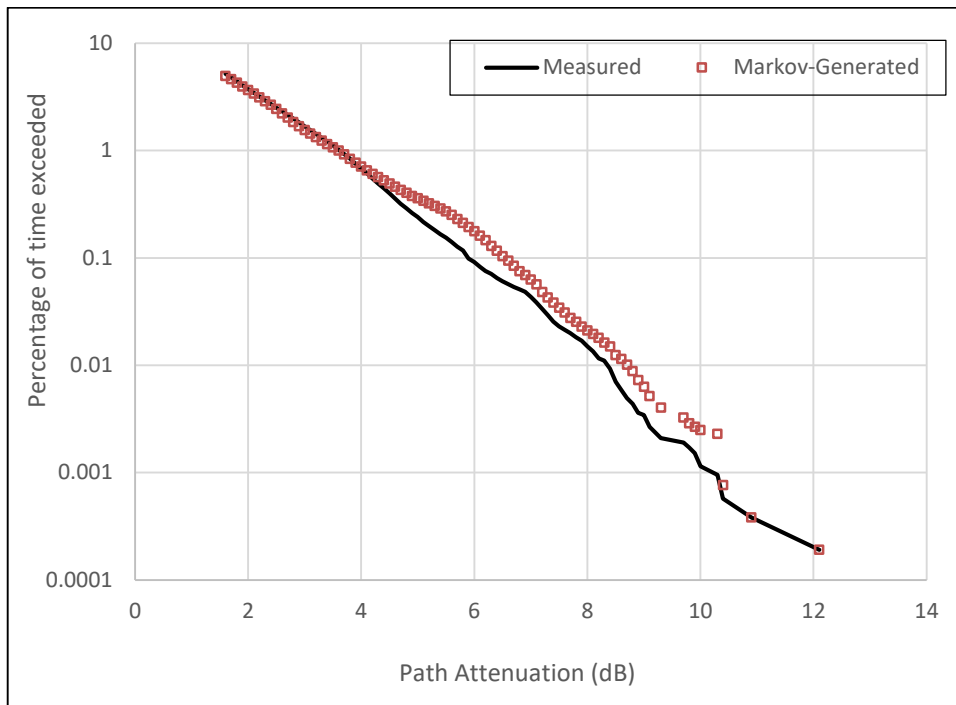


Figure 4-34: Rain attenuation exceedance for measured and Markov-generated statistics in 2015

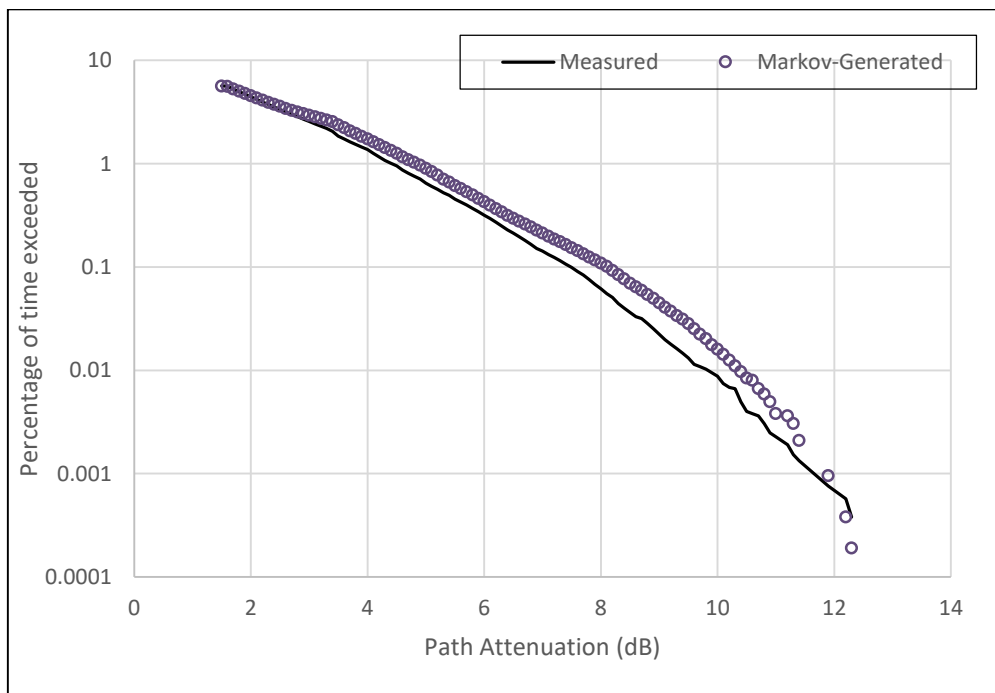


Figure 4-35: Rain attenuation exceedance for measured and Markov-generated statistics in 2016

4.7 Chapter Summary

In this chapter, Markov chain principle was applied to attenuation prediction. The probability density function of measured attenuation for seasonal and annual datasets were obtained. Initial investigations

carried out to reveal that the PDF obeys a lognormal fit. This PDF is later used as the state probability matrix for the Markov chain-generated rain attenuation time series. Seasonal and annual fade slope statistics at the various attenuation levels was calculated. The discrete PDF of the fade slope, fitted to a Gaussian (normal) distribution was also estimated. From the fade slope PDF, each element of the state transition probability matrix of each season and each year from 2013 to 2016 was calculated. Multiple iterations of Markov-generated PDFs representing predictions of future state spaces of seasonal and annual rain attenuation were then used to simulate the attenuation time series. The exceedance probability at various attenuation levels was estimated for the Markov-simulated data and compared with that of the measurement model. $A_{0.01}$ values of both datasets are also compared.

CHAPTER FIVE: SYNTHETIC STORM TECHNIQUE

ANALYSIS OF SLANT PATH ATTENUATION IN

SUBTROPICAL RAIN

5.1 Introduction

The Synthetic Storm Technique (SST) is a useful theoretical approach for estimating attenuation and has been widely applied to both terrestrial and slant path links [102], [103], [104]. The term was originally used in [105] to describe a method by which the rain rate data generated from a rain gauge is used to predict rain rate at a different location by using an estimate of cloud advection speed along the path between the two locations. The concept was then used in [106] to develop a novel mathematical method for estimating rain attenuation from rain rate records.

In this chapter, results of applying the SST approach for long term estimation of rain attenuation on a 12.6 GHz satellite TV link using rain rate statistics amassed over a period of four years from disdrometer measurements at the same location as the satellite link are presented. The rain data has a slightly higher time resolution than usual, being a record of rain rate at every 30 second interval of precipitation throughout the two years. Early applications of this method utilized rain rate data from temperate regions at 1-minute integration time. Also, a measurement-based model for rain attenuation on the link already exists as presented in chapter three.

5.2 Theoretical Framework for the Synthetic Storm Technique

The dynamic nature of rain forms has been explored by various investigators and certain patterns established. [105] showed that as a rain form passes over the rain gauge, advection speed and the rain rate data can be used to convert the time it takes to pass over the rain gauge to distance. A fairly good reckoning of the rain rate distribution pattern over the distance can then be deduced. In [107], the authors also showed that over distances comparable to the length of most earth-satellite paths, there's a marked statistical consistency in rain rate patterns as the rain form spans the distance. Drawing from these, [108] provided evidence that if the storm motion roughly aligns with the radio path, rain attenuation obtained from the synthetic path will agree with actual attenuation values. The SST was tested in several earlier works using radar-derived values of storm speed that averaged about 10 m/s [109], [110], [111].

SST adopts a dual-layer model of the vertical profile of rain. From the ground to the zero-degree isotherm is labelled the "A" layer. This layer consists entirely of liquid precipitation and the rain rate R in this layer is taken as the same as the rain rate measured by the equipment on the ground. Above layer A lies layer B, which is essentially the melting layer, made up of both liquid hydrometeors and ice in melting form. While layer A approaches up to 6 km, layer B is often estimated as lower than 0.5 km. In [106], it was shown that the rain rate R_B in the layer B, (called the apparent rain rate) is related to R as

$$R_B = 3.134R \quad (5.1)$$

[106] employed an old ITU-R method for estimating the rain height. According to the recommendation, rain height at the layer B in figure 5-1 for any location at a latitude above 23° as is the case with our link is given by [112]

$$H_B = 5 - 0.075(\varphi - 23) \quad (km) \quad (5.2)$$

The thickness of layer B, h is taken as 0.4 km, hence the height H_A is thus given by

$$H_A(\varphi) = H_B(\varphi) - h \quad (km) \quad (5.3)$$

For this work, the in-force ITU-R model for rain height [69] was adopted, which allots a value of 0.36 km to melting layer depth and hence estimates H_B as

$$H_B = h_0 + 0.36 \quad (km) \quad (5.4)$$

where h_0 is the height of the zero-degree isotherm and is equivalent to H_A and 0.36 is the melting layer depth in kilometres. The value of h_0 can be read for location from a map provided by the ITU-R recommendation [69].

The lengths L_A and L_B of the slant path up to the top of each layer are given by [69]

$$L_A = (H_A - H_S)/\sin \theta \quad (5.5)$$

$$\text{and} \quad L_B = (H_B - H_S)/\sin \theta \quad (5.6)$$

where θ is the elevation angle and H_S is the height of receiving antenna above sea level.

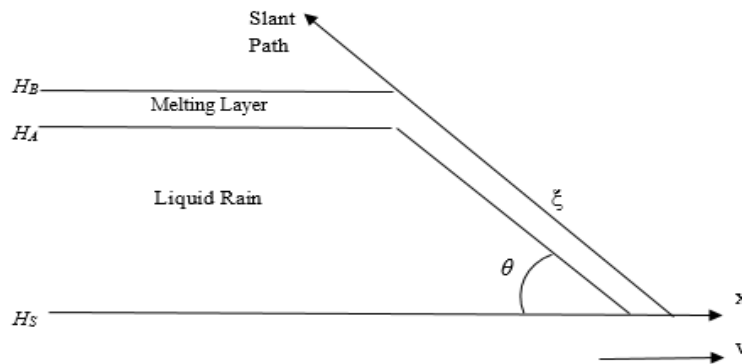


Figure 5-1: Two-layer vertical profile of rain for the Synthetic Storm Technique

Applying the power law expression of [65] which gives the specific attenuation γ at x on the x -axis as

$$\gamma(x) = kR^\alpha(x) \quad (5.7)$$

where k and α are frequency-dependent parameters for water at temperature 0°C obtained by [113] and [114]. The values of k and α for water at 20°C are also presented in [86], which makes it possible for us to estimate γ for layer B. γ is defined as the attenuation per kilometre, hence, the attenuation along a path of length L km can be estimated by the integral

$$A(x_0) = \int_{x_0-L/2}^{x_0+L/2} R^\alpha(x) dx \quad (5.8)$$

The fundamental idea behind the SST is that if there is a reliable level of isotropy of the rain medium at each layer, then the variation of attenuation with time is simulated by varying the point x_0 at a time rate that equals the storm speed v such that $x_0 = vt$.

According to [106], if θ elevation angle and ξ is the slant path ordinate, then total signal attenuation in case of satellite path is obtained from specific attenuation at a point as the sum of attenuation in both layers given by summing the integrals in equation (5.9) for each layer (r being the ratio 3.134 of rain rate in both layers) such that [106],

$$A(x_0) = K_A \int_0^{L_A} R^{\alpha_A}(x_0 + \Delta x_0, \xi) d\xi + K_B r^{\alpha_B} \int_{L_A}^{L_B} R^{\alpha_B}(x_0, \xi) d\xi \quad (5.9)$$

Equation (5-9) has the basic form of a rectangular function with width L centred at the origin such that

$$A = k \int_{-\infty}^{\infty} R^\alpha(x_0 + x) \text{rect}(x/L) dx \quad (5.10)$$

A Fourier transform of the above will be

$$S_A(f_s) = S_Y(f_s) L \text{sinc}(f_s L) \quad (5.11)$$

where $S_A(f_s) = \mathfrak{F}\{A(x_0)\}$, $S_Y(f_s) = \mathfrak{F}\{kR^\alpha(x)\}$ and $\text{sinc}(f_s L) = \sin(\pi f_s L)/(\pi f_s L)$

Applying these transforms to equation (5.9), we have

$$S_A(f_s) = S_{Y,A}(f_s) L_A \text{sinc}(f_s L_A) \exp(-j2\pi f_s \Delta x_0) + r^{\alpha_B} S_{Y,B}(f_s) \Delta L \text{sinc}(f_s \Delta L) \quad (5.12)$$

where $S_{Y,A}(f_s) = \mathfrak{F}\{k_A R^{\alpha_A}(x)\}$,

$$S_{Y,A}(f_s) = \mathfrak{F}\{k_A R^{\alpha_A}(x)\}$$

and $S_{Y,B}(f_s) = \mathfrak{F}\{k_B R^{\alpha_B}(x)\}$

Using the transformation $f = \frac{vf_s}{\cos \theta}$ and $v(\theta) = v / \cos \theta$ in equation (5.10) yields

$$S_A(f_s) = S_{Y,A}(f) L_A \text{sinc}(fL_A/v(\theta)) \exp(-j2\pi f \Delta x_0/v(\theta)) + r^{\alpha_B} S_{Y,B}(f) \Delta L \text{sinc}(f\Delta L/v(\theta)) \quad (5.13)$$

If, as is the case for the link $\theta \neq 90$, and $v \rightarrow \infty$, transforming equation (5.12) back to the time domain, the expression becomes

$$\lim_{v \rightarrow \infty} A(t) = k_A R^{\alpha_A}(t) L_A + r^{\alpha_B} k_B R^{\alpha_B}(t) (L_B - L_A) \quad (5.14)$$

The resulting limit in equation (5.12) implies that the long term application of the SST for estimating attenuation is insensitive to storm speed v [106]. Hence, a reliable estimate of $A(t)$ using a known, long term, measured rain rate time series $R(t)$ as the sole time-varying input can be arrived at.

5.3 Input Parameters and Link Statistics

With reference to the results outlined in chapter 3, 14 months of continuous measurement on a 12.6 GHz satellite TV link in Durban gave an empirical model of slant path attenuation whose average bound is given by

$$A_{ave} = 1.338R^{0.5482}(\text{dB}) \quad (5.15)$$

The average band was selected for comparison to SST results since SST itself is in principle a form of averaging. Details of the link's parameters are presented in Table 3-2. The expression in (5.15) was shown to bear exact conformance to actual measurement 89.9% of the time, having a coefficient of variation of 0.899. This makes it a near-perfect representation of measured data. The comparisons of actual attenuation patterns drawn in this chapter with SST results shall be based on equation (5.15) above. The table 5-1 presents the link parameters adopted for the SST calculations.

5.4 Attenuation Prediction by SST for some Rain Events

Using a storm speed of 9.41 ms^{-1} as averaged for Durban by a method due to [115], the results of the synthetic storm technique for Durban during a few significant rain events from 2013 to 2016 are presented in the Figures 5-2 to 5-7 along with the rain attenuation measured on the 12.6 GHz link during the rain event.

Table 5-1: Input parameters used for the 2-layer vertical rain profile

Parameter	Layer A	Layer B
k	0.02421	0.0168
α	1.1516	1.26
H	4.6 km	4.96 km
L	7.43778 km	8.043 km
<i>Elevation Angle</i>	36.5°	

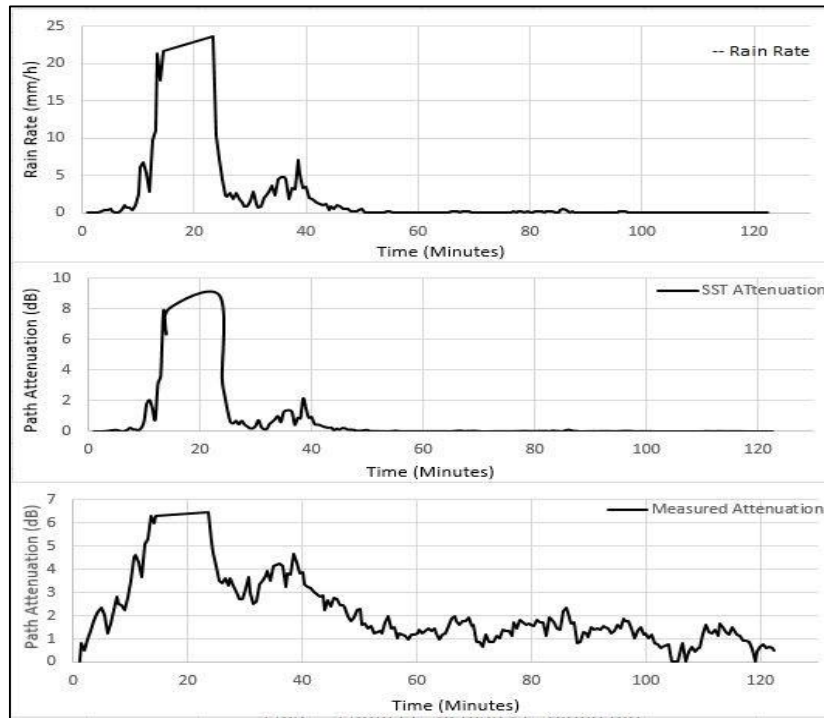


Figure 5-2: SST and measured attenuation for rain event on 6th of May 2016

From equation 5.9, SST attenuation can be described more accurately as a long term summation of the rain attenuation experienced on the link over an extended period of time. Therefore, event-specific snapshots aggregated at one storm speed may not be as accurate as the long-term data. Moreover, SST estimates tend to ignore the less significant fade instances brought about by low rain rate such as attenuation levels of 3 dB and below. In most of these instances, where the measured attenuation is 3 dB and below, SST often reflects a flat fade level, only registering a spike when the measured value shoots significantly above that threshold. Being essentially a summation of power law elements, the effect of layer B attenuation is slightly muted at low values of rain rate.

About the average rain rates, SST results generally agree with measured values. At the peak rain rates, it slightly overestimates the attenuation level but still gives a very good approximation. The attenuation predicted in the second layer is most pronounced in its effect on total path attenuation at the peak rain rates.

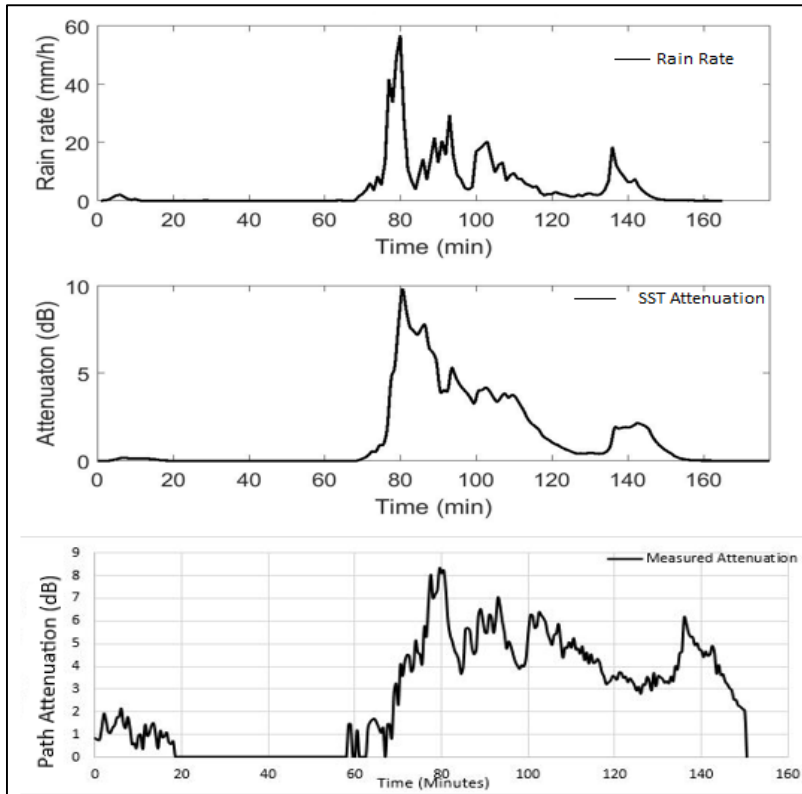


Figure 5-3: SST and measured attenuation for rain event on 6th of February 2015

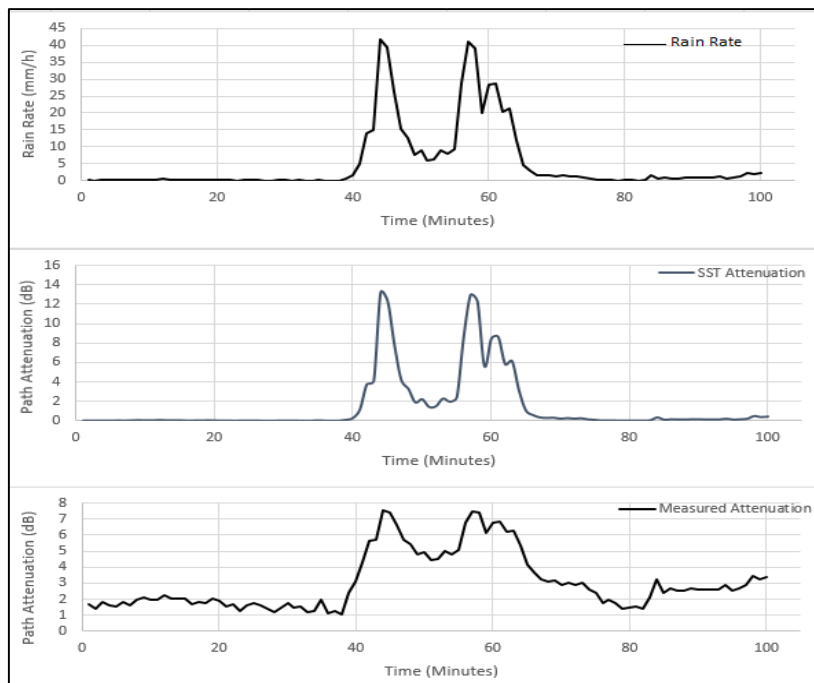


Figure 5-4: SST and measured attenuation for rain event on 4th of November 2014

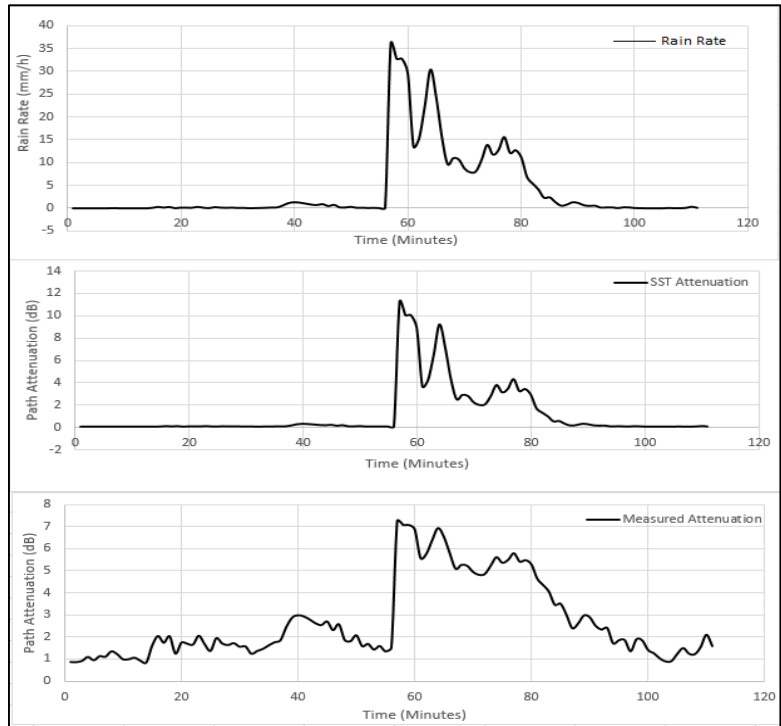


Figure 5-5: SST and measured attenuation for rain event on 3rd of December 2013

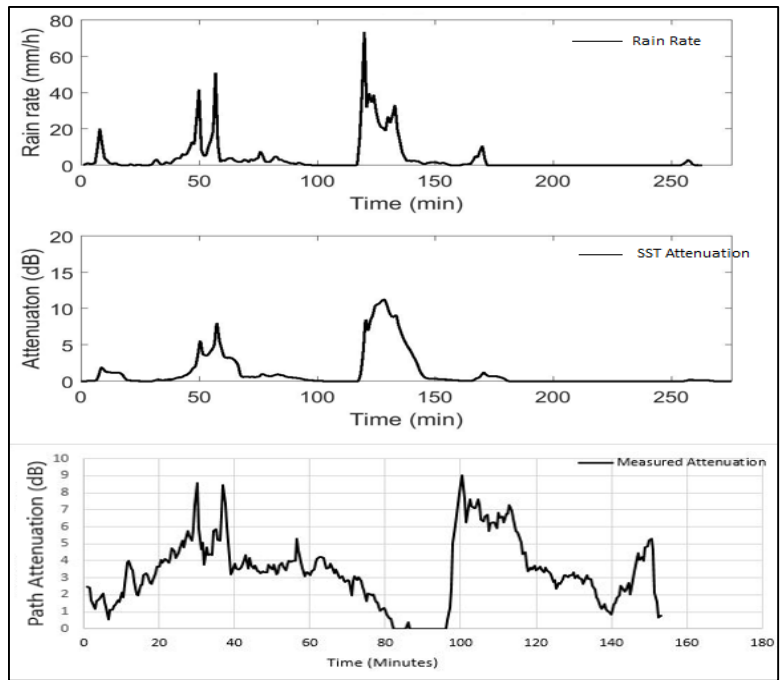


Figure 5-6: SST and measured attenuation for rain event on 1st of March 2015

5.5 Annual SST Attenuation Results

The conformity of SST to the measurement model is best illustrated by the comparison between the annual attenuation exceedance trends as presented in Figures 5-7 to 5-10 for the years 2013 to 2016. Depending on the rain pattern, the exceedance probability of the SST model and the measurement model is observed to largely fall in the same range, even reaching a point of convergence for 2015.

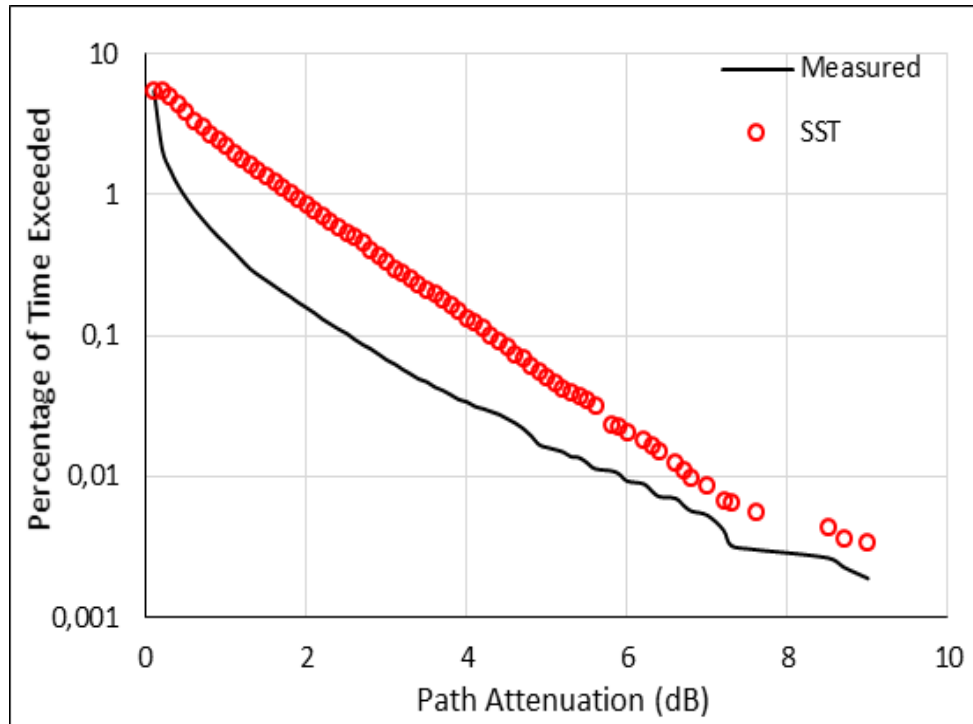


Figure 5-7: Comparison of SST attenuation exceedance probability with measurement 2013

The pattern of the annual exceedance probability curves are highly influenced by the rain pattern in the particular year it represents. This is quite obvious from the figures. The years 2013 and 2014, were essentially years of drought in much of the south eastern region of South Africa. The low rainfall in these two years compared to 2015 and 2016 is the reason for the variation in the annual exceedance patterns. This observation also confirms that SST prediction is sensitive to rainfall pattern over time and hence to climate and location.

Communication links are designed for 99.99% annual availability. That is, the fade margin allowed must not be greater the attenuation exceeded at 0.01% ($A_{0.01}$) of the year (or 87.6 hours) [1]. Table 5-2 compares $A_{0.01}$ as obtained from measurement and from SST prediction. The results agree more in 2013 and 2014 than in 2015 and 2016. Overall, SST appears to be a useful estimate of the attenuation exceeded.

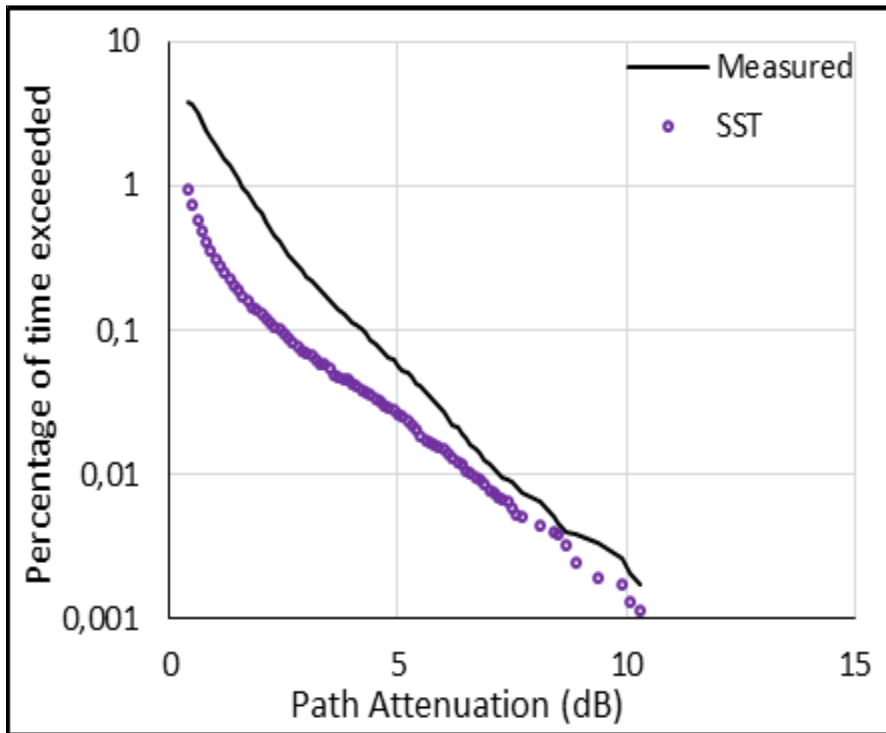


Figure 5-8: Comparison of SST attenuation exceedance probability with measurement 2014

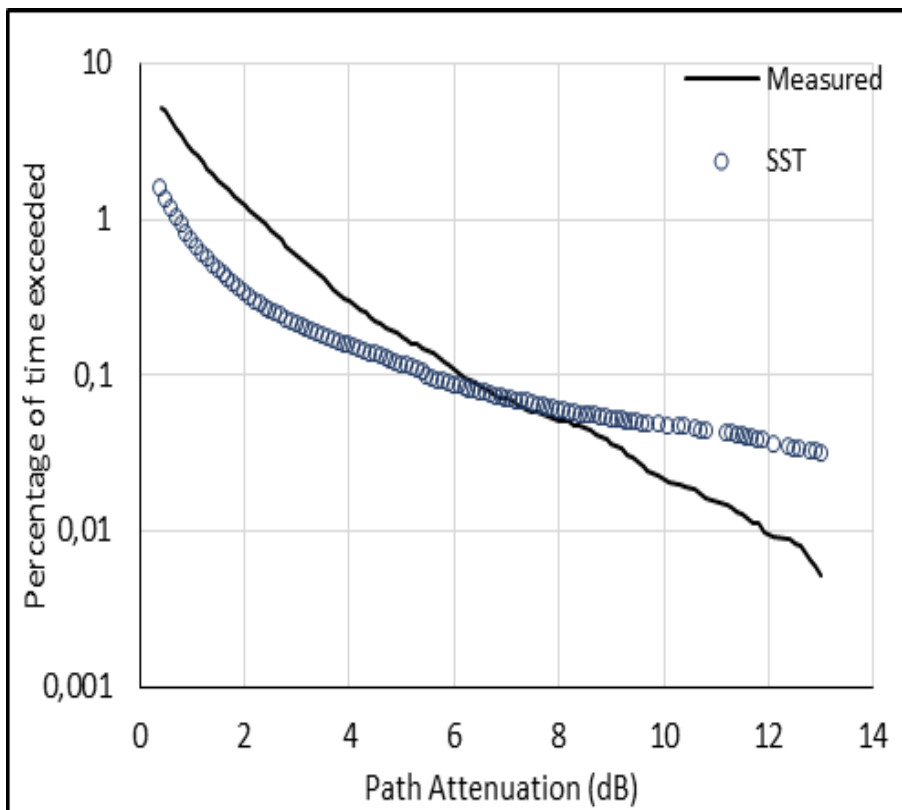


Figure 5-9: Comparison of SST attenuation exceedance probability with measurement 2015

Table 5-2: Path attenuation at various exceedance probabilities for both models

Year	$A_{0.001}$ (dB)	
	Measured	SST
2013	6	6.8
2014	7.3	6.6
2015	11.9	15.6
2016	13.8	12.2

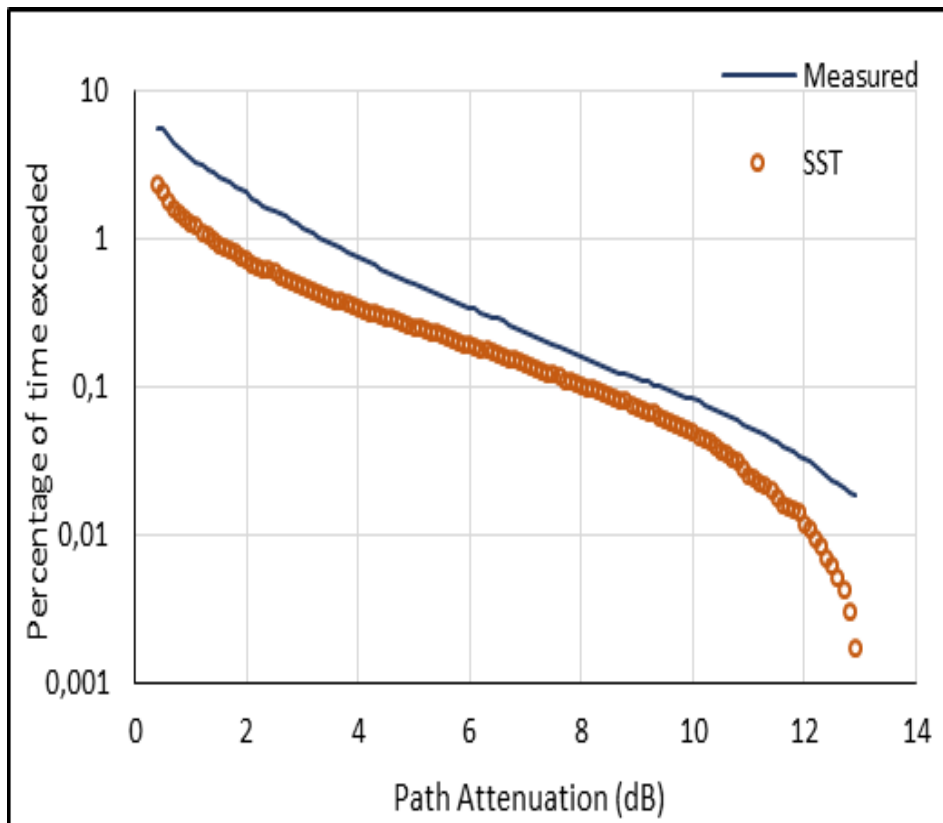


Figure 5-10: Comparison of SST attenuation exceedance probability with measurement 2016

5.6 Performance of SST Compared with the ITU-R Prediction

The Figure 5-11 is a direct comparison of SST, measurement and the in-force ITU-R model [8] for the 0 to 40 mm/h rain rate range. This range is chosen because it is the rain rate range in which the measurement link attains attenuation in the range of 0 to about 10.7 dB before squelching occurs.

A more general gauge of the relevance of SST as a useful theoretical tool for rain attenuation prediction in the subtropics can be obtained through error analysis which holds the measured data as the expected value and the SST as the observed value. Both the Chi-square test and root-mean-square error are estimated as in the equations (5-16) and (5-17). In equation (5-16), p_i is the SST value of attenuation at

a certain rain rate while a_i is the value from the measured model at the same rain rate. For equation (5-17), setting O_i the observed value as the SST value of attenuation and E_i the expected value as the value obtained from the measurement model.

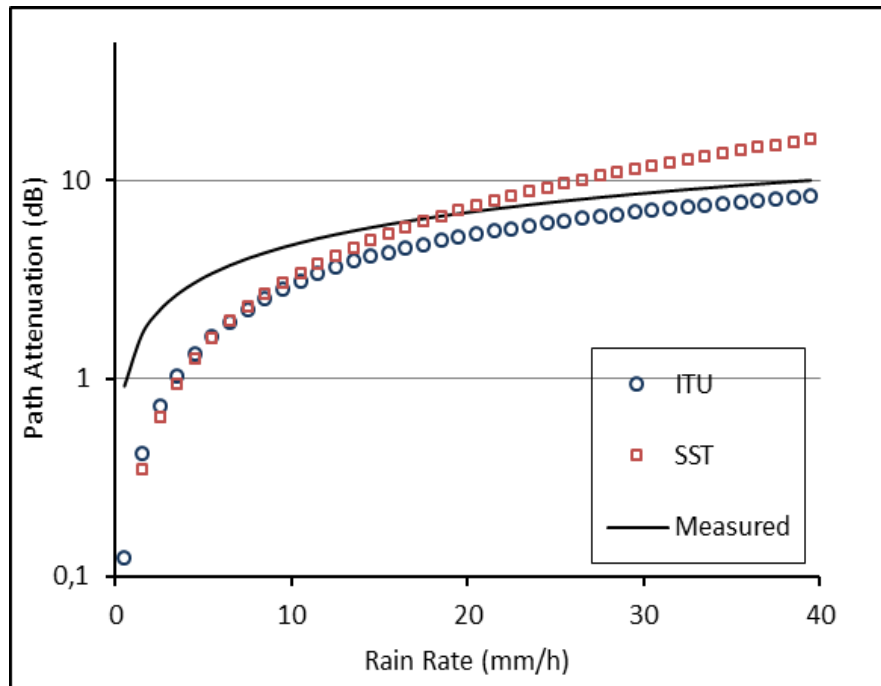


Figure 5-11: Comparison of the models at 1 to 40 mm/h

The RMSE error is a basic test of the deviation between an observed value and an estimated value. Chi-Square Test is a slightly more sophisticated statistical test of hypothesis where the Chi-Square distribution is obeyed when the null hypothesis holds true. Picking a convenient confidence level, we estimate the Chi-Square parameter between our observed value and the estimated value. The sample population forms our number of degrees of freedom. The Chi-Square value ought to lie well below the critical value on the Chi-Square distribution table for that particular set of parameters, i.e. confidence level and degrees of freedom. When this is the case, we say the null hypothesis is accepted as true, which implies that the statistical difference between the observed and the estimated values is not significant.

The Table 5-3 shows the results of the error analysis. The RMS error in SST is slightly higher than that of the ITU-R method but at 2.42, is still an acceptable margin of error. The Chi-Square test also shows that the SST has a Chi-Square value of 38.13 as against 19.76 for the ITU-R model. Both fall well below the critical value of 163.051 but the ITU-R is clearly a more acceptable hypothetical approach. It shows that the ITU-R model performs better as a prediction model than the SST model for this link but it can still be considered a very useful method in the rain fade prediction process since it does not vary too far from observed levels in this critical range of rain rates.

$$RMSE = \sqrt{\frac{\sum_{i=1}^n (p_i - a_i)^2}{n}} \quad (5.16)$$

$$\chi^2 = \sum \frac{(O_i - E_i)^2}{E_i} \quad (5.17)$$

Table 5-3: Error analysis of SST and ITU-R model using measurement figures as the expected value.

Model	RMSE	χ^2 Value		χ^2 test result
		Actual	Critical	
SST	2.42	38.13	163.051	Accept
ITU-R	1.47	19.76	163.051	Accept

The performance of the SST on Ku band satellite link using rainfall data from a subtropical location gives a strong indication that the SST is a reliable method for theoretical prediction of rain attenuation on slant paths. The efficacy of this method is well-documented for temperate regions [102], [103], [104] in a few cases for tropical regions [116], [18] and fewer still for the subtropics [117], [118].

5.7 Chapter Summary

This chapter discusses the theory of synthetic storm technique of rain attenuation estimation for a slant path and applies it to rain events on the experimental microwave link discussed in chapter 3. Cumulative distribution functions of the attenuation statistics by SST and by measurement are presented and compared. Close agreement between measured data and SST is demonstrated to occur at or near the $A_{0.01}$ point for each of the years estimated. Statistical comparison between the ITU-R theoretical model and SST model was carried out and presented and, shows that ITU-R appears to represent a slightly closer estimate to measured data than the SST model for the location.

CHAPTER 6: ESTIMATION OF RAIN HEIGHT FROM ATTENUATION-PRECIPITATION TIME DELAY DATA

6.1 Introduction

This chapter is a short chapter that presents a novel analysis done as an attempt to explain one of the observations made in the course of the measurement campaign reported in chapter 3. Possible explanations are explored and proposed for the physical implications of a phenomenon that is often observed during rain attenuation measurements and which may be more pronounced over slant paths of several kilometres but has so far not received an empirical explanation.

It is well-established that there is a direct relationship between rainfall and attenuation on a communication link especially at low wavelengths that compare favourably with rain drop size (about 3mm and higher or 10 GHz). This is an effect that is known to occur in a cause-effect dynamic such that the cause is expected to precede the effect in the time domain. Observations have shown however, that during certain precipitation events, a significant amount of time, running into several minutes passes between the occurrence of signal impairment and actual precipitation. This phenomenon is easily established because not only is a significant drop in RSL level registered by the spectrum analyser, the TV reception quality can be seen to be impaired (by monitoring the visual display unit connected to the receiver) several minutes *before* actual precipitation begins at the location. This is a phenomenon that has hitherto gone without much empirical interpretation.

While logical deductions can be made *a priori* (from cause to effect) or *a posteriori* (from effect to cause), the expected order of physical events is that the cause occurs (and is observed in the time domain) *before* the effect is observed. Rain being the cause and attenuation the effect, a time lapse between the two is understandable if precipitation occurs first. Such a time lapse can be attributed to equipment/system response time and/or other causes of no unique significance. Having these events occur in the reverse order requires further investigation especially when the time runs into several minutes.

6.2 Dynamics of the interaction between the Rain System and the Slant Path

The satellite beacon is beamed to Durban at ground elevation angle 36.5° from the geostationary IS-20 communication satellite which is located due east over the Indian Ocean on 69°E . Rain attenuation on a slant path will occur any time the rain medium interacts with the satellite beacon either at the location of the receive antenna or elsewhere on the slant path. Depending on the direction of migration of the rain cell relative to the location of the receive antenna, the smaller rain cells can on rare occasions interact with the signal path at a certain time and place, causing attenuation without necessarily dropping any actual precipitation at the receive antenna.

The interaction between a migrating rain cell and an earth-satellite communication link can occur in a number of configurations. While much planning and calculations go into locating the receiving antenna and the geostationary communication satellite [77], the position and direction of migration of the rain cell is completely random. It is governed by a wide variety of climactic factors, chiefly the principal ocean current(s) responsible for rainfall events at the receiver location [119]. The current(s) bring water-laden clouds from offshore to land where they release their moisture as rainfall. Durban is located on the coast of the Indian Ocean. Rain and other climatic indices in much of the eastern half of South Africa are governed primarily by two warm ocean currents – the Agulhas Current on the south-eastern coast and the Mozambique Current on the eastern coast. The Benguela current on the western coast is a cold current [120]. This configuration dictates that many rain events in Durban are from moisture-laden cloud migrating from directions due east and south of Durban.

The most useful configuration of these events during measurement campaigns is the one that allows us to do a direct correlation of a specific rain rate time series with the specific attenuation event caused by it. Two scenarios tend to emerge from these measurement campaigns:

1. The equipment registers a drop in RSL sometime AFTER precipitation is registered at the receive antenna, or
2. The equipment registers a drop in RSL BEFORE precipitation is registered at the receive antenna.

The latter is the scenario in which the effect appears to precede the cause in the time domain, which is not natural. This is the scenario for which we apply the term “attenuation-precipitation time delay event”.

Apparently, a widely varying number of scenarios is possible but a simplified example of a delay event is one in which the rain cell approaches the antenna location from the east and encounters the signal path some minutes before reaching the measurement location. In this case, it is to be expected that a significant attenuation of the signal can possibly be registered by the spectrum analyser *before* precipitation is registered by the disdrometer - especially if the event features fairly high rain spikes and large drop sizes. We assume this to be the most probable root cause of the time delay. We thus postulate that the time delay observed is the time it takes the edge of the rain cell to migrate from the point of interaction with the slant path to the point directly above the receiver location.



Figure 6-1: Rain formation in Durban and its interaction with the slant path of satellite beacon

6.3 Extraction of the Time Delay Statistics

A crucial feature that appears to be common to all the time delay events in this study also in part provides proof of the reliability of the explanation proposed above. This is the unmistakable regularity observed between the time series of the rain spikes and the time series of the RSL data. Even though a significant time lapse lies between both measurements, the regularity confirms that the attenuation pattern (represented by the troughs) seen in the RSL time series was caused by the particular spikes seen in the rain event.

The significance of such an event is dependent on the amount of time that passes between the time at which RSL level drops significantly and the time at which precipitation is registered on the ground at the receive antenna. A delay of several seconds would not qualify as a time delay event as it could well be due to delay in equipment response. Delays that last several minutes are the ones of interest. In this study, the minimum time that establishes such an event has been set at a convenient threshold of 4 minutes. The choice of 4 minutes is based on inspection of data extracted from the link. Of the many dozens of events examined, delays of 4 minutes and higher are much fewer while delays of less than 4 minutes appear to be commonplace. Also, the distance that the rain cell will cover in 4 minutes at the mean cloud advection speed of 9.41 ms^{-1} estimated for Durban [115] will be approximately 2.26 km, which appears to be a more appreciable distance to justify the subsequent analysis.

The 31 events selected for the analysis were picked based on the amount of time between the occurrence of the first major dip in RSL level and the first major rain spike that can be matched to that signal drop. Details of how this matching was done are discussed in chapter 3. Detail parameters of these events are presented in Table 6-1. The data shows that there is no correlation between the rain type and the level of delay observed, demonstrating that the delay is entirely a product of the random nature of rainfall.

Table 6-1: Time lapse events

Serial Number	Delay (Minutes)	Peak Rain Rate (mm/h)
1	15	4.404
2	7	2.336
3	14	2.915
4	7.5	18.324
5	6	1.593
6	7.7	1.846
7	7	2.5
8	14.8	16.024
9	13	5.123
10	5.8	15.996
11	5	87.73
12	7.5	1.481
13	15.5	11.561
14	5	19.181
15	4.6	6.0671
16	4	13.254
17	6	38.059
18	7	17.862
19	5.3	23.689
20	4.9	5.599
21	9.6	28.504
22	5.4	10.357
23	10.5	11.758
24	4.6	3.045
25	5	33.059
26	11.5	17.862
27	7.5	4.112
28	6.5	18.621
29	8.5	6.055
30	5.9	2.544
31	10.7	11.211

6.4 Relationship of Time Delay with Rain Height

The Figure 6-2 presents a plane geometry rendering of a time delay scenario. The point A is the point at which the rain cell first encounters the satellite beacon, B is the point above the receive antenna where precipitation is registered later and C position of the receive antenna as well as the disdrometer. The rain cell is expected to have covered a distance d_{cell} km during the observed time of delay. However, a rendering that may be more true to reality is given in the Figure 6-3 by considering all the relevant points in spherical coordinates.

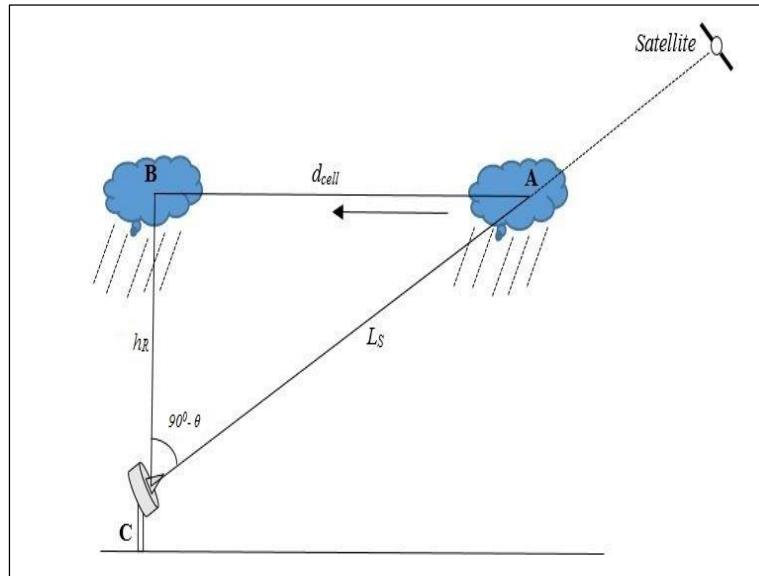


Figure 6-2: Illustration of a time delay event.

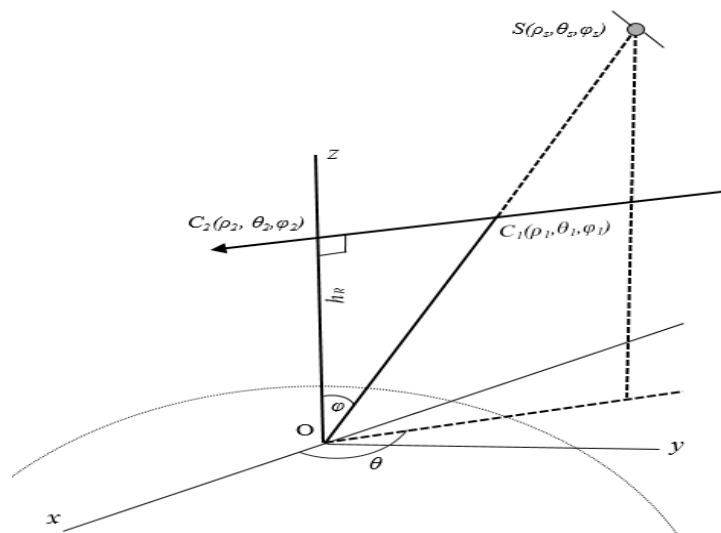


Figure 6-3: Illustration of a time delay event.

The position of the geostationary satellite will be the point $S(\rho_s, \theta_s, \varphi_s)$, where ρ_s is the total path of the link. θ_s is related to the azimuth angle α_s of the satellite from the ground (which is always known) as

$$\theta_s = 270^\circ - \alpha_s \quad (6.1)$$

The said azimuth being 57.5° for the *IS-20* satellite in Durban, θ_s is 212.5° . Also, the coordinate φ_s is related to the elevation angle θ_e as

$$\theta_e = 90^\circ - \varphi_s \quad (6.2)$$

At elevation angle 36.5° , φ_s equals 53.5° .

The position $C_1(\rho_1, \theta_1, \varphi_1)$ is where the migrating rain cell is expected to have encountered the satellite beacon to effect the observed attenuation. ρ_1 is the slant path length L_S given in terms of rain height h_R by

$$L_S = \frac{(h_R - h_s)}{\sin \theta_e} \quad (\text{km}) \quad (6.3)$$

By putting in the values of h_s and θ_e as 0.176 km and 36.5° respectively, ρ_1 or the slant path can be expressed in terms of rain height as

$$\rho_1 = L_S = 1.681h_R - 0.2959 \quad (6.4)$$

Like θ_s , θ_1 is also directly related to the azimuth angle α_1 of the migrating rain form as measured from the ground such that

$$\theta_1 = 270^\circ - \alpha_1 \quad (6.5)$$

Hence, θ_1 is also 212.5° . φ_1 is related to the elevation angle such that

$$\theta_e = 90^\circ - \varphi_1 \quad (6.6)$$

Thus, φ_1 also equals 53.5° .

At the point $C_2(\rho_2, \theta_2, \varphi_2)$, where precipitation occurs at the receive antenna, ρ_2 is the rain height h_R during that particular event while θ_2 and φ_2 both equal zero. During a true, observable time lapse event the necessary condition is that

$$\theta_1 = \theta_s \text{ OR } \alpha_1 = \alpha_s$$

Which implies that the rain cell must be migrating in such a direction that its azimuth relative to the origin is at least approximately equal to that of the stationary satellite. It should be noted that typical dimensions of rain height, cell size and slant path length are very similar, all measuring typically less than 10 km. This is why significant time delay scenarios where it can be distinctly claimed that the rain

cell encounters the slant path before reaching the receive antenna location, can only be a small fraction of the rain events captured.

For of evaluation purposes, we can express the points C_1 and C_2 to Cartesian coordinates using the identities

$$\begin{cases} x = \rho \sin \varphi \cos \theta \\ y = \rho \sin \varphi \sin \theta \\ z = \rho \sin \varphi \cos \theta \end{cases} \quad (6.7)$$

For the conversion, we input the known parameters of the link as done above. Thus the points $C_1(x_1, y_1, z_1)$ and $C_2(x_2, y_2, z_2)$ are obtained where the elements x_1, y_1, z_1 and x_2, y_2, z_2 are represented by linear expressions. In these expressions, the only unknown that will appear is the rain height h_R . This is because ρ_1 is expressed in terms of h_R from (6-4) while ρ_2 equals h_R . The actual distance covered by the rain cell in the time of delay is given by the magnitude of the vector

$$\underline{C} = (x_2 - x_1) \underline{x} + (y_2 - y_1) \underline{y} + (z_2 - z_1) \underline{z} \quad (6.8)$$

Alternatively, we can represent the components in each direction as functions of h_R such that

$$\underline{C} = A(h_R) \underline{x} + B(h_R) \underline{y} + C(h_R) \underline{z} \quad (6.9)$$

The magnitude of the vector \underline{C} is given by

$$|\underline{C}| = (A^2 + B^2 + C^2)^{1/2} \quad (6.10)$$

The right hand side of equation (6.9) will yield a quadratic function in h_R .

This distance covered $|\underline{C}|$ is easily extracted for each event using the time delay database presented in Table 6-1. A model is adopted for rain advection velocity by [121, 122], [123] which was confirmed for rain patterns in Durban, South Africa by [60]. Based on extensive radar measurements, the model allocates velocities of 6 ms^{-1} to 12 ms^{-1} to migrating rain cells depending on whether it is a Stratiform rain event or a convective rain event. The classification is done based on the highest rain peak in the event which is considered to be an indication of where the centre of the cell is and the size of the cell [60]. Larger rain cells tend to cause Stratiform rain and are associated with lower cloud advection speeds while the smaller cells lead to convective rain and attain higher cloud advection speeds. Using the values of $|\underline{C}|$ thus obtained, we reduce the entire equation (6.9) to an expression in h_R and we can thus estimate the rain height during individual time delay events. Thus, we have

$$vt_{delay} = (A^2 + B^2 + C^2)^{1/2} \quad (6.11)$$

where v is the advection velocity and t_{delay} is the time delay for that event.

6.5 Results of Rain Height Estimated from Time Delay Statistics.

Taking cloud advection velocities of 6 ms^{-1} for events of maximum rain rate below 5 mmh^{-1} , 9 ms^{-1} for events of up to 30 mmh^{-1} rain rate and 12 ms^{-1} for events above 30 mmh^{-1} , the value of h_R for each rain event was calculated using the expression in (6.10). The results generally show a good agreement with that of known methods [121], [122], [69]. Table 6-2 presents the results obtained for each of the events.

The ITU-recommended method for estimating rain height is outlined in [69]. The method recommends the adoption of an annual average value of h_R given by

$$h_R = h_0 + 0.36 \quad (\text{km}) \quad (6.12)$$

where h_0 is the height of the zero-degree isotherm which is a parameter that fluctuates for every location over a range in an annual rain cycle, taking on a different value from event to event. 0.36 km is taken as the height of the melting layer. A map is provided in [69] from which the annual average value of h_0 can be read off for any location.

The ITU model shows that the global range of average annual values lies between 1.36 km and 6.36 km. The values obtained from the time delay analysis shows a similar range from 1.4 km to 6.7 km. Figure 6-3 shows the exceedance probability of rain height values in Durban assuming that the time delay analysis is accurate. The rain height exceeded at 0.01% of the time as estimated by the foregoing analysis in Durban is about 5.3 km while the annual average value used for attenuation estimates due to [69] is 4.96 km.

The pattern of occurrence of time delay events appears to be insensitive to time of the year. The data shows no time delay events at all during three of the months of the year from which the statistics was obtained. This makes a credible annual analysis of rain height from time delay events improbable. A theoretical method such as is presented here which estimates h_R during specific events was not found in literature, the method might offer a better accuracy of attenuation estimates by eliminating the possible errors introduced by the adoption of an annual average value for rain height. Being an input into most slant path attenuation prediction methods [8], an event-specific estimate of rain height will afford a better prediction of attenuation on slant paths than an annual average.

Table 6-2: Rain Height estimates from time delay events

Time Delay (Minutes)	Estimated Rain Height (km)
15	6.48
7	1.69
14	3.55
7.5	3.15
6	1.42
7.7	1.88
7	1.69
14.8	6.39
13	5.6
5.8	2.4
5	2.04
7.5	1.82
15.5	6.71
5	2.04
4.6	1.87
4	1.6
6	2.49
7	2.94
5.3	2.18
4.9	2
9.6	4.09
5.4	2.22
10.5	4.49
4.6	1.87
5	2.04
11.5	4.93
7.5	3.15
6.5	2.71
8.5	3.6
5.9	1.4
10.7	4.57

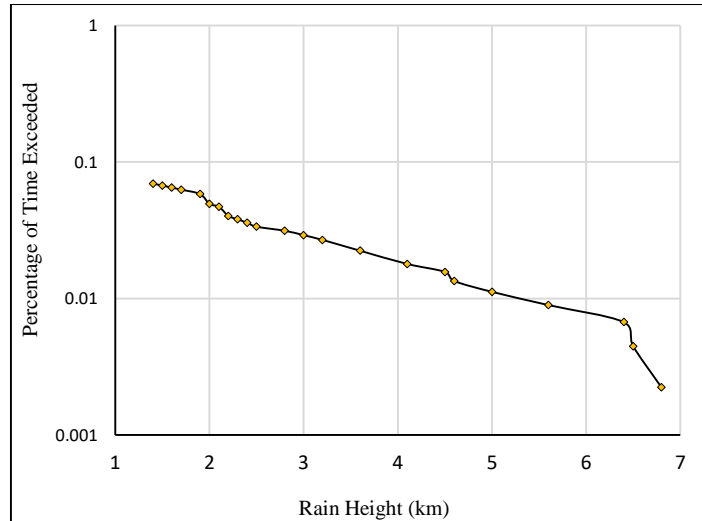


Figure 6-4: Exceedance probability of rain height estimated from time delay events in Durban

6.6 Chapter Summary

In this chapter, the anomaly of experiencing rain attenuation on the link several minutes before precipitation occurs is reported and discussed. A postulation is made that the delay is due to an interaction of the rain cell with the satellite beam before precipitation due to the same rain cell is observed at the receive antenna. Geometric analysis is presented to show that the level of delay is related to the variation in the rain height during each event. Adopting a model for cloud advection speed, a simple mathematical process is presented for estimating the rain height from the time delay statistics. Favourable comparison is shown between the rain height values obtained based on this approach and from other known methods.

CHAPTER SEVEN: CONCLUSIONS AND RECOMMENDATIONS

7.1.1 Introduction

In the scramble to roll out ever higher volumes of wireless communication links of high fidelity in the microwave band to meet rising demand, accurate and realistic estimates of the effects of hydrometeors on these links is of high importance. For certain regions of the world, dependence on theoretical methods that were evolved based on experiments in other regions may not be adequate to achieve this aim. Results of extensive experimental data and measurements of rain attenuation on slant paths from the subtropics have hitherto not been available. This thesis attempts, by several approaches, to present empirical and semi-empirical models for slant path rain attenuation on a typical communication service in the microwave band. Rain attenuation is a very significant source of loss in this frequency band, second only to free space path loss. System designers in the region depend primarily on theoretical models recommended by the ITU. The following conclusions can be drawn from the results reported in each of the chapters 3, 4, 5 and 6.

7.1.2 Chapter Three - Measurement of Attenuation at Ku Band in Subtropical Rain

From this chapter, the need for location-specific measured data for slant path attenuation as demonstrated by the results of modelling of measured attenuation in various statistical bounds. While existing theoretical approaches associate a single rain rate with a single attenuation level, measurement allows the full range of attenuation levels due to each rain rate to be seen so that planning can be made for the worst conditions rather than the best. The fade depth at various percentages of exceedance is modelled. The measurement model generally falls within the range of existing models but it offers a more realistic picture. In the myriad of cases (frequencies, slant path lengths, elevations angles), where exhaustive measurements cannot be carried out, statistical comparisons presented in this chapter are useful for selecting alternative theoretical estimation methods. Signal squelching takes place at high rain rates on microwave links. But temporary, instantaneous outage can also occur at relatively low rain rates.

7.1.3 Generation of Rain Attenuation Time Series from Measurement-Derived PDFs by Markov Chain Principle

Random number characteristics of measured slant path rain attenuation data can be exploited for prediction. The probability density function of measured seasonal and annual slant path subtropical rain attenuation statistics shows that it is a lognormal parameter. This discrete PDF represents the state space of probability matrix of the seasonal or annual dataset. The fade slope statistics is a Gaussian-distributed function. The probability of transitions between any two attenuation levels can be approximated from the discrete PDF of fade slope, thus enabling the calculation of a transition probability matrix possible for the particular attenuation state space. Long term rain attenuation data that simulates the random

number properties of real measurements is then generated by applying several iterations of the Markov chain. Slant path rain attenuation time series for the years 2013 to 2016 and for various seasons are generated.

7.1.4 Synthetic Storm Technique Analysis of Slant Path Attenuation in Subtropical Rain

Theoretical estimation of slant path attenuation in Durban can be done reliably by estimating it in the form of a synthetic storm for the long term. The synthetic storm technique appears to be the closest theoretical approach to actual measurement since it tends to coincide in value with the all-important $A_{0.01}$. The points of coincidence with measured data are 0.02% in 2013, 0.008% for 2014, 0.08% for 2015 and 0.019 % for 2016. This approach shows more promise in terms of accuracy than the theoretical ITU-R approach, being more statistically closer to the measured model.

7.1.5 Estimation of Rain Height from Attenuation-Precipitation Time Delay Data

Rain occurring on slant paths in a manner that precedes precipitation in the time domain is sometimes due to the rain cell interacting with the satellite beacon before it drops precipitation over the receiver location. With some knowledge of the cell speed, the time lapse can be used to estimate the rain height during the event. Rain height values estimated by this method show much similarity to traditional rain rate statistics.

7.2 Recommendations for Future Work

- Long term measurement campaigns on earth-satellite microwave links are required in subtropical regions of the world, especially in Australia, South America and other South African cities. The input from the region into the database utilized for planning and deployment needs to match those from the temperate regions.
- The one-on-one linear correlation between rain rate and attenuation generally adopted by the ITU-R theoretical model for slant path attenuation should be reviewed. The model should be mathematically reviewed to estimate for worst and best case scenarios.
- The measurement model in this work can be integrated into one or more fade mitigation schemes to enhance accuracy. Fade duration statistics and modelling will also be needed for this.
- The Markov chain method of generating slant path attenuation time series can be further developed by applying diverse methods for estimating the fade slope at each attenuation level.

- Event-specific radar measurements can be used to further validate the theoretical approach proposed in this work for estimating rain height using the statistics of time delay between attenuation and the commencement of precipitation.

REFERENCES

- [1] M. Kottke, J. Grieser, C. Beck, B. Rudolf, and F. Rubel, "World map of the Köppen-Geiger climate classification updated," *Meteorologische Zeitschrift*, vol. 15, pp. 259-263, 2006.
- [2] G. Ajayi, S. Feng, S. Radicella, and B. Reddy, "Hand Book on radio propagation related to satellite communications in tropical and sub-tropical countries UNESCO and ICTP," *URS I Standing committee on developing countries*, 1996.
- [3] O. Adetan and T. Afullo, "Raindrop size distribution and rainfall attenuation modeling in equatorial and subtropical Africa: the critical diameters," *Annals of telecommunications-Annales des telecommunications*, vol. 69, pp. 607-619, 2014.
- [4] A. A. Alonge and T. J. O. Afullo, "Seasonal analysis and prediction of rainfall effects in Eastern South Africa at microwave frequencies," *Progress In Electromagnetics Research B*, vol. 40, pp. 279-303, 2012.
- [5] M. Odedina and T. Afullo, "Determination of rain attenuation from electromagnetic scattering by spherical raindrops: Theory and experiment," *Radio Science*, vol. 45, 2010.
- [6] P. A. Owolawi, T. Afullo, and S. Malinga, "Rainfall rate characteristics for the design of terrestrial link in South Africa," in *Proc. of SATNAC*, 2008, pp. 71-76.
- [7] T. S. Rappaport, F. Gutierrez, E. Ben-Dor, J. N. Murdock, Y. Qiao, and J. I. Tamir, "Broadband millimeter-wave propagation measurements and models using adaptive-beam antennas for outdoor urban cellular communications," *IEEE transactions on antennas and propagation*, vol. 61, pp. 1850-1859, 2013.
- [8] P. Series, "Propagation data and prediction methods required for the design of Earth-space telecommunication systems," *Recommendation ITU-R*, pp. 618-12, 2015.
- [9] K. Chakravarty and A. Maitra, "Rain attenuation studies over an earth-space path at a tropical location," *Journal of Atmospheric and Solar-Terrestrial Physics*, vol. 72, pp. 135-138, 2010.
- [10] S. Das and A. Maitra, "Some melting layer characteristics at two tropical locations in Indian region," in *General Assembly and Scientific Symposium, 2011 XXXth URSI*, 2011, pp. 1-4.
- [11] C.-H. Tseng, K.-S. Chen, J. Shi, and C. Chu, "Prediction of Ka-band terrestrial rain attenuation using 2-year rain drop size distribution measurements in Northern Taiwan," *Journal of Electromagnetic Waves and Applications*, vol. 19, pp. 1833-1841, 2005.
- [12] I. Adimula and G. Ajayi, "Variations in raindrop size distribution and specific attenuation due to rain in Nigeria," in *Annales des télécommunications*, 1996, pp. 87-93.
- [13] J. Mandeep, O. W. Hui, M. Abdullah, M. Tariqul, M. Ismail, W. Suparta, *et al.*, "Modified ITU-R rain attenuation model for equatorial climate," in *Space Science and Communication (IconSpace), 2011 IEEE International Conference on*, 2011, pp. 89-92.
- [14] R. K. Crane, "Modelling attenuation by rain in tropical regions," *International Journal of Satellite Communications and Networking*, vol. 8, pp. 197-210, 1990.

- [15] J. Goldhirsh, "Prediction of slant path rain attenuation statistics at various locations," *Radio Science*, vol. 12, pp. 741-747, 1977.
- [16] J. Mandeep and S. Hassan, "Slant-path rain attenuation predictions in tropical regions," *Journal of atmospheric and solar-terrestrial physics*, vol. 68, pp. 865-868, 2006.
- [17] A. Y. Kwarteng, A. S. Dorvlo, and G. T. Vijaya Kumar, "Analysis of a 27-year rainfall data (1977–2003) in the Sultanate of Oman," *International Journal of Climatology*, vol. 29, pp. 605-617, 2009.
- [18] J. S. Ojo and O. C. Rotimi, "Diurnal and seasonal variations of rain rate and rain attenuation on Ku-band satellite systems in a tropical region: A synthetic storm techniques approach," *Journal of Computer and Communications*, vol. 3, p. 1, 2015.
- [19] O. O. Obiyemi, O. Adetan and T. S. Ibiyemi, "Recent update on one-minute rainfall rate measurements for microwave applications in Nigeria." *International Journal of Wireless Communications and Mobile Computing* vol. 3, p. 33-39, 2015.
- [20] D.P. Corson, F. Lorain, *Electromagnetic Fields and Waves*, 3rd Edition, WH Freeman and Company, New York, 1987
- [21] B. I. Bleaney, B. I. Bleaney, and B. Bleaney, *Electricity and Magnetism*, Volume 2: Oxford University Press, 2013.
- [22] K. Finkenzerler, *RFID handbook: fundamentals and applications in contactless smart cards, radio frequency identification and near-field communication*: John Wiley & Sons, 2010.
- [23] D. M. Leive, *International Telecommunications and International Law: The Regulation of the Radio Spectrum*, Oceana Publications Inc., Dobbs Ferry, New York, 1970.
- [24] T. Union, "International Telecommunication Union," *Yearbook of Statistics 1991–2000*, 2001.
- [25] T. S. Rappaport, *Wireless communications: principles and practice* vol. 2: prentice hall PTR New Jersey, 1996.
- [26] J. Lane, "Small-scale irregularities of the radio refractive index of the troposphere," *Nature*, vol. 204, pp. 438-440, 1964.
- [27] T. Tsuda, P. May, T. Sato, S. Kato, and S. Fukao, "Simultaneous observations of reflection echoes and refractive index gradient in the troposphere and lower stratosphere," *Radio science*, vol. 23, pp. 655-665, 1988.
- [28] T. Tamir, "On radio-wave propagation in forest environments," *IEEE Transactions on Antennas and Propagation*, vol. 15, pp. 806-817, 1967.
- [29] N. C. Rogers, A. Seville, J. Richter, D. Ndzi, N. Savage, R. Caldeirinha, *et al.*, "A generic model of 1-60 GHz radio propagation through vegetation-final report," *Radio Agency, UK*, 2002.
- [30] A. Seville, "Vegetation attenuation: Modelling and measurements at millimetric frequencies" *in IEE conference publication. Institution of Electrical Engineers*, vol. 2, pp. 2.5-2.8, 1997

- [31] E. COST 235, "Radiowave propagation effects on next generation fixed-services terrestrial telecommunications systems," *Final Report, No. EUR 16992 EN*, pp. 159-168, 1996.
- [32] R. K. Crane, *Electromagnetic wave propagation through rain*: Wiley-Interscience, 1996.
- [33] H. J. Liebe, "MPM—An atmospheric millimeter-wave propagation model," *International Journal of Infrared and millimeter waves*, vol. 10, pp. 631-650, 1989.
- [34] D. Cermak, O. Fiser, and V. Schejbal, "Electromagnetic Scattering by rain drops," *COST280*, 2005.
- [35] H. E. Green, "Propagation impairment on Ka-band SATCOM links in tropical and equatorial regions," *IEEE Antennas and Propagation Magazine*, vol. 46, pp. 31-45, 2004.
- [36] D. Hogg, "Millimeter-wave communication through the atmosphere," *Science*, vol. 159, pp. 39-46, 1968.
- [37] M. Ajewole, L. Kolawole, and G. Ajayi, "Evaluation of bistatic intersystem interference due to scattering by hydrometeors on tropical paths," *International Journal of Satellite Communications and Networking*, vol. 17, pp. 339-356, 1999.
- [38] C. Bohren and D. Huffman, "Absorption and scattering of light by small particles", *Wiley New York*, 1983.
- [39] M. N. Sadiku, "Numerical techniques in electromagnetics second edition," 2007.
- [40] M. Ajewole, L. Kolawole, and G. Ajayi, "Theoretical study of the effect of different types of tropical rainfall on microwave and millimeter-wave propagation," *Radio Science*, vol. 34, pp. 1103-1124, 1999.
- [41] H. Pruppacher and K. Beard, "A wind tunnel investigation of the internal circulation and shape of water drops falling at terminal velocity in air," *Quarterly Journal of the Royal Meteorological Society*, vol. 96, pp. 247-256, 1970.
- [42] H. R. Pruppacher and R. Pitter, "A semi-empirical determination of the shape of cloud and rain drops," *Journal of the atmospheric sciences*, vol. 28, pp. 86-94, 1971.
- [43] M. O. AJEWOLE, "Scattering and attenuation of centimetre and millimetre radio signals by tropical rainfall," *FEDERAL UNIVERSITY OF TECHNOLOGY, AKURE*, 1997.
- [44] W. Myers and T. Richardson, "Project IEEE P802. 16 Broadband Wireless Access Working Group Title Comparison of Propagation Models," 1999.
- [45] L. J. Battan, "Radar observation of the atmosphere," 1973.
- [46] D. Xu, Y. Li, M. Chiang, and A. R. Calderbank, "Elastic service availability: utility framework and optimal provisioning," *IEEE Journal on selected areas in communications*, vol. 26, 2008.
- [47] G. Nykolak, J. Auburn, H. Presby, P. Szajowski, and G. Tourgee, "Update on 4x2. 5Gb/s, 4.4 km free-space optical communications link: availability and scintillation," in *Optical Wireless Communications II, Proc. SPIE*, 1999.
- [48] I. R. P. Series, "Characteristics of precipitation for propagation modelling," *Recommendation ITU-R*, pp. 837-6, 2013.

- [49] G. Ajayi and E. Ofoche, "Some tropical rainfall rate characteristics at Ile-Ife for microwave and millimeter wave applications," *Journal of Climate and Applied Meteorology*, vol. 23, pp. 562-567, 1984.
- [50] A. A. Alonge and T. J. Afullo, "Characteristics of rainfall queues for rain attenuation studies over radio links at subtropical and equatorial Africa," *Radio Science*, vol. 49, pp. 583-596, 2014.
- [51] F. Moupfouma, "More about rainfall rates and their prediction for radio systems engineering," in *IEE Proceedings H (Microwaves, Antennas and Propagation)*, 1987, pp. 527-537.
- [52] A. Tokay, D. A. Short, C. R. Williams, W. L. Ecklund, and K. S. Gage, "Tropical rainfall associated with convective and stratiform clouds: Intercomparison of disdrometer and profiler measurements," *Journal of Applied Meteorology*, vol. 38, pp. 302-320, 1999.
- [53] M. Singh and J. E. Allnutt, "Rain attenuation predictions at Ku-band in South East Asia countries," *Progress In Electromagnetics Research*, vol. 76, pp. 65-74, 2007.
- [54] T. J. O. Afullo, "Raindrop size distribution modeling for radio link design along the eastern coast of South Africa," *Progress In Electromagnetics Research B*, vol. 34, pp. 345-366, 2011.
- [55] A. Alonge and T. Afullo, "Rainfall rate modeling for various rainfall types in South Africa," in *AFRICON, 2011*, 2011, pp. 1-6.
- [56] P. A. Owolawi and T. J. Afullo, "Rainfall rate modeling and worst month statistics for millimetric line-of-sight radio links in South Africa," *Radio Science*, vol. 42, 2007.
- [57] P. A. Owolawi, "Rainfall rate probability density evaluation and mapping for the estimation of rain attenuation in South Africa and surrounding islands," *Progress In Electromagnetics Research*, vol. 112, pp. 155-181, 2011.
- [58] P. Odedina and T. Afullo, "A Simplified Statistical Modeling of Radioclimatological Parameters for LOS Links in South Africa," 2008.
- [59] M. N. Ahuna, T. J. Afullo, and A. A. Alonge, "30-second and one-minute rainfall rate modelling and conversion for millimetric wave propagation in South Africa," *Journal of the South African Institute of Electrical Engineers*, vol. 107, 2016.
- [60] P. Akuon and T. Afullo, "Rain Cell Sizing For The Design Of High Capacity Radio Link Systems In South Africa," *Progress In Electromagnetics Research B*, vol. 35, 2011.
- [61] P. Akuon and T. Afullo, "Rain cell size statistics from rain gauge data for site diversity planning and attenuation prediction," in *Proc. of SATNAC*, 2011, pp. 213-216.
- [62] A. A. Alonge and T. J. Afullo, "Fractal analysis of rainfall event duration for microwave and millimetre networks: rain queueing theory approach," *IET Microwaves, Antennas & Propagation*, vol. 9, pp. 291-300, 2014.
- [63] T. Oguchi, "Attenuation of electromagnetic wave due to rain with distorted raindrops, 2," *Journal of the Radio Research Laboratory*, vol. 10, p. 19-44, 1964.

- [64] S. Lin, "11 GHz radio: Nationwide long-term rain rate statistics and empirical calculation of 11 GHz microwave rain attenuation," *Bell Labs Technical Journal*, vol. 56, pp. 1581-1604, 1977.
- [65] R. Olsen, D. V. Rogers, and D. Hodge, "The aR b relation in the calculation of rain attenuation," *IEEE Transactions on antennas and propagation*, vol. 26, pp. 318-329, 1978.
- [66] R. Crane, "Prediction of attenuation by rain," *IEEE Transactions on communications*, vol. 28, pp. 1717-1733, 1980.
- [67] J. García-López and J. Peiro, "Simple rain-attenuation-prediction technique for terrestrial radio links," *Electronics Letters*, vol. 19, pp. 879-880, 1983.
- [68] J. Garcia-Lopez, J. Hernando, and J. Selga, "Simple rain attenuation prediction method for satellite radio links," *IEEE transactions on antennas and propagation*, vol. 36, pp. 444-448, 1988.
- [69] S. P, "Rain height model for prediction methods," *Erecommendation ITU-R*, pp. 839-4, 2013.
- [70] ITU-Recommendations, "Specific attenuation model for rain for use in prediction methods," ed. Geneva, Switzerland: International Telecommunication Union, 2006.
- [71] P. Akuon and T. Afullo, "Path reduction factor modeling for terrestrial links based on rain cell growth," in *AFRICON, 2011*, 2011, pp. 1-6.
- [72] A. Adhikari, S. Das, A. Bhattacharya, and A. Maitra, "Improving rain attenuation estimation: Modelling of effective path length using Ku-band measurements at a tropical location," *Progress In Electromagnetics Research B*, vol. 34, pp. 173-186, 2011.
- [73] G. Maral, J. J. de Ridder, B. G. Evans, and M. Richharia, "Low earth orbit satellite systems for communications," *International Journal of Satellite Communications and Networking*, vol. 9, pp. 209-225, 1991.
- [74] A. D. Panagopoulos, P.-D. M. Arapoglou, and P. G. Cottis, "Satellite communications at Ku, Ka, and V bands: Propagation impairments and mitigation techniques," *IEEE Communications Surveys & Tutorials*, vol. 6, 2004.
- [75] J. E. Drain, "Three- and four-satellite continuous-coverage constellations," *Journal of Guidance, Control, and Dynamics*, vol. 8, pp. 725-730, 1985.
- [76] G. J. Geier, R. C. Hart, and T. M. King, "Method and apparatus for accurately determining the position of satellites in geosynchronous orbits," ed: Google Patents, 2003.
- [77] B. G. Evans, *Satellite communication systems* vol. 38: IET, 1999.
- [78] W. Jiang and P. Zong, "Prediction and compensation of sun transit in LEO satellite systems," in *Communications and Mobile Computing (CMC), 2010 International Conference on*, 2010, pp. 495-499.
- [79] J. Vankka and A. Kestilä, "Sun outage calculator for satellite communications," in *Space Science and Communication (IconSpace), 2013 IEEE International Conference on*, 2013, pp. 51-55.

- [80] A. Salmi, L. Elomaa, P. Kopsala, E. Laukkanen, and V. Oyj, "Piezoelectric Vaisala Raincap® Rain Sensor Applied To Drop Size Distribution Monitoring," in *Technical Conference on Meteorological and Environmental Instruments and Methods of Observation*. Geneva: World Meteorological Organization, 2011, pp. 1-7.
- [81] P. Licznar, J. Łomotowski, S. Błoński, and G. J. Ciach, "Microprocessor field impactometer calibration: Do we measure drops' momentum or their kinetic energy?," *Journal of Atmospheric and Oceanic Technology*, vol. 25, pp. 742-753, 2008.
- [82] Satbeams. (2016, 3rd March). *Satbeams IS-20 Satellite Footprint*. Available: <https://www.satbeams.com/footprints?beam=7014>
- [83] H. W. Ott and H. W. Ott, *Noise reduction techniques in electronic systems* vol. 442: Wiley New York, 1988.
- [84] J. S. Pal, F. Giorgi, X. Bi, N. Elguindi, F. Solmon, S. A. Rauscher, *et al.*, "Regional climate modeling for the developing world: the ICTP RegCM3 and RegCNET," *Bulletin of the American Meteorological Society*, vol. 88, pp. 1395-1409, 2007.
- [85] C. Reason, S. Hachigonta, and R. Phaladi, "Interannual variability in rainy season characteristics over the Limpopo region of southern Africa," *International Journal of Climatology*, vol. 25, pp. 1835-1853, 2005.
- [86] P. ITU-R, "RECOMMENDATION ITU-R P. 837-7,," *Characteristics of precipitation for propagation modeling*, ITU, Geneva, Switzerland, 2003.
- [87] W. Buytaert, R. Celleri, P. Willems, B. De Bievre, and G. Wyseure, "Spatial and temporal rainfall variability in mountainous areas: A case study from the south Ecuadorian Andes," *Journal of hydrology*, vol. 329, pp. 413-421, 2006.
- [88] G. Bryant, I. Adimula, C. Riva, and G. Brussaard, "Rain attenuation statistics from rain cell diameters and heights," *International Journal of Satellite Communications and Networking*, vol. 19, pp. 263-283, 2001.
- [89] G. Peeters, F. S. Marzano, G. d'Auria, C. Riva, and D. Vanhoenacker-Janvier, "Evaluation of statistical models for clear-air scintillation prediction using Olympus satellite measurements," *International journal of satellite communications*, vol. 15, pp. 73-88, 1997.
- [90] B. C. Grémont and M. Filip, "Spatio-temporal rain attenuation model for application to fade mitigation techniques," *IEEE Transactions on Antennas and Propagation*, vol. 52, pp. 1245-1256, 2004.
- [91] P. Series, "Acquisition, presentation and analysis of data in studies of radiowave propagation" *Recommendation ITU-R*, pp. 311-16, 2016.
- [92] H. O. Lancaster and E. Seneta, *Chi-square distribution*: Wiley Online Library, 1969.
- [93] W. R. Gilks, S. Richardson, and D. J. Spiegelhalter, "Introducing markov chain monte carlo," *Markov chain Monte Carlo in practice*, vol. 1, p. 19, 1996.
- [94] B. A. Berg and A. Billoire, *Markov chain monte carlo simulations*: Wiley Online Library, 2008.

- [95] S. Karlin, *A first course in stochastic processes*: Academic press, 2014.
- [96] M. Mitzenmacher, "A brief history of generative models for power law and lognormal distributions," *Internet mathematics*, vol. 1, pp. 226-251, 2004.
- [97] M. M. Van de Kamp, "Statistical analysis of rain fade slope," *IEEE Transactions on Antennas and Propagation*, vol. 51, pp. 1750-1759, 2003.
- [98] F. Rücker, "Frequency and attenuation dependent fade slope statistics," *Electronics Letters*, vol. 29, pp. 744-746, 1993.
- [99] F. Dintelmann, "Analysis of 11 GHz slant path fade duration and fade slope," *Electronics letters*, vol. 17, pp. 267-268, 1981.
- [100] W. Turin and R. Van Nobelen, "Hidden Markov modeling of flat fading channels," *IEEE Journal on Selected Areas in Communications*, vol. 16, pp. 1809-1817, 1998.
- [101] B. Héder and J. Bitó, "Rain attenuation time series generation applying N-State markov model parameterised from Hungarian measurement," in *ESTEC 2005 Conference*, 2005.
- [102] E. Matricciani, C. Riva, and L. Castanet, "Performance of the synthetic storm technique in a low elevation 5 slant path at 44.5 GHz in the French Pyrénées," in *Antennas and Propagation, 2006. EuCAP 2006. First European Conference on*, 2006, pp. 1-6.
- [103] C. I. Kourogorgas, A. D. Panagopoulos, J. D. Kanellopoulos, S. N. Livieratos, and G. E. Chatzarakis, "Investigation of rain fade dynamic properties using simulated rain attenuation data with synthetic storm technique," in *Antennas and Propagation (EuCAP), 2013 7th European Conference on*, 2013, pp. 2277-2281.
- [104] I. Sánchez-Lago, F. Fontán, P. Mariño, and U.-C. Fiebig, "Validation of the synthetic storm technique as part of a time-series generator for satellite links," *IEEE Antennas and Wireless Propagation Letters*, vol. 6, pp. 372-375, 2007.
- [105] G. Drufuca, "Rain attenuation statistics for frequencies above 10 GHz from rain gauge records'," in *AGARD conference on telecommunication aspects of frequencies between*, 1974.
- [106] E. Matricciani, "Physical-mathematical model of the dynamics of rain attenuation based on rain rate time series and a two-layer vertical structure of precipitation," *Radio Science*, vol. 31, pp. 281-295, 1996.
- [107] G. Drufuca and I. Zawadzki, "Statistics of raingage data," *Journal of Applied Meteorology*, vol. 14, pp. 1419-1429, 1975.
- [108] P. Watson, G. Papaioannou, and J. Neves, "Attenuation and cross-polarisation measurements at 36 GHz on a terrestrial path," in *Union Radio Scientifique Internationale, Open Symposium*, 1977, pp. 283-287.
- [109] B. Harden, J. Norbury, and W. White, "Model of intense convective rain cells for estimating attenuation on terrestrial millimetric radio links," *Electronics Letters*, vol. 10, pp. 483-484, 1974.

- [110] G. Drufuca and R. Rogers, "Statistics of rainfall over paths from 1 to 50 km," *Atmospheric Environment (1967)*, vol. 12, pp. 2333-2342, 1978.
- [111] A. Frisch, B. Stankov, B. Martner, and J. Kaimal, "Midtroposphere wind speed spectra from long-term wind profiler measurements," *Journal of Applied Meteorology*, vol. 30, pp. 1646-1651, 1991.
- [112] P. Series, "Rain height model for prediction methods," *Recommendations ITU=R*, 1992.
- [113] D. Maggiori, "Computed transmission through rain in the 1-400 GHz frequency range for spherical and elliptical drops and any polarization," *Alta Frequenza*, vol. 50, pp. 262-273, 1981.
- [114] D. Maggiori, "Calculation of the attenuation and phase displacement per unit of length due to rain composed of ellipsoidal drops," 1981.
- [115] S. Ghirardin, "Space and time evolution of synthetic rain structures," 2015.
- [116] A. K. Lwas, M. R. Islam, M. H. Habaebi, A. Ismail, K. Abdullah, A. Zyoud, *et al.*, "Analysis of the synthetic storm technique using rain height models to predict rain attenuation in tropical regions," in *Computer and Communication Engineering (ICCCE), 2014 International Conference on*, 2014, pp. 220-223.
- [117] J. Ojo and P. Owolawi, "Application of synthetic storm technique for diurnal and seasonal variation of slant path Ka-band rain attenuation time series over a subtropical location in South Africa," *International Journal of Antennas and Propagation*, vol. 2015, 2015.
- [118] B.O. Afolayan, T.J. Afullo and A.A. Alonge, "Seasonal and annual analysis of slant path attenuation over a 12 GHz earth-satellite link in subtropical Africa," *International Journal on Communications and Antenna Propagation*, vol. 7 (7), Dec 2017.
- [119] S. Manabe, "Climate and the ocean circulation 1: i. The atmospheric circulation and the hydrology of the earth's surface," *Monthly Weather Review*, vol. 97, pp. 739-774, 1969.
- [120] N. Walker, "Links between South African summer rainfall and temperature variability of the Agulhas and Benguela Current systems," *Journal of Geophysical Research: Oceans*, vol. 95, pp. 3297-3319, 1990.
- [121] G. Drufuca, "Radar-derived statistics on the structure of precipitation patterns," *Journal of Applied Meteorology*, vol. 16, pp. 1029-1035, 1977.
- [122] A. Pawlina-Bonati, "Essential knowledge of rain structure for radio applications based on available data and models," in *Proc. third Regular Workshop on Radio Communication in Africa Gaborone, Botswana*, 1999, pp. 25-29.
- [123] S. Begum, C. Nagaraja, and I. Otung, "Analysis of rain cell size distribution for application in site diversity," in *Antennas and Propagation, 2006. EuCAP 2006. First European Conference on*, 2006, pp. 1-5.